# Electronic structure of acceptor arrays in silicon

Jianhua Zhu

A dissertation submitted in partial fulfillment of the requirements for the degree of

**Doctor of Philosophy** 

Ωf

**University College London.** 

UCL Department of Physics and Astronomy and London Centre for
Nanotechnology
University College London

October 11, 2022

I, Jianhua Zhu, confirm that the work presented in this thesis is my own. Where information has been derived from other sources, I confirm that this has been indicated in the work.

### **Abstract**

In this thesis, we develop a tight-binding model based on linear combination of atomic orbitals (LCAO) methods to describe the electronic structure of arrays of acceptors, where the underlying basis states are derived from an effective-mass-theory solution for a single acceptor in the cubic model. Our model allows for arbitrarily strong spin-orbit coupling in the valence band of the semiconductor. Based on that, we compute the electronic structure of acceptor clusters in silicon by using three different methods to take into account electron correlations: the full configuration interaction (full CI calculation), the Heitler-London approximation (HL approximation), and the unrestricted Hartree-Fock method (UHF method). We have studied pairs and dimerised linear chains of acceptors in silicon in the 'independent-hole' approximation, and investigated the conditions for the existence of topological edge states in the chains. For the finite chain we find a complex interplay between electrostatic effects and the dimerisation, with the long-range Coulomb attraction of the hole to the acceptors splitting off states localised at the end acceptors from the rest of the chain. A further pair of states then splits off from each band, to form a pair localised on the next-to-end acceptors, for one sense of the bond alternation and merges into the bulk bands for the other sense of the alternation. We confirm the topologically non-trivial nature of these next-to-end localised states by calculating the Zak phase. We argue that for the more physically accessible case of one hole per acceptor these long-range electrostatic effects will be screened out; we show this by treating a simple phenomenologically screened model in which electrostatic contributions from beyond the nearest neighbours of acceptor each pair are removed. Topological states are now found on the end acceptors of the chains. In some cases

Abstract 4

the termination of the chain required to produce topological states is not the one expected on the basis of simple geometry (short versus long bonds); we argue this is because of a non-monotonic relationship between the bond length and the effective Hamiltonian matrix elements between the acceptors. We also compute the electronic structure of acceptor clusters in silicon by using three different methods to take into account electron correlations: the full configuration interaction (full CI calculation), the Heitler-London approximation (HL approximation), and the unrestricted Hartree-Fock method (UHF method). We show that both the HL approach and the UHF method are good approximations to the ground state of the full CI calculation for a pair of acceptors and for finite linear chains along [001], [110] and [111]. The total energies for finite linear chains show the formation of a 4-fold degenerate ground state (lying highest in energy), below which there are characteristic low-lying 8-fold and 4-fold degeneracies, when there is a long (weak) bond at the end of the chain. We present evidence that this is a manifold of topological edge states. We identify a change in the angular momentum composition of the ground state at a critical pattern of bond lengths, and show that it is related to a crossing in the Fock matrix eigenvalues. We also test the symmetry of the self-consistent meanfield UHF solution and compare it to the full CI; the symmetry is broken under almost all the arrangements by the formation of a magnetic state in UHF, and we find further broken symmetries for some particular arrangements related to crossings between the Fock-matrix eigenvalues in the [001] direction. We also compute the charge distributions across the acceptors obtained from the eigenvectors of the Fock matrix; we find that, with weak bonds at the chain ends, two holes are localized at either end of the chain while the others have a nearly uniform distribution over the middle; this also implies the existence of the non-trivial edge states. We also apply the UHF method to treat an infinite linear chain with periodic boundary conditions, where the full CI calculation and the HL approximation cannot easily be used. We find the band structures in the UHF approximation, and compute the Zak phases for the occupied Fock-matrix eigenvalues; however, we find they do not correctly predict the topological edge states formed in this interacting system. On Abstract 5

the other hand, we find that direct study of the quantum numbers characterising the edge states, introduced by Turner *et al.*, provides a better insight into their topological nature. Finally, the one-hole and the multi-hole models are applied to the 2D system. We show the energy states for the finite arrangement as well as the band structures for periodic cases. We also compare the full CI result with the UHF one for the multi-hole model, where we find including large next-nearest interactions will improve the accuracy of the results when we investigate the distribution of the holes. Then we prove the existence of the topological edge states in the infinite honeycomb lattice under the multi-hole model, which is also verified in the calculations for the real doped silicon lattice.

### **Impact Statement**

In the last few decades, studies of defects in semi-conducting systems have broadened to include applications to quantum computation and quantum simulation as well as their more traditional role in doping for classical electronics. Donors are especially well studied but in materials such as silicon having degenerate conduction band minima they suffer from the disadvantage of inter-valley interferences causing rapid oscillations in the wave functions and hence also in hopping or exchange interactions, leading to extreme sensitivity to the precise dopant position. The spin-orbit coupling in the acceptor provides an opportunity that it allows the formation of a much wider variety of non-trivial topological states, and also provides another way to manipulate the spin degree of freedom using electric fields. And an powerful model which could make accurate predictions on the band structure of the acceptor system is the first step to achieve the benefits above.

In this paper, we develop a tight-binding model based on linear combination of atomic orbitals (LCAO) methods to describe the electronic structure of arrays of acceptors, and then include the hole-hole interactions in three different ways to investigate the multi-hole systems. Our results generalise the concept of topological edge states to encompass the richness of bandedge degeneracy and spin-orbit coupling expected in acceptor states in silicon. Our findings point to the complex interplay between topological effects based on the dimerisation, the distance dependence of the interactions, and the long-range electrostatics that is likely to determine the nature and location of the edge states in the one-hole system. Our models and results achieved make it possible to envisage novel spintronic devices based on the manipulation of hole spins, as well as electrically controlled silicon quantum bits

(qubits), which implies potential applications in quantum simulation and quantum computation. Based on my study of acceptors, it should provide a rich platform for the study of topological and quantum effects in the acceptors systems and other relevant fields in the future.

## Acknowledgements

I wish to acknowledge the support of the Engineering and Physical Sciences Research Council and UK Research and Innovation under the ADDRFSS programme (grant EP/M009564/1). I thank Andrew Fisher, Wei Wu, Sankalan Bhattacharyya, Steven Schofield, Neil Curson, Ben Murdin, Nguyen Le, and Gabriel Aeppli for helpful and inspiring discussions.

# **Contents**

1	Intr	oductio	n	16
	1.1	Individ	dual dopants and quantum information	16
	1.2	Theory	y of donors	17
	1.3	Altern	ative candidate: acceptors	19
	1.4	Experi	imental progress	21
	1.5	Introd	uction to topological insulators and topological invariants	23
	1.6	Outlin	e of the structure for the rest of thesis	25
2	The	Single .	Acceptor Problem	28
	2.1	Single	-acceptor cubic model	28
	2.2	Single	acceptor result	31
	2.3	Summ	ary	34
3	One	-hole M	Iodel In One-dimensional Systems	35
	3.1	One-h	ole model	35
		3.1.1	A pair of acceptors	35
		3.1.2	Linear acceptor-chain and LCAO model	37
		3.1.3	Zak phase calculation for a generalized eigenvalue problem	40
	3.2	One-h	ole model results	40
		3.2.1	A pair of acceptors for the one-hole model	40
		3.2.2	Finite linear acceptor-chain	41
		3.2.3	Linear chain with periodic boundary conditions	46
	3.3	Summ	ary	51

Contents	10
----------	----

4	Mul	ti-hole l	Models In One-dimensional Systems	52
	4.1	Multi-	hole models	52
		4.1.1	Full CI calculation and HL approximation	53
		4.1.2	Unrestricted Hartree-Fock method	54
		4.1.3	Periodic boundary conditions	56
		4.1.4	Zak phase calculation for the multi-hole model	56
		4.1.5	Spatial cut-offs	57
		4.1.6	Single-particle basis	58
	4.2	Multi-	hole model results	61
		4.2.1	A pair of acceptors	61
		4.2.2	Finite dimerised linear chains	66
			4.2.2.1 Small-separation case $(d_1 + d_2 = 3a_0)$	66
			4.2.2.2 Large-separation case $(d_1 + d_2 = 6a_0)$	75
		4.2.3	Symmetry breaking in the UHF calculation	79
		4.2.4	Linear chain with periodic boundary conditions	81
		4.2.5	Structure of the edge states	86
	4.3	Summ	ary	88
5	Two	_dimen	sional Systems	90
J	5.1		imensional system	90
			imensional non-interacting system results	
	3.2	5.2.1	Finite systems without hole-hole interactions	
		3.2.1	5.2.1.1 Rectangles	
			5.2.1.2 Finite ladders	
		5.2.2	Infinite systems without hole-hole interactions	
	5.3		imensional interacting system results	
	3.3		• •	
		5.3.1	Finite system with hole-hole interactions	
		5.3.2	Infinite ladder with hole-hole interactions	
	~ ·	5.3.3	Honeycomb lattice with hole-hole interactions	
	5.4	Summ	ary	118

	Contents	11
6	Conclusions	121
Aį	ppendices	128
A	Modeling details for single-acceptor calculation	128
В	Modeling details for the tight-binding model	131
C	Modelling details for full CI calculation and HL approximation	134
D	Modelling details for unrestricted Hartree-Fock method	136
E	Modelling details for topological invariants	140

142

Bibliography

# **List of Figures**

1.1	The schematic diagram for the valance bands	19
2.1	The total probability density of the ground state	32
2.2	The single acceptor eigenstates as a function of $\Delta$	32
3.1	The schematic diagrams for the finite chain and the infinite chain	36
3.2	Eigenenergies in a pair of acceptors as a function of separation $r$	41
3.3	The smallest eigenvalue of the overlap matrix	42
3.4	The highest few energy states for the finite chain as a function of $d_1$ .	43
3.5	The band structure for the infinite chain	47
3.6	The band structure of the highest 4 states for the infinite chain	48
3.7	Schematic showing the definition of the transition strengths	49
4.1	The doubly-degenerate ground state energies for a pair of acceptors.	59
4.2	The probability density of the ground state wave functions	60
4.3	The interaction energy $E_{\rm int}$ and the difference of the total energy $E_{\rm tot}$ .	62
4.4	The Fock matrix eigenvalues for a pair of acceptors	63
4.5	The difference between the ground state and the first excited state	63
4.6	The probability density for different components in the ground state.	64
4.7	Schematics of the linear chains	65
4.8	The total energy of the ground state	66
4.9	The total energy of the highest 50 states of the full CI result	67
4.10	The Fock matrix eigenvalues obtained for the 4-acceptor chain	68
4.11	The Fock matrix eigenvalues obtained for the 6-acceptor chain	69
4 12	The total energy differences for different comparisons	70

5.14 The distributions of holes for the 4-acceptor rectangle. . . . . . . . . 104

5.15 The magnetic angular momentum for the 4-acceptor rectangle. . . . 104

5.16 Band structures for the infinite ladder with hole-hole interactions. . . 108

5.17 Band structures for the infinite ladder without hole-hole interactions. 108

5.18 The band structures in the small cell case of the infinite ladder. . . . 109

5.20 The magnetic angular momentum for the honeycomb lattice. . . . . 112

	List of Figures 14	
5.21	The parity and the band gap	
5.22	The parity of the ground states for different layers	

## **List of Tables**

2.1	The highest four single acceptor eigenenergies	32
3.1	The symmetry for the ground state under the cubic model	42
3.2	The Zak phase $Z$ for long-range model after mod $2\pi$	46
4.1	The eigenenergy of the 4-fold-degenerated ground state $(\Gamma_8^+)$	58
4.2	The magnetic symmetry groups of the UHF ground states	79
5.1	The localizing of states under the long-short arrangement	93
5.2	The Zak phase Z after mod $2\pi$ in the 2D systems	98
5.3	The largest fractional differences of the total energy	05
5.4	The parity and the $Z_2$ invariant $v$ for different separation $d$ 1	10

### **Chapter 1**

### Introduction

### 1.1 Individual dopants and quantum information

Quantum computing is the computation which performs calculations by using the properties of quantum states. A computer based on this is called a 'quantum computer'. There, the bits in the classical computers will be replaced by the qubits (quantum bits), which can take 0 or 1 quantum state. Comparing to a classical computer, a quantum computer can perform a large amount of calculations at the same time theoretically due to the superposition. But maintaining the states of qubits is extremely difficult as the quantum decoherence could arise during the calculation, so the outcome will be wrong. Although the results can be corrected by extra steps [1], new errors will keep arising as the decoherence of the qubits could come from many things such as interactions with the external environment and the lattice vibrations and it is almost impossible to get rid of all of them. So a threshold needs to be drawn for the error rate to truncate the progress of corrections. Then one of the main questions here is how to achieve a system with robust qubits so that the decoherence can be avoid as much as possible and the error rate is low enough.

For decades, the formidable capacity of the quantum computer attracts thousands of researchers dive into the investigation of it. In 1998, B. E. Kane proposed a possible method to achieve a quantum computer by using donors in doped silicon [2]. In that paper, he pointed out that information can be encoded onto the nuclear spin of donors. As the nuclear spin is well isolated from the external environment,

operations on the those qubits will have a lower error rate. The key of this proposal is to take advantage of the hyperfine interaction, which can be controlled by voltages applied to the device. There electron and nuclear spins are coupled by the hyperfine interaction. As the electrons are sensitive to the external electric fields, the hyperfine interaction and the electron-mediated nuclear spin interaction can be controlled by voltages applied to metallic gates in a semiconductor device, which will realize the required external manipulation of nuclear spin in the quantum computations. So the logical operations can be realized with the help of external electric fields, while measurements of spin can be done by using currents of spin-polarized electrons. The realization of this computer will be a great challenge as the material and the condition of the dopant needs to meet extraordinary requirements: the materials must be free of spin and charge impurities so the dephasing fluctuations can be avoided, while donors must be doped in an ordered array far beneath the surface. It is also difficult to build a required gate as the gates with lateral dimensions and separations around 100Å must be patterned on the surface and registered to the donors beneath them. But as it is a possible plan to realize the quantum computer with silicon (the dominant material in the microelectronics industry), it drives many researchers to the investigations of donors (we will see many new progresses have been achieved in the recent years in §1.4), and is also the motivation of this thesis.

### 1.2 Theory of donors

Although the band gap in a semiconductor is not as big as that in an insulator, the number of carriers is still very small. To increase the number of carriers, we can dope impurities with an additional electron or hole. The first kind of dopant is called 'donor', while the second one is called 'acceptor'. The energy states of donors are close to the conduction band in the semiconductor, so the electrons on these states can be thermally excited to the conduction band.

The effective mass approximation is one of the popular approximations applied to the semiconductor system to simplify the calculations[3]. There, the behavior of electrons (or holes) will be approached by the behavior of free electrons (or

free holes) with effective mass, while the effective mass of a particle is the mass it seems to have when it interacts with an other particle or moves in a field. After applied this approximation, it is possible to use equations and formulas applied to the free particle to describe a electron (or a hole) in the semiconductor system. And the calculations will be simplified as those equations and formulas (such as the Schrodinger equation) for the free particle are simple.

For a single donor [4], the question will becomes solving the perturbed crystal eigenvalue problem, which is

$$H\psi = \left[ -\frac{\hbar^2}{2m_0} \nabla^2 + V \right] \psi = E\psi. \tag{1.1}$$

Here V is the total crystal potential,  $\psi$  is the impurity-electron wave function. As this is based on the assumption that the perfect crystal eigenvalue problem has been solved, the total crystal potential V can be written as

$$V = V^0 + U, (1.2)$$

where  $V^0$  is the perfect-crystal periodic potential, and U is the perturbation. Then, following the discussion in Reference [4], one can achieve the form after applying the effective mass approximation as shown below

$$E_n^0(\vec{k})F_n(\vec{k}) + \sum_{\vec{k'}} U(|\vec{k} - \vec{k'}|)F_n(\vec{k'}) = EF_n(\vec{k}), \tag{1.3}$$

where  $E_n^0(\vec{k})$  is the energy of the *n*th band as a function of the wave vector  $\vec{k}$  in the first Brillouin Zone in the perfect crystal eigenvalue problem,  $F_n(\vec{k})$  are the parameters achieved when we expand  $\psi$  in terms of the complete orthonormal set of Bloch functions as

$$\psi(\vec{r}) = \sum_{n} \sum_{\vec{k}} F_n(\vec{k}) \psi_{n\vec{k}}^0(\vec{r}), \tag{1.4}$$

 $\psi^0_{nec k}$  are the Bloch functions. As the perturbation U is negative for donors, the

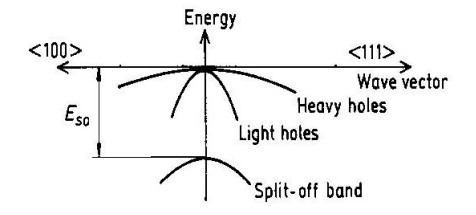


**Figure 1.1:** The schematic diagram for the valance bands.

relevant band here is the lowest conduction band, which has six equivalent minima. So, for example, the energy around the minimum along the +x direction, located at  $\vec{k}_1$ , can be written as

$$E^{0}(\vec{k}) \cong \frac{\hbar^{2}}{2m_{I}}(k_{x} - k_{1})^{2} + \frac{\hbar^{2}}{2m_{I}}(k_{y}^{2} + k_{z}^{2}). \tag{1.5}$$

The corresponding trial function in the real basis ( $F_i(\vec{r})$ ) is a sum of 1s- and 2s-like hydrogenic functions, which can be used easily in the further calculations. The exchange interaction of a pair of donors was studied with the Heitler-London treatment of exchange several decades ago [5]. There after giving the Hamiltonian operator, selected wavefunctions (most likely combinations of states for the system) will be used to calculate the energy of the system. So the calculation will be simplified dramatically. However, multi-conduction-band-minima found in donors will lead to unavoidable interference between the conduction-band valleys of the host (the multi-valley effects). This generates strong oscillation of spin-spin interactions in the exchange splitting of two-donor two-electron states, which makes the position of donors becomes important in determining the strength of the exchange coupling. But unwanted interactions could lead to decoherence of the qubits in the system, so extremely high precision will be required to take the places with no exchange-interaction.

### 1.3 Alternative candidate: acceptors

Besides donors, there is an other kind of dopant called 'acceptor'. The energy states of acceptors are close to the valence band in the semiconductor, so these states can accept electrons from the valence band as acceptors (Group III A elements) contain

extra holes compared with the other atoms (like silicon). The valence band has a single maximum at the Brillouin zone center ( $\Gamma$  point). But in some semiconductors (such as silicon and germanium), the valance bands at  $\Gamma$  point are degenerate as shown in Figure 1.1. The upper main band consists of the heavy- and light-hole bands, in which the effective masses are big and small, respectively. The bands are splitted at  $\Gamma$  point by the energy of  $E_{SO}$ , which is called 'spin-orbit coupling'. For the strong spin-orbit coupling case (a large  $E_{SO}$ ), the split-off band is far away from the main band, and we can neglect the influence of it. For the weak spin-orbit coupling case (small  $E_{SO}$ ) the split-off band is very close to the main band, and we can treat them as if they are degenerate. This will lead to different Hamiltonians for a single acceptor. For the strong spin-orbit coupling case (a large  $E_{SO}$ ), as the coupling is very strong, the vector of spin- $\frac{1}{2}$  spin operators  $\vec{S}$  and the vector of spin-1 angular momentum operators  $\vec{I}$  are always on the same line. So we can define the total intrinsic angular momentum of a valence-band electron  $\vec{J} = \vec{I} + \vec{S}$  which corresponding to spin- $\frac{3}{2}$  and only consider it in the calculations. For the weak spin-orbit coupling case (a small  $E_{SO}$ ), as the coupling is weak enough to be neglected, the vector of spin- $\frac{1}{2}$  spin operators  $\vec{S}$  is no longer relative to the question here. So we only need to deal with the vector of spin-1 angular momentum operators  $\vec{I}$  in the calculations. Another advantage of acceptors is that the spin (angular momentum) states can also be manipulated with electric fields, so acceptors could play the similar role as donors in the devices when we need to control the spins by the external electric fields.

Acceptors have attracted renewed attention because of the absence of multivalley effects in the valence band, which will lead to monotonic exchange and hopping interactions that are easier to control. However, owing to the spin-orbit coupling of the valence band, the spin-orbit interactions need to be taken into account from the outset.

Previously the electronic structures of a single acceptor in common semiconductors have been studied both theoretically and experimentally. Baldereschi and Lipari introduced the so-called 'spherical model' [6], based on the effective-mass

theory and including the cubic contributions either through perturbation theory [7] or in an exact form [8]. These calculations gave reasonably accurate predictions of the acceptor ionisation and excitation energies. Recently, Durst, et. al., computed the electronic structure and exchange interaction between two acceptors by adopting the spherical model and the Heitler-London approximation [9]. They also investigated the interaction between acceptor pairs in the extreme long-range limit, where hopping of electrons is no longer relevant, again using the spherical model [10]; they argue that in this limit the interactions are dominated by electric quadrupole moments.

### 1.4 Experimental progress

For the experiments, measurements of the optical transitions and spectra of acceptors in silicon have been performed [11]. The coherence time of the excited state of acceptors in silicon has also been measured, showing promise for optically controlled p-n devices [12]. The transport properties of boron in silicon, such as the conductivity and magnetoresistance have also been studied previously [13]. The Mott transition is a metal-insulator transition in condensed matter [14, 15]. The electric potential will form a well around each atom that will attract carriers, and the interactions between carriers will repel them away from each other. When these interactions get large enough, they will force the system into a insulating state with one carrier per acceptor or donor. The measurement can be done by testing the conductivity of the material under different temperatures: when the conductivity no longer depends on the temperature, it is on the metallic side of Mott transition. In a previous work [16], they offered experimental evidence for the Mott transition from randomly doped p-type bulk Si (Si:B). It suggests that the Mott transition occurs at densities around  $4.11 \times 10^{18} \, \text{cm}^{-3}$ , corresponding to average spacings around  $6.24 \, \text{nm} \approx 2.45 \, a_0$ .

The electrical detection and high-fidelity coherent manipulation of a single spin qubit for quantum computing are also proved possible [17]. Serial electron transport through a donor-based triple quantum dot in silicon with nanoscale preci-

sion is demonstrated by scanning tunnelling microscopy lithography in 2014 [18]. The method to electrically control electron spins in donor-based qubits in silicon is achieved in 2017 [19]. A device which can determine inter-donor distances to achieve controllable wavefunction overlap and perform high fidelity spin readout on each qubit at the same time is achieved by scanning tunnelling microscopy lithography in 2018 [20]. And a single qubit gate with coherent oscillations of the electron spin on a P donor molecule in Si patterned by scanning tunneling microscope lithography is demonstrated in 2021 [21].

A possible method to realize multi-qubit quantum circuits based on donors in silicon is pointed out in 2019 [22]. The many-body Su–Schrieffer–Heeger (SSH) model [23, 24, 25, 26, 27, 28] is the simplest one-dimensional model of strongly correlated topological matter, which is hard to be simulated in the experiment due to the challenge of precisely engineering long-range interactions between electrons. But recently a linear array of ten quantum dots successfully realize both the trivial and the topological phases of the many-body SSH model for precision-placed atoms in silicon with strong Coulomb confinement [29]. There, they tuned the ratio between intercell and intracell electron transport to observe signatures of the topological phase and the trivial phase with different number of conductance peaks.

Recently, the readout and control of the spin-orbit state of two coupled acceptors in silicon was demonstrated experimentally, opening up another route to quantum computing and quantum information in silicon [30, 31, 32, 33, 34]. Acceptor pairs in silicon have also been used for simulations of fermionic strongly-correlated many-body systems [35]. A team from IBM recently proved that boron in diborane can be used as a p-type dopant in silicon to build p-type nanowire devices in combination with hydrogen lithography [36]. And, in collaboration with researchers from UCL and Keysight Technologies, they made p-n junctions with phosphorus (n-type dopant) and boron (p-type dopant) by using broadband electrostatic force microscopy, which were imaged with scanning microwave microscopy (SMM) [37]. *AlCl*<sub>3</sub> and *BCl*<sub>3</sub> are also investigated as a molecular precursor for the incorporation on Si(100) for atomically precise acceptor-based devices both experi-

mentally and theoretically [38, 39]. And the controlled doping of P atoms in Si(001) has been realized by using  $PH_3$  with the accuracy arround 1nm [40], which makes a great progress towards fulfilling the requirement of the precision in Kane's proposal [2]. An alternative way to realized the controlled doping by using arsenic is also achieved in 2020 [41]. Now the high precision of deterministic doping can be achieved as the dopant will take the place of the silicon atom in two nearest cells. Although the surface chemistry needed for deterministic implantation of more complex structures has not yet been developed, it is timely to investigate the potential structures that could be produced, and the potential role of the spin-orbit interaction in their electronic properties.

# 1.5 Introduction to topological insulators and topological invariants

As mentioned in §1.1, robust qubits are required for a quantum computation. One of the way to achieve that is encoding the information onto some stable states which are robust enough towards outside influence. One of the candidates is the topological state, which is symmetry-protected and will be more stable than the trivial states. The symmetry-protected topological order is a kind of order in zero-temperature quantum-mechanical states of matter that have a symmetry and a finite energy gap. There the symmetry protected properties of states can only be lost when the symmetry is broken. The trivial states will have same topology as the vacuum, while the non-trivial states have different topology. As what we will show in §3.2.2, changing of the potential from the surrounding can introduce edge states into the system in the trivial case, while non-trivial states will always localize at some particular place. In general, topologically ordered states have special properties like they contain non-trivial edge states, which become perfect conducting channel that can conduct electricity without generating heat. Based on that, we have the topological insulators. These insulators have non-trivial symmetry-protected topological order, so the conductive surface state, which makes the electrons can only move along the material surface, are protected by the particle number conservation and time-reversal

symmetry. This kind of insulators can be characterized by the topological invariants, so we can identify them by calculating a suitable topological invariant for the system.

One of the topological invariants is the Zak phase. For a 1D system, the calculation of the Zak phase can be transformed to the integration of the Berry connection over the first Brillouin zone. This quantity was defined in the previous paper [42, 43] as

$$Z = i \int_{\text{first BZ}} dk \langle u_k | \partial_k u_k \rangle \tag{1.6}$$

where  $u_k$  is the eigenvector of the Bloch Hamiltonian at wavevector k. When the Zak phase is 0 modulo  $2\pi$ , we expect the system to be topologically trivial and the corresponding finite chain to have no topological edge state, whereas when the Zak phase is  $\pi$  modulo  $2\pi$ , the system is topologically non-trivial and the corresponding finite chain supports topological edge states. As it is the integration of the Berry connection over the first Brillouin zone, the Zak phase is invariant (modulo  $2\pi$ ) under gauge transformations of the form  $|u_k\rangle \to e^{i\beta_k}|u_k\rangle$  [44].

Another invariant used in the thesis is the  $Z_2$  invariant based on the time-reversal symmetry [45]. In two dimensional case we have the possibility to form topological insulators, where robust edge states are rigorously protected by time-reversal symmetry. In systems with inversion symmetry, the calculation of parity can also be used as a diagnostic for the existence of this topological state: according to a previous paper [45], the  $Z_2$  invariant v (which takes the value 0 for trivial states and 1 for non-trivial states) can be obtained from the parity of occupied bands by using

$$(-1)^{\nu} = \prod_{i} \delta_{i} = \prod_{i} \prod_{m=1}^{N} \xi_{2m}(\Gamma_{i}), \qquad (1.7)$$

where  $\xi_{2m}(\Gamma_i) = \pm 1$  is the parity of the time-reversed state pair 2m (or 2m-1) at time-reversal symmetric point i. When v=1, the system has odd parity and there exist non-trivial topological edge states; When v=0, the system has even parity and there only exist trivial topological states. To determine the value of v in

two dimensions, only the four distinct time-reversal-invariant points in momentum space need to be taken into account:  $i \in \{(0,0),(0,\pi),(\pi,0),(\pi,\pi)\}.$ 

For the interacting system, we can also achieve the evidence for the non-trivial topological states by examining the symmetries of the edge states in the light of the classification of the topological phases of one-dimensional interacting fermions proposed by Reference [46]. In that paper, the time-reversal symmetry leads to additional distinctions between different phases. All possible phases of fermions can be classified into 8 categories by using three given parameters  $\mu, \phi, \kappa$ . The definitions for those parameters are shown below.

$$Q^A Q^B = e^{i\mu} Q^B Q^A \tag{1.8}$$

$$Q^A T = e^{i\phi} T Q^A \tag{1.9}$$

$$U^{A}(U^{A})^{*} = U^{B}(U^{B})^{*} = exp(i\kappa)\mathbf{1}$$
 (1.10)

Here Q is the fermion parity operator,  $Q^A$  and  $Q^B$  are local operators acting on the ends of the segment which satisfy  $(Q^A)^2 = (Q^B)^2 = 1$ , T is the time-reversal operator,  $U^A$  and  $U^B$  are the unitary transformations acting on the ends of the segment which satisfy

$$T|\alpha\beta\rangle = \sum_{\alpha',\beta'} U_{\alpha'\alpha}^A U_{\beta'\beta}^B |\alpha'\beta'\rangle \tag{1.11}$$

and  $[U^A, U^B] = 0$ ,  $\alpha$  and  $\beta$  enumerate the states associated with the two edges. After calculating these parameters for the edge state, we can know whether the state is topologically non-trivial or not by checking the table offered in Reference [46].

#### 1.6 Outline of the structure for the rest of thesis

In this thesis, we construct a linear combination of atomic orbitals (LCAO) model for deterministically placed acceptors in silicon, and develop three different multi-hole models (including hole-hole Coulomb interactions) with one hole per acceptor along low-index crystallographic directions (they are [001], [110] and [111] for

one dimensional system) based on that: the full configuration interaction calculation (full CI, in §4.1.1), the Heitler-London approximation (HL approximation, in §4.1.1) based on the full CI calculation but with a restricted basis, and the unrestricted Hartree-Fock method (UHF method, in §4.1.2) which represents the multihole state by a Slater determinant of one-hole states.

We first compute the electronic structure of the single acceptor in silicon by using the cubic model in Chapter 2; our results confirm the significant improvement due to the inclusion of the cubic term. Based on these single-acceptor calculations, we have selected an appropriate basis set of single-acceptor electronic states and performed calculations on acceptor pairs and linear chains by using a linear combination of atomic orbitals (LCAO) approach within an independent-hole model in Chapter 3. Our results suggest an interesting interplay between electrostatic effects and topological edge state in finite chains.

Then we introduce hole-hole Coulomb interactions into the system and begin the calculations of the multi-hole cases in Chapter 4. Some limitations of the full CI calculation and the HL approximation are discussed in §4.1.1. We study dimerised chains with staggered bond lengths  $d_1$  and  $d_2$  and concentrate on a 'small-separation' case with  $d_1 + d_2 = 3a_0$  and a 'large-separation' case with  $d_1 + d_2 = 6a_0$  where  $a_0$  is the effective Bohr radius; we show that both the HL approach and the UHF method are accurate approximations to the ground state of the fully exact CI calculation for these finite-length linear chains. We investigate the energy spectrum obtained from full CI for a 4-acceptor chain and explain the ground state in terms of the formation of edge states; we also relate an anti-crossing in the [001] direction for the small-separation case to the behavior of the Fock matrix eigenvalues obtained from the UHF method. We analyse the symmetries of the states produced by symmetry breaking in the UHF solution, and present evidence for the existence of non-trivial many-body edge states in the finite chain system. We point out that the UHF method can be applied to a linear chain with periodic boundary conditions, and calculate the band structure formed by the Fock matrix eigenvalues. We also analyse the topological phases of the system based on two methods: first, a method focusing on

the edge states of finite one-dimensional interacting Fermionic systems, and second, the Zak phase [43] for an infinite non-interacting system.

After getting the valid models for both non-interacting case and interacting case in one dimensional system, we apply those methods on two dimensional system in Chapter 5. We calculate the energy states for the finite rectangle arrangements as well as the band structures for periodic boundary condition cases under both the one-hole model and the multi-hole model. For the one hole model, we campare 2D systems with one dimensional systems, and find some states localized at particular acceptors due to the nonequivalent potential. We also find the evidence for the existence of the non-trivial topological edge states. For the multi-hole model, we compared the full CI result with the UHF one, and investigate the distribution of the holes there. Then we investigate the topological property of edge states in the infinite honeycomb lattice by calculating the  $Z_2$  invariant mentioned in §1.5. We also consider the acceptors in the real doped silicon lattice to predict the behavior of acceptors in the experiment.

### **Chapter 2**

### The Single Acceptor Problem

### 2.1 Single-acceptor cubic model

Within effective mass theory [3], the Hamiltonian for an isolated acceptor contains spherical and non-spherical (cubic) parts. Including all the terms, we can obtain a cubic model. Here we should point out that the cubic symmetry is introduced by the effective mass approximation, while the defect itself has terahedral ( $T_d$ ) symmetry. This is unavoidable when effective mass theory is applied. In the effective mass the Coulomb potential around the defect is different from the real case, so the this model is invalid for very small separations. But we can still expect the results for the other separations are accurate enough.

In this thesis, we take the general form of the cubic model (valid for arbitrary spin-orbit coupling) as follows,

$$\hat{H}_{c} = \frac{p^{2}}{\hbar^{2}} - \frac{2}{r} - \frac{\mu}{3\hbar^{2}} (P^{(2)} \bullet I^{(2)})$$

$$+ \frac{2}{3} \Delta (\frac{1}{2} - \vec{I} \bullet \vec{S}) + \frac{\delta}{3\hbar^{2}} ([P^{(2)} \times I^{(2)}]_{4}^{(4)} + \frac{\sqrt{70}}{5} [P^{(2)} \times I^{(2)}]_{0}^{(4)} + [P^{(2)} \times I^{(2)}]_{-4}^{(4)})$$

$$(2.1)$$

where p is the hole linear momentum operator,  $\mu$  is the strength of the spherically symmetric heavy-hole light-hole coupling,  $\Delta$  is the spin-orbit coupling, and  $\delta$  is the strength of the cubic term [7]. The tensor operators  $P^{(2)}$  and  $I^{(2)}$  are as defined in previous studies of acceptors [6]:  $P_{ik} = 3p_ip_k - \delta_{ik}p^2$  contains the hole (linear)

momenta, while  $I_{ik} = \frac{3}{2}(I_iI_k + I_kI_l) - \delta_{ik}I^2$  is built from the angular momentum operators  $I_i$  of a spin-1 object (corresponding to the intrinsic orbital angular momentum of the p-orbitals comprising the valence band).  $\vec{I}$  is the corresponding vector of spin-1 angular momentum operators, while  $\vec{S}$  is the vector of spin- $\frac{1}{2}$  spin operators of the hole. In this model, we use the effective Rydberg  $R_0 = \frac{e^4 m_0}{2\hbar^2 \varepsilon_0^2 \gamma_1}$  and the effective Rydberg  $R_0 = \frac{e^4 m_0}{2\hbar^2 \varepsilon_0^2 \gamma_1}$ tive Bohr radius  $a_0 = \frac{\hbar^2 \varepsilon_0^2 \gamma_1}{e^4 m_0}$  as units of energy and length, respectively [6], where  $\varepsilon_0$  and  $m_0$  are the crystal dielectric constant and the free electron mass, respectively, and  $\gamma_1$  is the parameter proposed by Luttinger for the description of the hole dispersion relation near the center of the Brillouin zone [3]. Here the factor '2' above r arises due to the definition of  $R_0$ .  $[A \times B]_m^{(l)}$  denotes component m of the part of the spherical tensor product  $A \times B$  having rank l. For silicon, where the effective Rydberg  $R_0 = 24.8 \,\mathrm{meV}$  and  $a_0 = 2.55 \,\mathrm{nm}$ , we have the strength of the spherical term  $\mu = 0.483$ , the valence band spin-orbit splitting  $\Delta = 1.774R_0$ , and the cubic term  $\delta = 0.249$ . We note that the model is set up to describe electrons in the valence band, so the ground state for holes will appear at the top of the spectrum (i.e., with the largest positive eigenvalue). For convenience, we describe the state by the location of it in the figure shown in the thesis, for example, the highest state is the ground state.

For the convenience of the following discussion, here we give the definitions of the total angular momentum  $\vec{F}$ :  $\vec{F} = \vec{L} + \vec{I} + \vec{S} = \vec{L} + \vec{J}$ , where  $\vec{L}$  is the orbital angular momentum of the envelope function and  $\vec{J} = \vec{I} + \vec{S}$  is the total intrinsic angular momentum of a valence-band electron. Then we have the corresponding total magnetic angular momentum  $m_F$ . In the spherical case where the cubic term is neglected,  $\vec{F}$  is conserved. So eigenstates are characterised by quantum numbers F and  $m_F$ . So the spherical state for acceptors can be expanded as a linear combination of a group of states with spherical symmetry labeled by  $L, J, F, m_F$ . In the cubic model Equation 2.1, the cubic term couples states with  $\Delta m_F = 0, \pm 4$  where the cubic term is not zero [7], so the eigenstates are now labeled by irreducible representations of the cubic double group rather than by values of F. There are 6 fermionic representations,  $\Gamma_6^\pm, \Gamma_7^\pm, \Gamma_8^\pm$ ; states with these symmetries can be obtained by taking suitable

linear combinations of states with spherical symmetry.  $\Gamma_6^\pm$  are double degenerate states,  $\Gamma_7^\pm$  are six-fold degenerate states,  $\Gamma_8^\pm$  are four-fold degenerate states. For the convenience of further calculations, we use an underlying basis of Gaussian orbitals of spherical symmetry up to a maximum of L=3 and  $F=\frac{9}{2}$  (which we label as  $F_{\frac{9}{2}}$  states, corresponding to the usual notation in atomic physics). With the help of this Gaussian basis, the further calculations in the following chapters are able to be done easily as the formulas for the transition integrals and hole-hole interactions in Reference [47] can be applied. We compute the matrix elements of the Hamiltonian in this basis of spherically symmetric states. The spherically symmetric term is

$$\langle L', J', F, m_F | P^{(2)} \bullet I^{(2)} | L, J, F, m_F \rangle = (-1)^{L+J'+F} \begin{Bmatrix} F & J' & L' \\ 2 & L & J \end{Bmatrix} (L' || P^{(2)} || L)$$

$$\bullet (J' || I^{(2)} || J)$$
(2.2)

where the term with  $\{\}$  is the 6-j symbol, and the reduced matrix element  $(J' \| I^{(2)} \| J)$  can be obtained by the formula

$$(J' || I^{(2)} || J) = (-1)^{J + \frac{7}{2}} \sqrt{(2J+1)(2J'+1)} \begin{cases} 1 & J' & \frac{1}{2} \\ J & 1 & 2 \end{cases} (I' || I^{(2)} || I)$$
 (2.3)

The cubic symmetry term is

$$\langle L', J', F', m'_{F} | [P^{(2)} \times I^{(2)}]_{m}^{(4)} | L, J, F, m_{F} \rangle = 3(-1)^{F' - m'_{F}} \sqrt{(2F + 1)(2F' + 1)}$$

$$\bullet \begin{pmatrix} F' & 4 & F \\ -m'_{F} & m & m_{F} \end{pmatrix} \begin{cases} J' & J & 2 \\ L' & L & 2 \\ F' & F & 4 \end{cases}$$

$$\bullet (L' || P^{(2)} || L) (J' || I^{(2)} || J)$$

$$(2.4)$$

where the term with () is the 3-j symbol, and the term with {} is the 9-j symbol. Then we can transform these matrix elements into a set of basis functions belong-

ing to the irreducible representations of the cubic double group by the projectors connected the  $|L,J,F,m_F\rangle$  basis and the cubic symmetry basis. It can be achieved by the formula offered in the projection operator section in reference [48]. Diagonalizing the projectors and applying the eigenvectors corresponding to the non-zero eigenvalue to the  $|L,J,F,m_F\rangle$  basis, we will get the Hamiltonian under the cubic symmetry basis. The eigenfunctions of the Hamiltonian (2.1) can be solved by expanding the cubic states in terms of Gaussian functions [7]. The resulting cubic states are then used as the basis for the following chapters. For the convenience of the discussion in the next section, we take the  $\Gamma_8^+$  state as an example to show the structure of the state.

$$\Phi(\Gamma_8^+) = f_1(r) \left| L = 0, J = \frac{3}{2}, F = \frac{3}{2}, m_F \right\rangle 
+ f_2(r) \left| L = 2, J = \frac{3}{2}, F = \frac{3}{2}, m_F \right\rangle 
+ f_3(r) \left| L = 2, J = \frac{1}{2}, F = \frac{3}{2}, m_F \right\rangle 
+ f_4(r) \left| L = 2, J = \frac{3}{2}, F = \frac{5}{2}, m_F \right\rangle 
+ f_5(r) \left| L = 2, J = \frac{1}{2}, F = \frac{5}{2}, m_F \right\rangle 
+ f_6(r) \left| L = 4, J = \frac{3}{2}, F = \frac{5}{2}, m_F \right\rangle 
+ f_7(r) \left| L = 2, J = \frac{3}{2}, F = \frac{7}{2}, m_F \right\rangle 
+ f_8(r) \left| L = 4, J = \frac{3}{2}, F = \frac{7}{2}, m_F \right\rangle 
+ f_9(r) \left| L = 4, J = \frac{1}{2}, F = \frac{7}{2}, m_F \right\rangle$$
(2.5)

where  $f_i(r)$  is the radial part which can be expanded in terms of Gaussian functions (shown in the next section), and  $|L,J,F,m_F\rangle$  is the angular part.

### 2.2 Single acceptor result

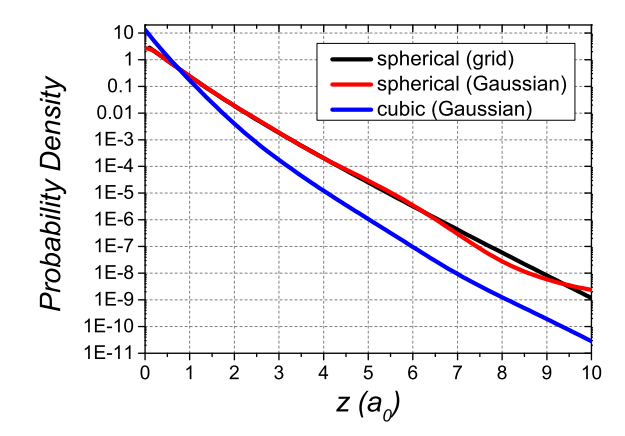
The single-acceptor problem can be solved by expanding the wave function of the eigenstates in terms of Gaussian functions [6, 7]. The radial parts of the states (such

Spherical state	Spherical result	Cubic state	Cubic result
$1S_{\frac{3}{2}}$	1.356041	$1\Gamma_8^+$	1.868314
$2P_{\frac{3}{2}}$	0.456253	$1\Gamma_6^+$	0.930278
$2S_3$	0.360829	$1\Gamma_0^-$	0.717426

 $2\Gamma_8^+$ 

0.538586

**Table 2.1:** The highest four single acceptor eigenenergies obtained from the Gaussian expansion for Si; the energy unit is the effective Rydberg  $R_0$ .



0.314359

 $\overline{2}P_{\underline{5}}$ 

**Figure 2.1:** The total probability density of the ground state wavefunctions with different approximations for a single acceptor along z-axis ([001] direction) in Si under the one-hole model. The black line is for the results by solving on the grid under the spherical model. The red line is for the results from Gaussian expansion under the spherical model. The blue line is for the results from Gaussian expansion under the cubic model.

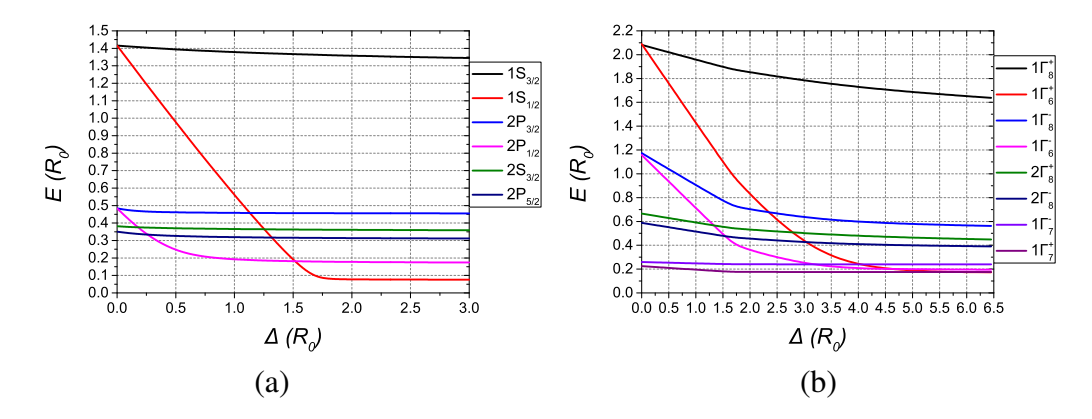


**Figure 2.2:** The behavior of the eigenstates as a function of  $\Delta$  with  $\mu = 0.483$  and  $\delta = 0.249$  (the values in Si): (a) the energy spectra for the spherical case, (b) the energy spectra for the cubic case. Note that some states of other symmetries are not shown, and  $\Delta = 1.774R_0$  for silicon.

as  $f_i(r)$  in Equation 2.5) are expanded as

$$f_i(r) = r^l \sum_i A_i e^{-\alpha_i r^2}, \tag{2.6}$$

where l is the orbital angular momentum of the envelope function and  $\alpha_i$  is a Gaussian exponent. We use 21 Gaussian functions, with exponents  $\alpha_i = \frac{5 \times 10^5}{2.42632^{i-1}}$  for both single acceptor case in this chapter and one-hole model in the next chapter. Here we take the number 2.42632 to make the exponents drop in the same range  $(\alpha_1 = 5 \times 10^5, \alpha_{21} = 0.01)$  as shown in the previous paper [6]. This group of exponents has been tested by comparing with the experimental ionization energies [6, 7], so it should provide reliable results here.

We will use the highest four states as a basis for further calculations of the pair and the acceptor chain to include the influence from near excited states; the states and their energies in the spherical and cubic cases are shown in Table 2.1. The spherical results have been benchmarked against an exact solution of the radial equation in my MSc project [49], which shows this method can provide very good results. We note that the states in the cubic case are systematically more strongly bound than those in the spherical case, and we expect they will have correspondingly shorter decay lengths. This is supported by Figure 2.1, which shows the total probability of the ground state wave functions with different approximations for a single acceptor along z-axis; the more rapid decay in the cubic case is apparent. Here we can also see that the results from Gaussian expansion under the spherical model is very close to the results by solving on the grid under the same model, which support that Gaussian expansion is a valid approximation towards solving on the grid.

We also show the behavior of the eigenstates in the spherical and cubic cases as the spin-orbit coupling  $\Delta$  changes, for fixed  $\mu$  and  $\delta$  ( $\mu=0.483$ ,  $\delta=0.249$ ), in Figure 2.2. As  $\Delta\to 0$ ,  $\vec F=\vec L+\vec I+\vec S$  is not the only conserved quantity; instead,  $\vec S$  and  $\vec L+\vec I$  are separately conserved. So, the  $1S_{\frac{3}{2}}$  and  $1S_{\frac{1}{2}}$  states converge to the  $1S_1$  state of the orbital-only model (where the suffix now refers to the value of  $\vec L+\vec I$ ); similarly  $2S_{\frac{3}{2}}$  converges to the  $2S_1$  state,  $2P_{\frac{1}{2}}$  and  $2P_{\frac{3}{2}}$  will converge to the

 $2P_1$  state, and  $2P_{\frac{5}{2}}$  will converge to the  $2P_2$  state; the  $1S_1$ ,  $2S_1$ ,  $2P_1$  and  $2P_2$  states were discussed for weak spin-orbit coupling in the previous paper [6]. Similarly, in the cubic case without spin-orbit coupling, the symmetries reduce to  $\Gamma_n^{\pm} \otimes \Gamma_6^+$  (where  $\Gamma_n^{\pm}$  denotes the symmetry of the orbital part in the cubic potential, including the envelope function and the orbital angular momentum of the atomic p states, and  $\Gamma_6^+$  is the symmetry of a single spin-1/2). Compared with the results in the previous paper [8], the cubic case behaves very similar towards the one with the central cell correction. As the calculation with the central cell correction generally agree with the experiment results, our results should also conform to experiments.

### 2.3 Summary

In this chapter, we followed the method in the previous paper [6], and achieved the eigenvalues and eigenvectors by choosing a group of proper Gaussian exponents. In the next chapter, we will use these results to do the calculation with more acceptors in one dimensional within the independent-hole approximation.

### **Chapter 3**

# One-hole Model In One-dimensional Systems

In this chapter we will investigate the acceptors in one-dimensional system under the independent-hole model. In this thesis, we call it 'one-hole model' as it does not include the hole-hole interactions. We will build a linear combination of atomic orbitals (LCAO) model, by expanding the mutli-acceptor wavefuntion as a linear combination of the single acceptor wavefunctions. The transitions between the next nearest neighbours will be considered here. The linear acceptor chain will be studied including both the finite chain and the chain with a periodic boundary condition. The energy states for the finite system and the band structure of the infinite system will be calculated. And we will try to investigate the topological property of the system mentioned in §1.5.

#### 3.1 One-hole model

### 3.1.1 A pair of acceptors

For the case of a pair of acceptors, a calculation for a fully interacting two-hole model has recently been reported in the Heitler-London limit [9], but it is challenging to extend this approach to systems with more than two acceptors. We therefore introduce an independent-hole model to simplify the calculation, where we initially assume that there is only one hole in the acceptor pair. The single-hole system can be written as  $A_2^-$ , where A stands for the acceptor (compare the  $H_2^+$  molecule, which

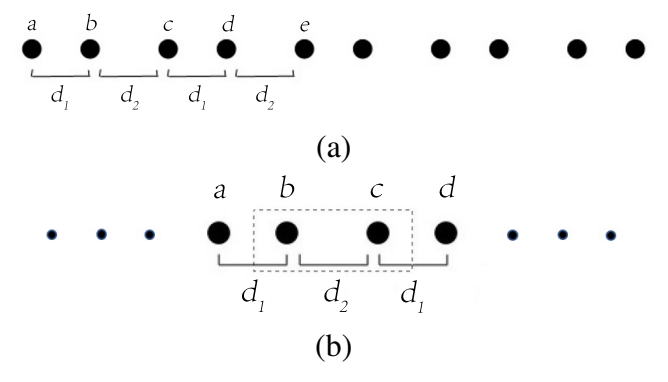


**Figure 3.1:** (a) Schematic of the 10-acceptor finite chain. (b) The unit cell of the infinite chain; atoms b and c are in the same cell. The letters a, b, c, d and e label the acceptors. We refer to  $d_1 < d_2$  as the 'short-long' case, and  $d_1 > d_2$  as the 'long-short' case.

contains a single electron). In this case, the Hamiltonian in scaled Rydberg units  $(R_0 = \frac{e^4 m_0}{2\hbar^2 \varepsilon_0^2 \gamma_1})$  is

$$\hat{H}_{s,c}^{\text{pair}} = \hat{H}_{s,c}^A - \frac{2}{r_B} = \hat{H}_{s,c}^B - \frac{2}{r_A}$$
 (3.1)

where  $H_A$  and  $H_B$  are the Hamiltonians of a single acceptor A and a single acceptor B (which may be written either in the spherical approximation or including cubic terms). Here the factors '2' above  $r_A$  and  $r_B$  arise also due to the definition of  $R_0$ . Then we can easily obtain an expression for the off-diagonal matrix element (or transition strength) in the basis of single-acceptor eigenstates

$$\langle \phi_A | \hat{H}^{\text{pair}} | \phi_B \rangle = \frac{1}{2} (E_A + E_B) \langle \phi_A | \phi_B \rangle - \langle \phi_A | \frac{1}{r_A} | \phi_B \rangle - \langle \phi_A | \frac{1}{r_B} | \phi_B \rangle$$
 (3.2)

$$\langle \phi_{A}^{'} | \hat{H}^{\text{pair}} | \phi_{A} \rangle = \langle \phi_{A}^{'} | H_{A} - \frac{2}{r_{B}} | \phi_{A} \rangle = E_{A} \langle \phi_{A}^{'} | \phi_{A} \rangle - \langle \phi_{A}^{'} | \frac{2}{r_{B}} | \phi_{A} \rangle$$
(3.3)

where  $E_A$  and  $E_B$  are the single acceptor eigenvalues, and  $\phi_A$ ,  $\phi_B$  are the corresponding single-acceptor eigenstates.

Using Equations 3.2 and 3.3, we can obtain the transition strength between any single-acceptor states on any sites. The single-hole energies can then be found by solving a generalised eigenvalue problem provided we can compute the overlap  $\langle \phi_A | \phi_B \rangle$  and the potential term  $\langle \phi_A | \frac{1}{r_i} | \phi_B \rangle$ . We follow the methods in the previous

paper [47] to get the matrix elements between the Gaussian orbitals, then times the relevant Gaussian coefficients of the single-acceptor states and sum them to get the matrix elements under the Cartesian basis. Reference [47] gives the result for states up to P orbitals, while the results for higher angular momenta can be obtained by taking further derivatives along the different axis. Than with the help of spherical harmonics, the Cartesian basis can be transformed to the  $|L, m_L, J, m_J\rangle$  basis, which can be transformed to the  $|L, J, F, m_F\rangle$  basis by using relevant Clebsch–Gordan coefficients. The projectors connected the  $|L, J, F, m_F\rangle$  basis and the cubic symmetry basis can be achieved by the formula offered in the projection operator section in reference [48]. Diagonalizing the projectors and applying the eigenvectors corresponding to the non-zero eigenvalue to the  $|L, J, F, m_F\rangle$  basis, we will get the Hamiltonian matrix and overlap matrix under the cubic symmetry basis.

This approach becomes exact as (i) the number of single-acceptor states used and (ii) the number of Gaussian functions used to represent each one both tend to infinity. Since we are interested in the states close to the ground state in silicon, we use only the highest 4 single-acceptor states  $(1S_{\frac{3}{2}}, 2S_{\frac{3}{2}}, 2P_{\frac{3}{2}}, 2P_{\frac{5}{2}})$  for the spherical case and  $1\Gamma_8^+$ ,  $2\Gamma_8^+$ ,  $1\Gamma_6^+$ ,  $1\Gamma_8^-$  for the cubic case) in our basis, as the others are far away from them in energy. For the spherical case the different total angular momenta are mixed in the array but the projection  $m_F$ , for which the quantisation axis is chosen along the inter-acceptor axis, remains a good quantum number. For the cubic case, with a general axis direction states of all symmetries are mixed; however time-reversal symmetry guarantees the states still appear in Kramers doublets, which can be thought of as derived from the  $m_F = \pm \frac{1}{2}$  and  $m_F = \pm \frac{3}{2}$  pairs in the spherical case.

### 3.1.2 Linear acceptor-chain and LCAO model

From the one-hole model in §3.1.1, we can develop a similar linear combination of single-acceptor states to describe a finite linear chain of acceptors by similarly adding the potential terms from neighbouring dopants ( $V_{\text{potential}}$ ) into the single-

acceptor Hamiltonian.

$$\hat{H}_{s,c}^{\text{chain}} = \hat{H}_{s,c}^A - \frac{2}{r_B} + \hat{V}_{\text{potential}} = \hat{H}_{s,c}^B - \frac{2}{r_A} + \hat{V}_{\text{potential}}$$
(3.4)

Here we show the transition elements used in the finite chain calculation. The subscript indicates the acceptor on which the state involved in the transition is centered. The labels of the acceptor are same as the ones in Figure 3.1 (a)

$$t_{aa} = E_a S_{aa} + V_b \tag{3.5}$$

$$t_{ab} = \frac{1}{2}E_aS_{ab} + \frac{1}{2}E_bS_{ab} + \frac{1}{2}V_a + \frac{1}{2}V_b + V_c$$
 (3.6)

$$t_{ac} = \frac{1}{2}E_aS_{ac} + \frac{1}{2}E_cS_{ac} + \frac{1}{2}V_a + V_b + \frac{1}{2}V_c + V_d$$
 (3.7)

$$t_{bb} = E_b S_{bb} + V_a + V_c (3.8)$$

$$t_{bc} = \frac{1}{2}E_bS_{bc} + \frac{1}{2}E_cS_{bc} + V_a + \frac{1}{2}V_b + \frac{1}{2}V_c + V_d$$
 (3.9)

$$t_{bd} = \frac{1}{2}E_bS_{bd} + \frac{1}{2}E_dS_{bd} + V_a + \frac{1}{2}V_b + V_c + \frac{1}{2}V_d + V_e$$
 (3.10)

Here  $E_i$  is the single-acceptor energy of the state on atom i,  $S_{ij}$  is the overlap matrix between the states on atom i and atom j,  $V_i$  is the potential matrix of atom i. Here  $t_{aa}$ ,  $t_{ab}$  and  $t_{ac}$  are for the acceptor at the end of the chain,  $t_{bb}$ ,  $t_{bc}$  and  $t_{bd}$  are for the acceptor in the middle of the chain.  $t_{bb}$ ,  $t_{bc}$  and  $t_{bd}$  are also used in the infinite chain calculation.

However, the basis states on different acceptors are not orthogonal and hence the overlap matrix *S* must be included in the construction of the LCAO model. This requires that all the eigenvalues of the overlap matrix must be positive, in order to obtain a well defined generalised eigenvalue problem. Approximations to the overlap matrix, for example truncating it after a finite number of neighbours, may destroy the positive-definiteness of *S* and make it impossible to solve the eigenvalue problem. This is a problem particularly for small separations, as we will show in §3.2.2. To minimise this problem, we include in the calculation the influence of the next nearest neighbour by considering the matrix elements between each acceptor and its next nearest neighbour in both the transition matrix and the overlap matrix.

We will see that the influence from the third neighbours should be small under the arrangement of the chain in the acceptor-pair calculation in §3.2.1.

For definiteness we focus on the 10-acceptor finite chain shown in Figure 3.1 (a), where we label the first five acceptors from one end by a, b, c, d, and e. We assume that the separations appear periodically as shown in Figure 3.1 (a), so the chain possesses a dimerisation that can be varied by changing the separations  $d_1$  or  $d_2$ . Under this arrangement, it is easier to investigate the topological behaviors.

We refer to the single-hole model including interactions with the next nearest neighbours as the 'long-range' model. This is expected to be a good model for a single hole bound to an array of acceptors and in this case the long-range Coulomb interactions have an important effect on the physics (as shown in §3.2.2). However, we may also wish to understand the behaviour of clusters which are at or close to charge neutrality and hence contain many holes (for example, one hole per acceptor), but the motion of the holes is approximately independent of each other. In that case we expect that the motion of the other holes will effectively screen out these long-range interactions, so we adopt as our approximation to this charge-neutral case a 'short-range' model where the effect of the Coulomb potential term ( $V_{\text{potential}}$ ) in Equation (3.4) is removed. So the Coulomb potential from the surrounding acceptors is removed, while the part from the acceptors involved in the transition is retained. Corresponding to the potential, we also take out the next nearest transitions. So only the nearest transitions are considered in the 'short-range' model.

From the one-hole model in §3.1.1, we can also generate an LCAO model to describe the linear infinite acceptor-chain in the similar way. The general form of the Hamiltonian will has the same form as for the finite chain (Equation (3.4)). We assume each unit cell contains two acceptors as shown in Figure 3.1 (b). The intercell separation is taken as  $d_1$ , and the intra-cell separation is  $d_2$ . Since the system is periodic its eigenstates are labelled by a Bloch wavevector k, which we define so that the phase factor of the transition from left to right is  $e^{ik}$ , and that from right to left is  $e^{-ik}$ . We will consider the next nearest transitions here as well, so Equation (3.8), Equation (3.9) and Equation (3.10) also can be used in the calculations.

# 3.1.3 Zak phase calculation for a generalized eigenvalue problem

An indication of whether a given state in the finite chain system has a topological origin can be obtained by calculating the Zak phase for the corresponding infinite chain. For a generalized eigenvalue problem, the formula for the Zak phase in §1.5 becomes

$$Z = i \int_{\text{first BZ}} dk \langle u_k | S(k) | \partial_k u_k \rangle$$
 (3.11)

where  $u_k$  is the eigenvector of the Bloch Hamiltonian at wavevector k, S(k) is the overlap matrix. As previously, when the Zak phase is 0 modulo  $2\pi$ , we expect the system to be topologically trivial and the corresponding finite chain to have no topological edge state, whereas when the Zak phase is  $\pm \pi$ , the system is topologically non-trivial and the corresponding finite chain supports topological edge states. And Equation (3.11) is also invariant under gauge transformations.

### 3.2 One-hole model results

### 3.2.1 A pair of acceptors for the one-hole model

The behaviors of the eigenenergies for the spherical and cubic cases are shown as a function of acceptor separation r in Figure 3.2. The states all converge to one of the highest four states of a single acceptor as  $r \to \infty$ , and can roughly be understood as either bonding or anti-bonding combinations of the single-acceptor states; however, for the cubic cases this is complicated by crossings of the states. The splittings between the states set in at smaller values of r for the cubic case due to the stronger localization of the states in the cubic case.

Another important thing needs to be pointed out here is the long range interactions in the cubic case. The ground states in Figure 3.2 show that the eight-fold-degenerate ground state has already formed at  $r = 5a_0$  corresponding to two groups of four-fold-degenerate ground state for the single acceptor case. And the difference between the ground state energy here (around  $2.27R_0$ ) and the single acceptor

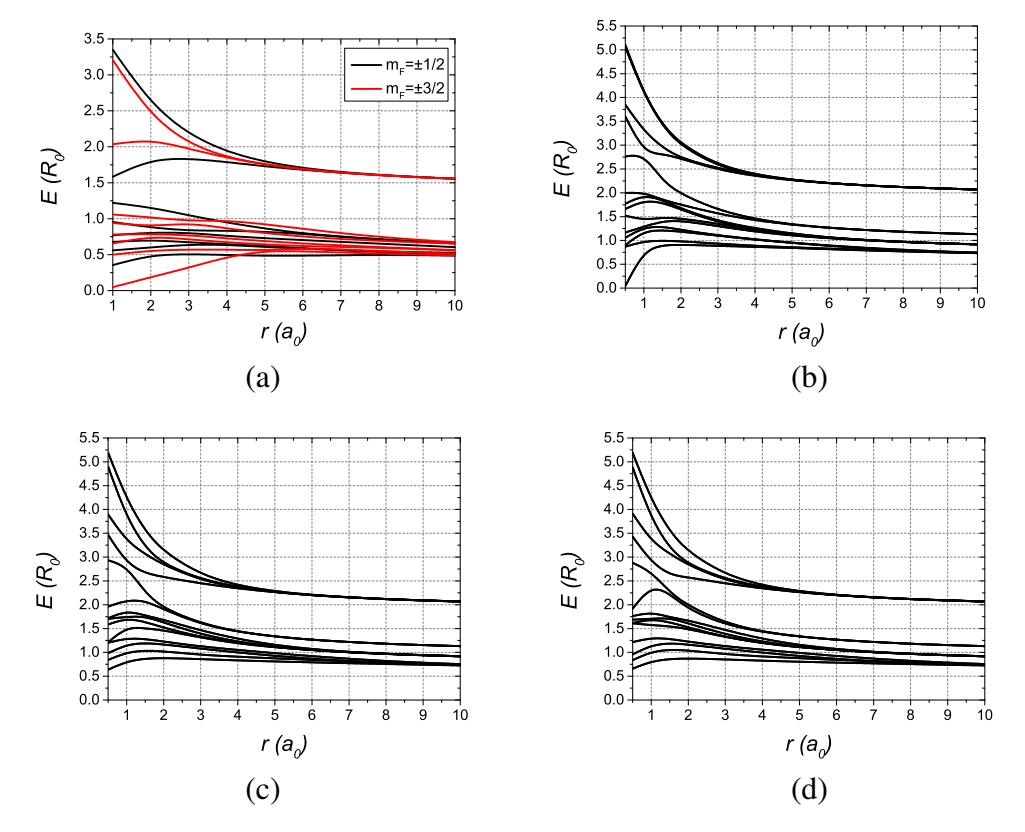


**Figure 3.2:** Eigenenergies in a pair of acceptors as a function of separation r for (a) the spherical case, and for the cubic case in (b) the [001] direction, (c) the [110] direction, (d) the [111] direction. In (a), the states with  $m_F = \pm 3/2$  ( $m_F = \pm 1/2$ ) are in red (black).

case  $(1.868314R_0)$  is very close to the interaction between the localized hole and the other acceptor core (hole-core Coulomb interaction,  $0.4R_0$ ). Consider there are two acceptors and each of them has a four-fold-degenerate ground state, the ground state energy behaves like two single acceptor with hole-core Coulomb interactions between them. So it is reasonable to believe that influence from the third neighbours should also be small in the linear chain under the chosen arrangements in §3.2.2 (the separations towards the third neighbour is at least  $8a_0$  for the cubic case) as only the hole-core Coulomb interaction between them can be identified there.

### 3.2.2 Finite linear acceptor-chain

As our LCAO model does not contain the influence of all the acceptors in the chain, the overlap matrix S is not guaranteed to be positive definite. For example, the behavior of the smallest eigenvalue of the overlap matrix for a 10-acceptor finite

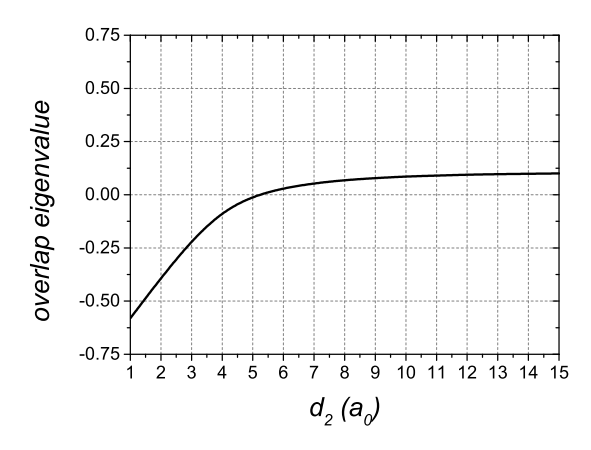


**Figure 3.3:** The smallest eigenvalue of the overlap matrix, truncated at next-nearest-neighbours, for a 10-acceptor finite chain in the spherical model with  $m_F = \pm \frac{1}{2}$  as a function of separation  $d_2$  when  $d_1 = 4a_0$ . Note the appearance of unphysical negative eigenvalues when  $d_2 \le 6a_0$ .

**Table 3.1:** The symmetry for the ground state under the cubic model.

System	Group	Symmetry
Single Acceptor	$O_h$	$\Gamma_8^+$
Pair/Chain([001] direction)	$D_{4h}$	$\Gamma_6^{\pm}, \Gamma_7^{\pm}$
Pair/Chain([110] direction)	$D_{2h}$	$\Gamma_5^\pm$
Pair/Chain([111] direction)	$D_{3d}$	$\Gamma_4^{\pm}, \Gamma_5^{\pm}, \Gamma_6^{\pm}$

chain in the spherical model (truncated at the next-nearest-neighbour) when  $m_F = \pm \frac{1}{2}$  as a function of the acceptor separation  $d_2$  when  $d_1 = 4a_0$  is shown in Figure 3.3. It can be seen that, even with the influence of the next-nearest-neighbour included, S ceases to be positive definite for separations  $d_2 < 6a_0$ . The next-next nearest term and the following terms are small compared to the next-nearest-neighbour ones, so adding them only improves the description of the system a little but significantly increases the cost of the calculation. Therefore, we only include the next-nearest-neighbour terms in our model, and restrict our calculations so we do not enter the parameter regions where the corresponding S matrix is not positive definite. For the spherical case we require that one of the separations is larger than  $4a_0$  and the other is no smaller than  $6a_0$ ; for the cubic case (where the basis states are more localised) we require that one of the separations is larger than  $2a_0$  and the other is no smaller than  $4a_0$ . From now on, we refer to the case  $d_1 < d_2$  as the short-long arrangement, to  $d_1 = d_2$  as the uniform chain, and to  $d_1 > d_2$  as the long-short arrangement.

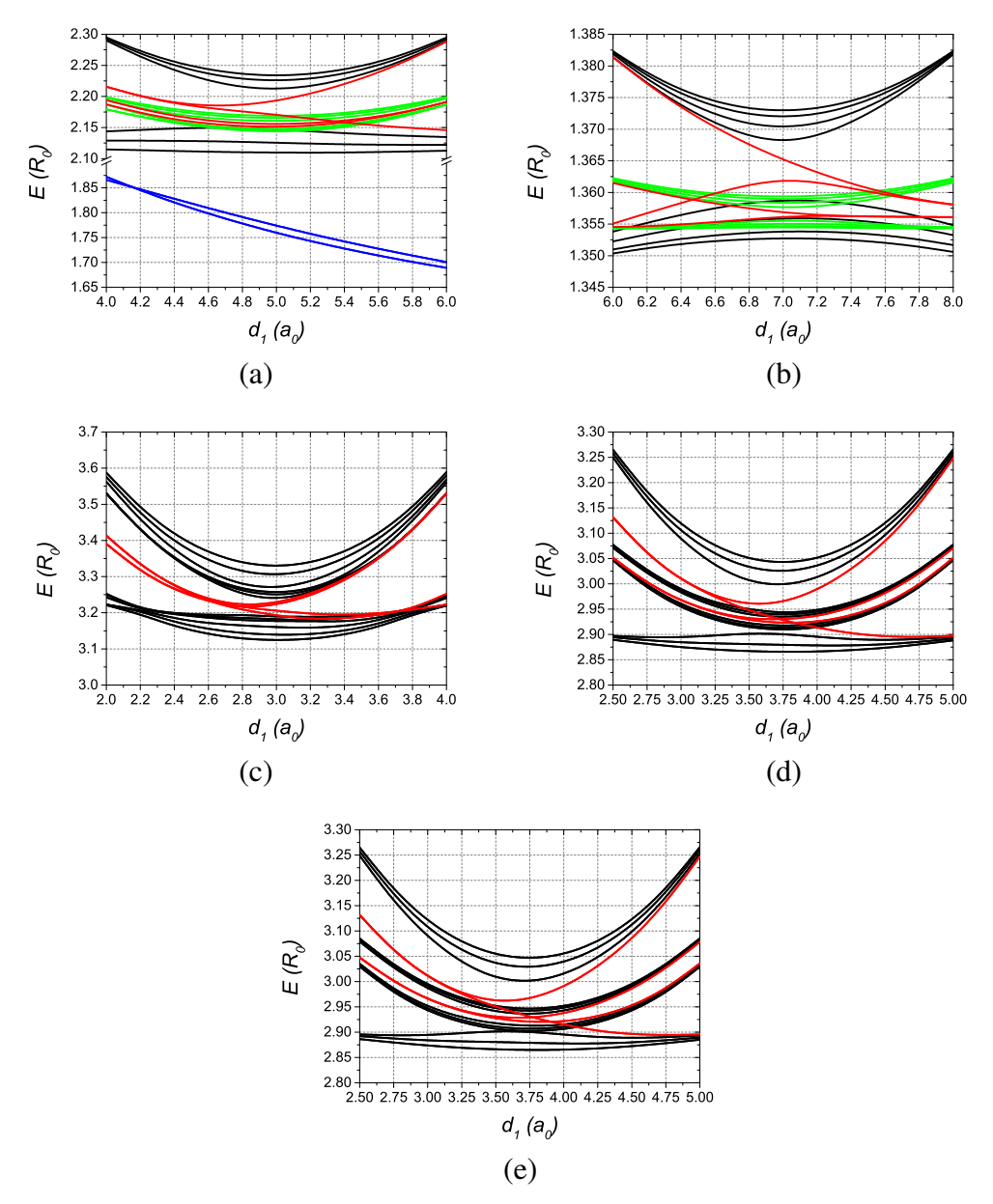


**Figure 3.4:** The highest few energy states as a function of  $d_1$  when  $d_1 + d_2$  is held constant. (a) the highest 40 energy states for the spherical case when  $d_1 + d_2 = 10a_0$ , (b) the highest 40 energy states for the spherical case in the short-range model without long-range potential when  $d_1 + d_2 = 14a_0$ , (c) the highest 32 states for the cubic case in the [001] direction when  $d_1 + d_2 = 6a_0$ , (d) the highest 32 energy states for the cubic case in the [110] direction when  $d_1 + d_2 = 7.5a_0$ , (e) the highest 32 energy states for the cubic case in the [111] direction when  $d_1 + d_2 = 7.5a_0$ . The red curves are the states splitting from the main bands and lying between them. For the spherical case shown in (a), the blue curves are the states that split from the main bands and lie below them; the black curves show states in the main bands for  $m_F = \pm \frac{1}{2}$ , the green-curve states in are the main bands for  $m_F = \pm \frac{3}{2}$ . The same colour-coding was also done for (b).

First, we fix the sum  $d_1 + d_2$  to a constant, choosing the values  $10a_0$  for the spherical model,  $6a_0$  for the cubic model in the [001] direction, and  $7.5a_0$  for the cubic model in the [110] and [111] direction (This is because the overlap matrix for the infinite chain is not positive definite in the [110] and [111] directions under the condition  $d_1 + d_2 = 6a_0$  — see §3.2.3). The behavior of the highest few energy states as a function of  $d_1$  under this condition is shown in Figure 3.4; we show the highest 40 energy states for the spherical case, and the highest 32 states for the cubic case. All these states are derived from the ground-state manifold in the single acceptor case. It can be seen that the eigenstates are arranged in groups that correspond to the bands in the infinite-chain model (see below). For the spherical case in Figure 3.4(a), the bulk states with  $m_F = \pm 1/2$  are shown in black and those with  $m_F = \pm 3/2$  in green, while pairs of states shown in red split off from these main bands. In each case a red nearly degenerate pair lies in the gap between main bands on one side of the diagram, and converges into two different bands on the other side. These states in red becomes each edge state on one side of the diagram. There are also other states that always lie below the main bands (the blue curves). We find that the blue states below the main band are localized at the end of the chain, and the red states between the main bands are localized on the acceptors next to the end of the chain. (The blue states are not shown for the cubic cases — we explain the reason below.)

Now let us investigate the electrostatic origin of the edge states below the main band. These states are introduced into our system because of the parabolic potential arising from the long-range interactions between the charges. This potential rises at the ends of the chain, reflecting the different environments of the acceptors in the middle and at the ends of the chain, so when we add a hole to either of the lowest two states among them, they will be localized at the ends. We can check the influence of the parabolic potential by comparing the results for the short-range model, where the long-range Coulomb interactions are absent. Without the long-range potential and the next nearest transitions, the system is less localized than the original one, so we can only have  $d_1 + d_2 = 14a_0$  while retaining a positive definite

overlap matrix. The behavior of the highest 40 energy states as a function of  $d_1$  under this condition is shown in Figure 3.4 (b). We see that the blue states below the main band disappear (This is also true for the short-range model in the cubic case, not shown). Since these edge states arise purely from electrostatic effects they are trivial (i.e. non-topological) states, and we do not show them in the graphs for the cubic cases.

Comparing Figure 3.4(a) and (b), we also see that the behavior of the red edge states associated with the  $m_F = \pm 1/2$  (black) bands in the spherical model reverses: for the long-range model (a) the states lie in the band gap for the short-long arrangement but join the bands in the long-short case, while the reverse is true in the short-range model (b). This is because the long-range electrostatic interactions effectively pull the end acceptors away from the bulk bands, transforming a chain ending with a long bond into one ending with a short bond and *vice versa*. This is also reflected in the different numbers of (black) band states with  $m_F = \pm 1/2$  in the two cases.

We can also see that the behavior of the red edge states associated with the  $m_F = \pm 3/2$  (green) bands in the spherical model does *not* reverse between the long-range and short-range cases, even though the number of states in each band changes just as for  $m_F = \pm 1/2$  as the electrostatic edge state is pushed back into the band. As we show in §3.2.3, this is a consequence of an anomalous variation of the effective transition amplitude with distance in the particular geometry considered; it is related to an anomalous behaviour of the topological Zak phase that is discussed in §3.2.3.

The calculations for the cubic cases (Figure 3.4 (c) to (e)) are performed in the long-range model, and the behaviour of the edge states (red) is similar to the long-range spherical model. For the [001] and [111] directions, the  $m_F = \pm 3/2$  and  $m_F = \pm 1/2$  bands of the spherical model evolve into states which retain different symmetries in the cubic environment; a red state can therefore cross all the states in a band having a different symmetry from its own. In the [110] direction, on the other hand, there is just one irreducible representation that is even under exchange of the acceptors and one that is odd, so a given red state will anti-cross (with states

**Table 3.2:** The Zak phase Z computed under a variety conditions for long-range model after mod  $2\pi$  in the spherical and cubic cases. 'First' means that the states correspond to the first curve at the top of the pictures in Figure 3.6, 'second' means that the states correspond to the second curve from the top of the pictures in Figure 3.6.

Arrangement	Long-short	Short-long
Spherical case with $m_F = \pm \frac{1}{2}$	0	$\pi$
Spherical case with $m_F = \pm \frac{3}{2}$	π	0
Cubic case in [001] direction (first)	0	π
Cubic case in [001] direction (second)	0	π
Cubic case in [110] direction (first)	0	π
Cubic case in [110] direction (second)	0	π
Cubic case in [111] direction (first)	0	π
Cubic case in [111] direction (second)	0	π

of the same symmetry) or cross (with states of the opposite symmetry) alternately as it passes through a band; we nevertheless color the red state continuously as if it crossed all the other states (the anti-crossings are hardly visible on the scale of Figure 3.4(d)). The relevant symmetries are shown in Table 3.1.

### 3.2.3 Linear chain with periodic boundary conditions

For the infinite chain, exchanging the value of  $d_1$  and  $d_2$  makes no difference on the system. So we only need to consider the short-long arrangement ( $d_1 \le d_2$ ) when  $d_1 + d_2$  is held constant. The band structures under different arrangements for two spherical cases (long-range and shrort-range) and the the cubic case in different directions when  $d_1 + d_2$  is fixed are shown in Figure 3.5; we show the highest 32 energy states for the spherical case, and the highest 28 states for the cubic case. We also show the detail of the highest 4 energy bands (those at the top of the graphs in Figure 3.5) in Figure 3.6. Each of them is double degenerated. Here k is the momentum, a is the lattice constant, and the blue line is the Fermi energy. The non-equivalent arrangement cases (left column in Figure 3.6,  $d_1 \ne d_2$ ) are insulators, while the uniform chain cases (right column in Figure 3.6,  $d_1 = d_2$ ) are metals. We should point out that the spherical case and the cubic case along the [110] direction are one-band metal, while the cubic cases along the [001] and [111] direction are two-band metal. There are gaps between the bands of states when  $d_1 \ne d_2$ , but these gaps close when  $d_1 = d_2$ , where the periodicity of the model halves and the size of

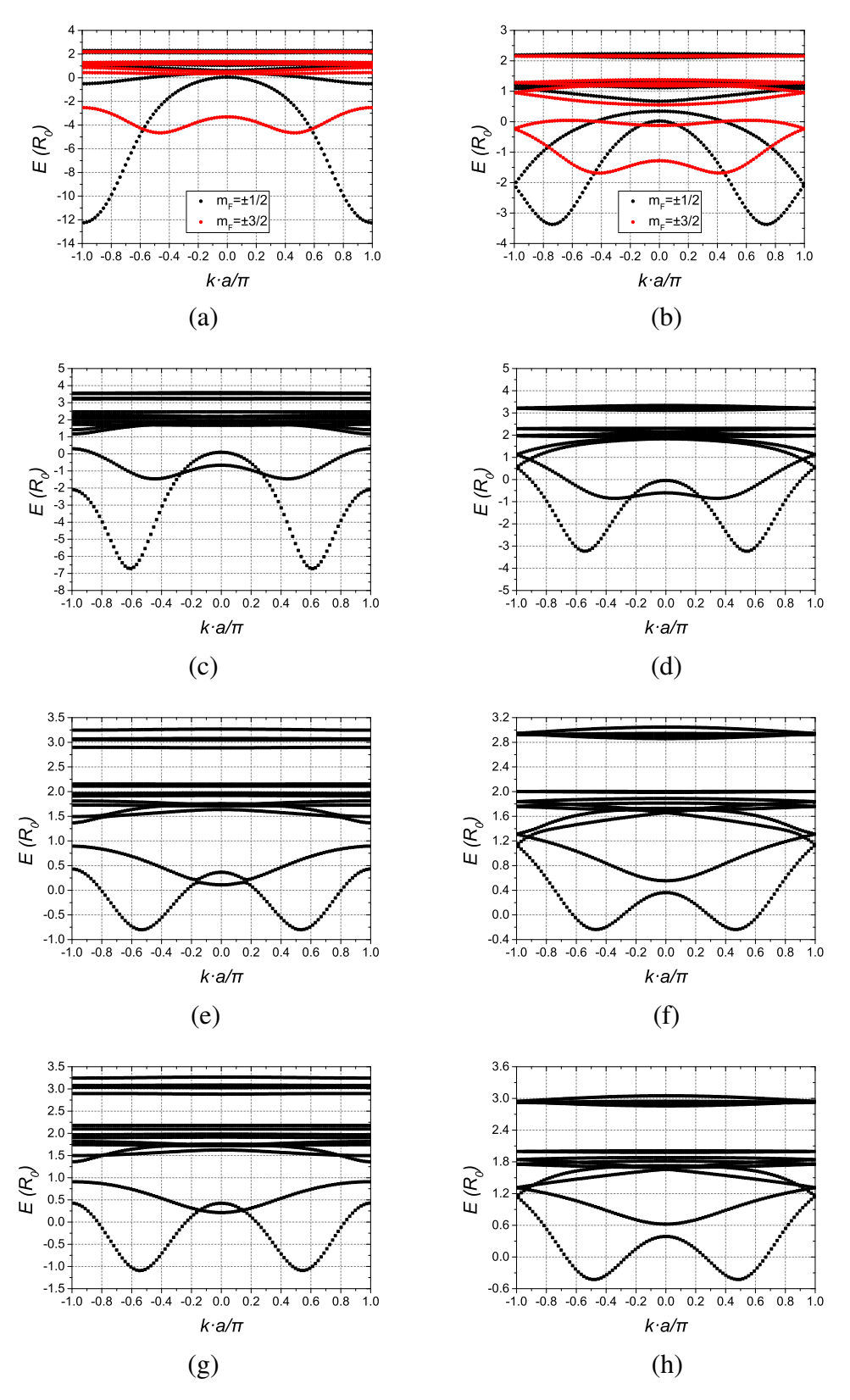


**Figure 3.5:** The band structure under different arrangements when  $d_1 + d_2$  is fixed. (a) the spherical case when  $d_1 = 4a_0$  and  $d_2 = 6a_0$ , (b) the spherical case when  $d_1 = d_2 = 5a_0$ , (c) the cubic case when  $d_1 = 2a_0$  and  $d_2 = 4a_0$  in the [001] direction, (d) the cubic case when  $d_1 = d_2 = 3a_0$  in the [001] direction, (e) the cubic case when  $d_1 = 2.5a_0$  and  $d_2 = 5a_0$  in the [110] direction, (f) the cubic case when  $d_1 = d_2 = 3.75a_0$  in the [111] direction, (g) the cubic case when  $d_1 = 2.5a_0$  and  $d_2 = 5a_0$  in the [111] direction, (h) the cubic case when  $d_1 = d_2 = 3.75a_0$  in the [111] direction. For the spherical model calculations, the states with  $m_F = \pm 3/2$  ( $m_F = \pm 1/2$ ) is in red (black).

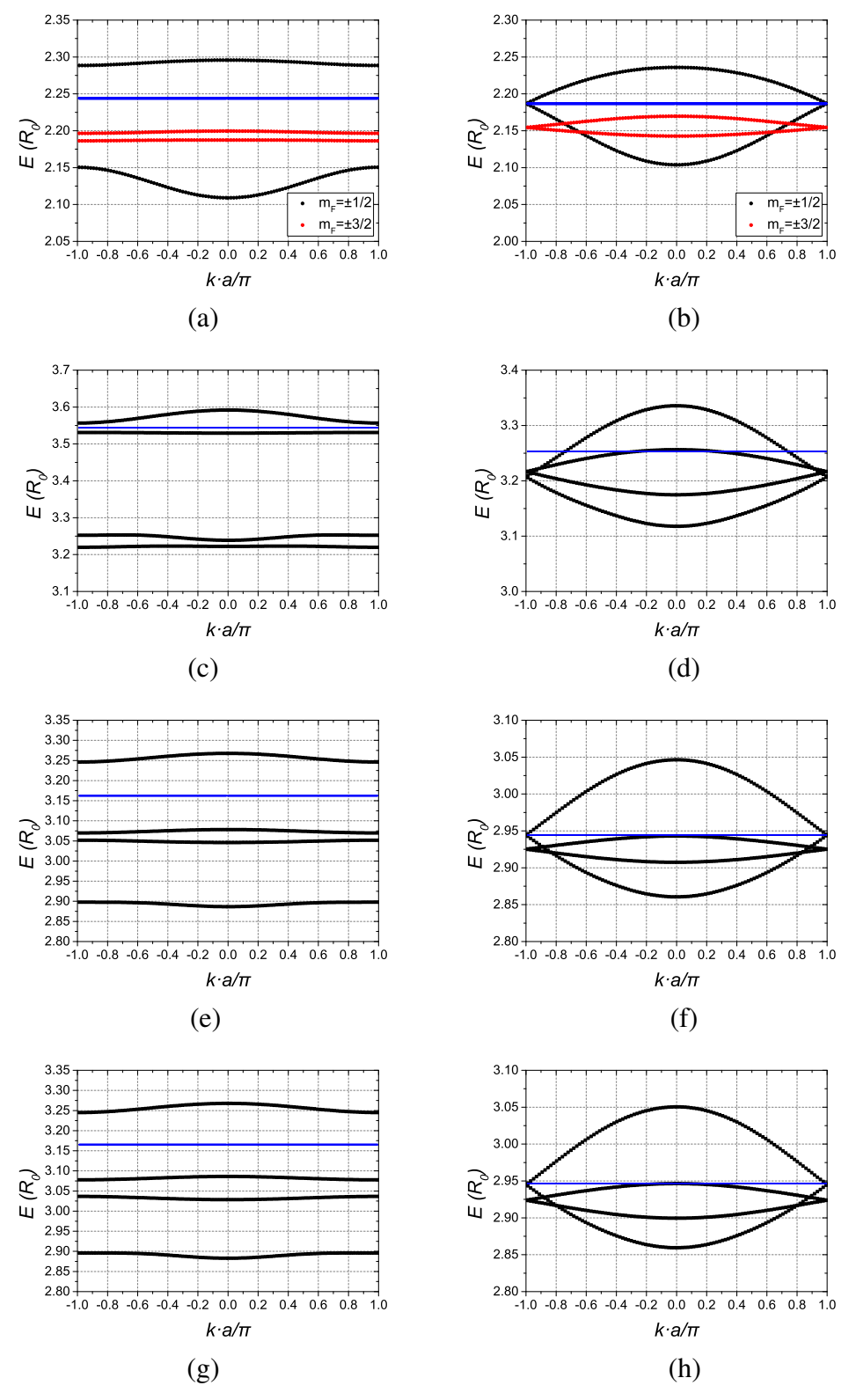


**Figure 3.6:** The band structure of the highest 4 energy states under different arrangements when  $d_1 + d_2$  is fixed: (a) the spherical case when  $d_1 = 4a_0$  and  $d_2 = 6a_0$ , (b) the spherical case when  $d_1 = d_2 = 5a_0$ , (c) the cubic case when  $d_1 = 2a_0$  and  $d_2 = 4a_0$  in the [001] direction, (d) the cubic case when  $d_1 = d_2 = 3a_0$  in the [001] direction, (e) the cubic case when  $d_1 = 2.5a_0$  and  $d_2 = 5a_0$  in the [110] direction, (g) the cubic case when  $d_1 = d_2 = 3.75a_0$  in the [111] direction, (h) the cubic case when  $d_1 = d_2 = 3.75a_0$  in the [111] direction, (h) the cubic case when  $d_1 = d_2 = 3.75a_0$  in the [111] direction. The blue line is the Fermi energy. For the spherical model calculations, the states with  $m_F = \pm 3/2$  ( $m_F = \pm 1/2$ ) is in red (black).

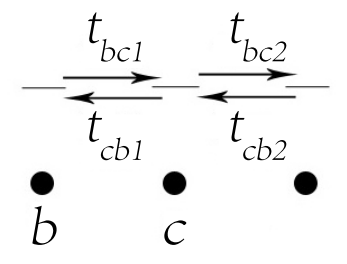


**Figure 3.7:** Schematic showing the definition of the transition strengths  $t_{bc1}$ ,  $t_{cb1}$ ,  $t_{bc2}$ , and  $t_{cb2}$ ; here atoms b and c are in the same unit cell.

the Brillouin zone doubles. The calculation could not be done under the condition  $d_1 + d_2 = 6a_0$  for the cubic model in the [110] and [111] directions, because the relevant overlap matrix is not positive definite; we use the condition  $d_1 + d_2 = 7.5a_0$  instead.

We now investigate the topological properties of the band structure and their connection to the properties of the finite chains. We calculate the Zak phase Z as described in §3.1.3; the results are shown in Table 3.2. All the short-long arrangement calculations are done under the same conditions as the band structures described above, while the long-short arrangement calculations are done by exchanging the values of  $d_1$  and  $d_2$ . For the cubic case, 'first' means that the states correspond to the first curve at the top of the pictures in Figure 3.6, 'second' means that the states correspond to the second curve from the top of the pictures in Figure 3.6. The results confirm that the states observed to split from the bands in the finite-chain calculations are indeed non-trivial topological states. In general we expect these topological states to arise when the effective chain (after allowing for the split-off of any electrostatically bound states) is terminated by a weak bond; Table 3.2 indeed shows non-trivial Zak phases ( $Z = \pi \mod 2\pi$ ) for short-long chains; however, compared with the other cases and SSH model results, the Zak phase for the spherical case with  $m_F = \pm \frac{3}{2}$  is 'abnormal' (it has non-trivial edge states for long-short-chains).

Now we show that the existence of 'abnormal' values of Zak phase result from the behavior of the effective transition strength between the same single-acceptor level on different nearest-neighbour sites as a function of separation.

First, we develop a simple orthogonal 1-level-per-acceptor model in which the

only parameters are the transition strengths between different sites, the most important being between nearest neighbours. These are shown in Figure 3.7: we define  $t_{bc1}$ ,  $t_{cb1}$  to be the intra-cell transition strengths, and  $t_{bc2}$ ,  $t_{cb2}$  to be the inter-cell transition strengths. Normally, a longer bond length would correspond to a smaller value of the transition strength and a shorter bond to a larger transition energy. But in the 'abnormal' case, we find that the dependence is reversed by checking the Hamiltonian elements, so the longer bond length has a stronger transition strength for the particular level concerned. This makes the effective arrangement for the system (defined in terms of strong and weak interactions) differ from the geometrical arrangement; hence the system can switch from a 'short-long' arrangement to a 'long-short' arrangement and *vice versa*. In other words, whether the chain is abnormal or not depends on whether or not its effective arrangement is the same as its geometrical arrangement.

In the real acceptor chain the states on different sites are in general not orthogonal so we must solve a generalized eigenvalue problem. This leads us to define an effective transition matrix

$$T_{\text{eff}}(k) = S^{-\frac{1}{2}}(k)T(k)S^{-\frac{1}{2}}(k).$$
 (3.12)

Under this definition, the eigenvector becomes

$$|\tilde{u}_k\rangle = S^{\frac{1}{2}}(k)|u_k\rangle \tag{3.13}$$

and the Zak phase can be written as

$$Z = i \int_{\text{first BZ}} dk \langle \tilde{u}_k | \partial_k \tilde{u}_k \rangle \tag{3.14}$$

As shown in a previous paper [44], the Zak phase remains invariant under the transformation (3.13). Therefore we can say the effective transition strength matrices are equivalent to the original transition matrices in the computation of the Zak phase.

We find that the effective transition strengths can behave differently from the

original ones and in particular their dependences on the geometrical arrangement can be opposite. Therefore, once again we need to use an effective arrangement to describe the system, which we define so that the short effective bonds correspond to the strong effective transition strengths, and the long effective bonds to the weak effective transition strengths. With these two new definitions, we find the Zak phase for a particular band is determined by the the effective atomic arrangement; once again, the Zak phase is abnormal when this effective arrangement differs from the actual geometry. An alternative way of phrasing this argument is in terms of the Wannier functions for each band, whose centres of charge are closely related to the Zak phase [43] and which are by construction decoupled from the other bands [50].

### 3.3 Summary

In this chapter, we achieved a LCAO model for one dimensional system within the independent-hole approximation. We studied the energy states in the finite chain arising from linear combinations of the  $1\Gamma_8^+$  acceptor ground states and found a complex interplay between the long-range Coulomb interaction and the topological properties of the chain. The electrostatic attraction between the hole and the acceptors in the interior of the chain 'splits off' a state localised on the end acceptor, and the transition between topological and non-topological states then takes place on the acceptor next to those acceptors. The topological origin of the state localised on the acceptors next to the end of the chain can be confirmed by computing the Zak phase in the corresponding infinite system. The non-trivial states found there will always localize at some particular place and cannot be removed by changing the potential.

### **Chapter 4**

### **Multi-hole Models In**

## **One-dimensional Systems**

In this chapter we will investigate the acceptors in one-dimensional system under three multi-hole models: the full configuration interaction (full CI calculation), the Heitler-London approximation (HL approximation), and the unrestricted Hartree-Fock method (UHF method). We will always take one hole per acceptor, so it is charge neutral. And only the nearest transitions will be considered here, which is proved to be a valid approximation as discussed in §4.1.5. We will compare the results from three methods and investigate the relation between them. The linear acceptor chain will be studied including both the finite chain and the chain with a periodic boundary condition. The energy states for the finite system and the band structure of the infinite system will be calculated. We will also investigate the topological property of the edge states and the symmetry of the system.

### 4.1 Multi-hole models

According to the previous works, low temperature behaviors of matter (such as magnetism [51], low-dimensional electron transport [52], topological phases [53]) can arise due to strongly interacting particles within crystals [54]. Some interesting quantum phases (such as antiferromagnetism [55], superconductivity [56]) also can be achieved in the low-temperature strongly interacting cases [57]. So the calculations of an acceptor array including hole-hole interactions may bring us some inter-

esting states. In §3.1, we developed a one-hole model to describe a pair of acceptors and a linear acceptor chain. Here, we use the same approach to describe the one-hole part of the Hamiltonian, including cubic anisotropy, but only considering the nearest transitions for the chain (see §4.1.5). We then combine this one-hole Hamiltonian with two-hole terms representing the inter-hole Coulomb repulsion, using methods described in Reference [47]. Our units of energy and length are the effective Rydberg  $R_0 = \frac{e^4 m_0}{2\hbar^2 \varepsilon_0^2 \gamma_1}$  and the effective Bohr radius  $a_0 = \frac{\hbar^2 \varepsilon_0^2 \gamma_1}{e^4 m_0}$ , respectively[6]. We use parameters appropriate for silicon throughout; however, our methods are easily transferable to other cubic semiconductors. With these silicon parameters,  $R_0 = 24.8 \,\mathrm{meV}$  and  $a_0 = 2.55 \,\mathrm{nm}$ . In all cases we report our results for lines oriented along the three highest-symmetry directions of the cubic host: [001], [110] and [111].

# 4.1.1 Full configuration interaction calculation (full CI calculation) and Heitler-London approximation (HL approximation)

The configuration interaction calculation (full CI) retains a basis of Slater determinants corresponding to all possible configurations of the holes distributed across basis states on all acceptors, and the Hamiltonian is

$$H_{CI} = \sum_{i}^{N} (H_i \cdot \prod_{j \neq i}^{N} S_j) - \sum_{i < j}^{N} (\frac{2}{r_{ij}} \cdot \prod_{l \neq i, j}^{N} S_l), \tag{4.1}$$

where  $H_i$  is the Hamiltonian matrix element for the one-hole model,  $S_i$  is the overlap matrix element for the one-hole model,  $\frac{2}{r_{ij}}$  is the hole-hole interaction in effective Rydberg units, N is the number of holes, and i, j, k labels the holes. The interaction appears with a minus sign because the Hamiltonian is expressed for electron states. Therefore, throughout this chapter, the most favourable states for occupation by holes are those with the *highest* energy—we refer to the highest-energy state as the

'ground state'. The overlap matrix is also needed and can be written as

$$S_{CI} = \prod_{i}^{N} S_i, \tag{4.2}$$

where  $S_i$  is the overlap matrix element for the one-hole model, and N is the number of holes.

The full CI calculation is exact for a given choice of single-particle basis, but scales very badly (super-exponentially) with the size of the system. Also, the total energy expression is not extensive so it cannot be implemented under periodic boundary conditions. The first problem is ameliorated by restricting the set of configurations to those with exactly one hole per acceptor when the system is on the instulating side of the Mott transition [14, 15]; we call this the Heitler-London (HL) approximation because it is in the same spirit as the Heitler-London treatment of the H<sub>2</sub> molecule, and has been used for acceptors pairs in Reference [9]. The many-particle basis set now grows more slowly (although still exponentially), but the difficulty in treating the infinite system still remains.

### 4.1.2 Unrestricted Hartree-Fock method

To handle the infinite system we employ an unrestricted Hartree-Fock (UHF) method, where the many-hole wave-function is optimised over single Slater determinants constructed from a set of one-hole functions, without any restriction on the spin components of each function. The optimisation of the one-hole functions results in a self-consistent-field (SCF) approach, where each hole can be understood to experience the average interaction of the others. The one-hole functions are eigenfunctions of the Fock matrix  $\hat{F}$ , which is given by

$$\hat{F} = \hat{H}^{\text{core}} + \hat{G},\tag{4.3}$$

where  $\hat{H}^{\text{core}}$  is the Hamiltonian for the one-hole model (including spin-orbit coupling), and  $\hat{G}$  is a matrix reflecting the self-consistent influence from other holes. If we expand all quantities in terms of a set of single-hole basis functions  $|\phi_{\mu}\rangle$ , G is

given by

$$G_{\mu\nu} = \sum_{\lambda\sigma} P^{\lambda\sigma} \left( (\mu\nu \|\sigma\lambda) - (\mu\lambda \|\sigma\nu) \right), \tag{4.4}$$

where  $\mu, \nu, \sigma, \lambda$  are labels running over all basis functions on all acceptors. Although labels run over all basis functions on all acceptors generally, only a part of the combinations of acceptors ( $\mu\nu$  and  $\lambda\sigma$  are on the same acceptor or on the nearest neighbours) will be considered in our calculations in this chapter and later as discussed in §4.1.5.

$$(\mu \nu \| \sigma \lambda) = \int d\mathbf{x}_1 d\mathbf{x}_2 \, \phi_{\mu}^*(\mathbf{x}_1) \phi_{\sigma}^*(\mathbf{x}_2) \frac{-2}{|\mathbf{r}_1 - \mathbf{r}_2|} \phi_{\nu}(\mathbf{x}_1) \phi_{\lambda}(\mathbf{x}_2)$$
(4.5)

(where  $\mathbf{x} = (\mathbf{r}, \tau)$  is a composite coordinate for position  $\mathbf{r}$  and intrinsic angular momentum  $\tau$ , and  $(\mu \nu \| \sigma \lambda)$  is the notation used in Reference [58]) are matrix elements of the Coulomb interaction, and P is the one-hole density matrix which can be constructed as

$$P^{\mu\nu} = \sum_{i}^{N} C_{i}^{\mu} C_{i}^{*\nu}, \tag{4.6}$$

where  $C_i$  is an eigenvector of the generalised eigenproblem

$$F \cdot C_i = \varepsilon_i S \cdot C_i, \tag{4.7}$$

N is the number of holes (hence the number of occupied eigenvectors), and i goes through all eigenvector labels. Once again, because our calculation is describing holes, the single particle states are occupied according to the *aufbau* principle from the highest eigenvalue downwards. The total energy can then be written as

$$E_{\text{tot}} = \frac{1}{2} \sum_{\mu\nu} P^{\nu\mu} \left( H_{\mu\nu}^{\text{core}} + F_{\mu\nu} \right), \tag{4.8}$$

The self-consistent calculation continues until the output density matrix (4.6) is similar to the input one used in (4.4). Further details can be found in Reference [58]; however, in contrast to the conventional case, our system contains spin-orbit coupling and therefore we cannot separate the single-particle functions into separate

sets corresponding to each spin component. So it is necessary to include exchange interactions between *all* pairs of single-hole states, not just those of the same spin.

Here we should point out that the UHF method is less useful for the calculation of excited states. On one hand, the calculation of excited states requires optimising over single Slater determinants for both the ground state and the excited state at the same time, which is hard to be done. On the other hand, the single Slater determinants does not describe the excited state properly. So it is better to use the HL approximation to simplify the calculation of low-lying excitations.

### 4.1.3 Periodic boundary conditions

Although less accurate than the CI method, the UHF method does not have the limitations mentioned in §4.1.1. It scales polynomially, rather than exponentially, as the system size increases, and the total energy expression (4.8) is extensive. So it is possible to apply it to a linear chain with periodic boundary conditions [59]. In this case, the Fock matrix  $\hat{F}_k$  at a particular Bloch wavevector k will be

$$\hat{F}_k = \sum_X e^{ikX} \hat{F}_X = \sum_X e^{ikX} (\hat{H}_X^{\text{core}} + \hat{G}_X) = \hat{H}_k^{\text{core}} + \hat{G}_k, \tag{4.9}$$

where X labels lattice displacements of a single unit cell,  $\hat{F}_X$ ,  $\hat{H}_X^{\text{core}}$  and  $\hat{G}_X$  are the elements of F, H and G connecting different cells separated by X, and  $\hat{H}_k^{\text{core}}$  and  $\hat{G}_k$  are the matrices of  $\hat{H}^{\text{core}}$  and  $\hat{G}$  in momentum space. The Fock matrix  $\hat{F}_k$  can be diagonalised to find a set of eigenvectors  $C_{ki}$ , and the corresponding contribution  $P_k$  to the the one-particle density matrix is

$$P_k^{\mu\nu} = \sum_{i}^{N} C_{ki}^{\mu} C_{ki}^{*\nu}.$$
 (4.10)

The real-space form of  $P^{\mu\nu}$  can then be recovered by inverse Fourier transformation, and re-inserted into the SCF procedure as previously.

### 4.1.4 Zak phase calculation for the multi-hole model

For the unrestricted Hartree-Fock calculation of a linear chain with the periodical boundary condition, the multi-hole state is not able to be achieved directly from the Fock matrix. Instead, it require a complex determinant to calculate it from the one-hole state. So we could no longer get Zak phase easily by using the method in §3.1.3. Instead, this quantity can be obtained from the one-hole density matrix, which is available during the SCF procedure of the UHF calculation. We follow a recent paper[53], in calculating the Zak phase for in a general situation is using the formula

$$Z = \arg \left[ \operatorname{tr} \left( \prod_{k} S_{k} P_{k} \right) \right], \tag{4.11}$$

where  $S_k$  is the overlap matrix transformed into Fourier space,  $P_k$  is the single-particle density matrix as defined above, and k is the wavevector going through the first Brillouin zone. However, we have to remember that Coulomb interactions can change the topological classification [60, 46] so we cannot necessarily expect the Zak phase to predict correctly the presence or absence of topological edge states; indeed, we show evidence in §4.2.5 that the Zak phases do not correspond to the topological property of the edge states in the interacting system.

### 4.1.5 Spatial cut-offs

In practice, the sums in equations (4.4) and (4.9), as well as the corresponding sums over acceptor cores in  $\hat{H}^{core}$  have to be truncated. For the results in the multi-hole model we have performed this truncation after nearest neighbours; for exchange and hopping terms which involve transferring a single hole from site to site, this is justified by the relatively well localised acceptor wave-functions (this means that the relevant matrix elements will decay exponentially with hopping distance). The Coulomb terms (both the hole-hole interaction and the hole-core interaction) decay much more slowly, like  $\frac{1}{R}$  (where R is the separation between the charges), but will cancel one another out provided the system is approximately charge neutral at all points (fortunately, it is true in our calculations). We have checked that the key findings of this chapter listed below are reproduced in an extended model which includes all the next-nearest-neighbour hoping but only the largest next-nearest-neighbour hole-hole interactions, for both the finite length chain and periodic boundary case. These key findings include:

**Table 4.1:** The eigenenergy of the 4-fold-degenerated ground state ( $\Gamma_8^+$ ) obtained from the Gaussian expansion with 21 Gaussian parameters and 5 Gaussian parameters for Si and the difference between them; the energy unit is the effective Rydberg  $R_0$ , and the difference is shown in the percentage of the original 21-parameter result.

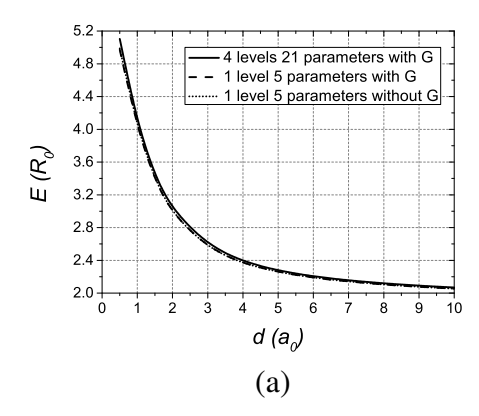
21-parameter result	5-parameter result	difference
$1.868314R_0$	$1.854034R_0$	0.7644%

- anti-crossings between the ground state and the nearest excited state in the [001] direction of the finite chain in the full CI calculation in §4.2.2;
- 4-fold-degenerate state at the long-short end in the finite chain full CI calculation in §4.2.2;
- anti-crossings between filled states and empty states in the [001] direction of the finite chain in the UHF method in §4.2.2;
- the large gap between filled states and empty states in both the finite chain and the infinite chain in the UHF method in §4.2.2 and §4.2.4;
- the Zak phase value achieved in UHF method in the infinite chain in §4.2.4.

Since introducing the next nearest hole-hole interactions will more than double the time of the calculations, it is a wise choice to only consider the nearest neighbours.

### 4.1.6 Single-particle basis

It remains to specify the basis for the single-particle states on each acceptor for the multi-hole calculations. As in the previous one-hole calculations, we decompose the spatial parts of the acceptor states into linear combinations of Gaussian orbitals. However, as we are interested in the behavior of the low-lying states of the linear chain, we make several changes. First, we consider only the 4-fold-degenerate ground state manifold  $(1\Gamma_8^+)$  of an isolated acceptor, we expand the radial parts in terms of Gaussian functions as shown in Equation 2.6. Second, because we only need to describe the ground state, we use only five Gaussian functions, with exponents  $\alpha_i = \{100.0, 25.0, 6.25, 1.5625, 0.390625\}$ , rather than 21 as in the one-hole calculation; the single-acceptor ground-state energies in silicon computed with 5 and 21 Gaussians are compared in Table 4.1 and found to differ by less than 1%.



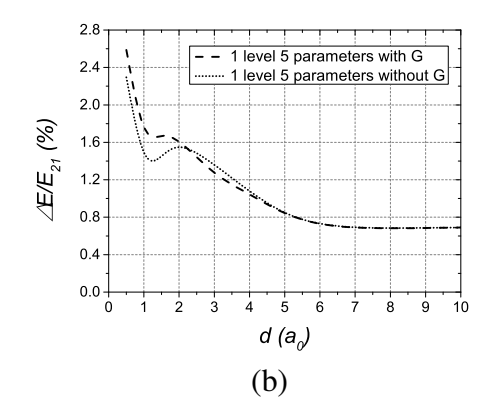


**Figure 4.1:** The behavior of the doubly-degenerate ground state energies with different approximations in the [001] direction for a pair of acceptors in Si under the one-hole model: (a) the ground state eigen energies, (b) the differences between the ground state eigen energies with different approximations. The solid line is the result of one-hole model with 21 Gaussians, the dash lines are for the ground state ( $1\Gamma_8^+$ ) with 5 Gaussian parameters but including *G*-orbitals, the dotted lines are for the ground state ( $1\Gamma_8^+$ ) with 5 Gaussian parameters excluding *G*-orbitals. In (b), energy differences with respect to energy  $E_{21}$  (the solid line in (a)) are shown as percentages of the energy  $E_{21}$  (the solid line in (a)).

The reduction in the number of Gaussians saves time in the evaluation of matrix elements for the subsequent calculations. Now it approximately takes 0.4% of the time required by the 21-Gaussian basis.

Finally, we remove the admixture of G-orbital Gaussian components (l=4) in the ground-state manifold, to limit the size of the matrices involved in the calculation, and re-normalize the remaining parts of the wavefunction. As an example, we compare the energy of the doubly-degenerate ground state for a single hole bound to a pair of acceptors in the [001] direction with and without the G-orbitals in Figure 4.1. It can be seen that omitting the G-orbitals leads to errors in the energy of 1–2%. We also compare the ground state wave functions for both a single acceptor and a pair of acceptors. The probability densities are shown in Figure 4.2. Here as we take the total probability of 4 degenerate states in the single acceptor case, the results will obey the cubic symmetry. So the probabilities along x-axis and y-axis are same as the one along z-axis. It can be seen from Figure 4.2 (a) that two systems will behave similarly but the the 5-Gaussian case is less localized in the small range near to the acceptor core. And we can also learn the same thing by comparing (b)

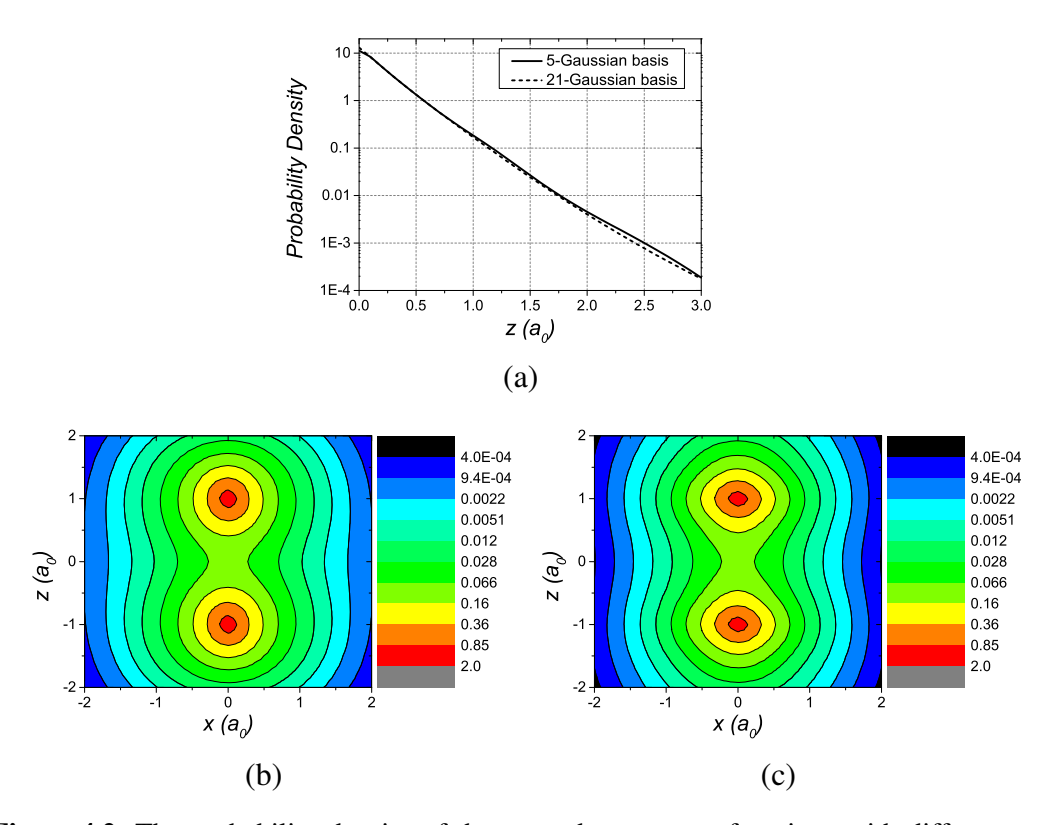


**Figure 4.2:** The probability density of the ground state wave functions with different approximations for a single acceptor and a pair of acceptors in the [001] direction in Si under the one-hole model: (a) the total probability density of the single acceptor case along z-axis, (b) a pair of acceptors case when  $d = 2a_0$  for 5-Gaussian basis in x-z plane, (c) a pair of acceptors case when  $d = 2a_0$  for 21-Gaussian basis in x-z plane. In (a), the solid line is the result of one-hole model with 5 Gaussians, the dash lines are for the ground state with 21 Gaussian parameters excluding *G*-orbitals.

and (c).

For convenience in the discussion of results in §4.2.2.1 and §4.2.2.2, we assign labels to the states of the 4-fold-degenerate ground  $\Gamma_8^+$  manifold so that we can distinguish them. The main contribution is from the  $S_{\frac{3}{2}}$  state with total angular momentum  $F = \frac{3}{2}$ ; we therefore use the values of the angular momentum projections  $m_F = \{\frac{3}{2}, \frac{1}{2}, -\frac{1}{2}, -\frac{3}{2}\}$  to label the different rows of the irreducible representation. (The total angular momentum  $\vec{F} = \vec{L} + \vec{I} + \vec{S}$ , where  $\vec{I}$  is the intrinsic orbital angular momentum of the p states in the valence band.)

### 4.2 Multi-hole model results

### 4.2.1 A pair of acceptors

For a pair of acceptors, all the methods and approximation mentioned in §4.1 can be applied. To show the long-range behavior clearly, we calculate the interaction energy

$$E_{\text{int}} = E_T - 2E_{\text{single}} = E_{\text{tot}} - \frac{2}{R} - 2E_{\text{single}}, \tag{4.12}$$

where  $E_{\text{single}}$  is the single-acceptor energy,  $E_T$  is the total energy including the corecore interaction,  $E_{\text{tot}}$  is the total energy for the holes only (directly obtained from the Hamiltonian (4.1)), and  $\frac{2}{R}$  is the core-core interaction term (appearing with a minus sign to be consistent with our convention for the hole energy). We did not consider the core-core interaction term in the one-hole model; we refer to  $E_{tot}$  as the 'total energy' for the rest of this thesis. The interaction energies  $E_{int}$  of the ground state from three different models in three high-symmetry directions are shown in the left column of Figure 4.3; they appear as the negatives of standard molecular bindingenergy curves. We also show the difference in the total energy  $E_{\text{tot}}$  between the full CI calculation and the other approaches (as a percentage of the full CI result) in the right column. Both the HL approximation and the UHF method are good approximations to full CI for all directions, but the differences are greatest at small separations; the HL approach generally provides a better energy than UHF (since they involve variational approximations to the true wave-function, both methods give a lower bound on the true ground-state energy in the hole system). For the [001] direction, the differences reach a maximum around  $1.5a_0$  and can be ignored when the separation  $d \ge 4a_0$ ; for the [110] and [111] directions, they peak around  $1.5a_0$  and could be ignored for  $d \ge 5a_0$ . By comparing the eigenvectors of the full CI results and the UHF results, we also find the arrangement of the holes in the UHF calculation is corresponding to one of the largest components of the ground state in the full CI case.

For the convenience of further discussion in §4.2.2.1 and §4.2.2.2, Figure 4.4 shows the Fock matrix eigenvalues for pairs oriented along different directions. The

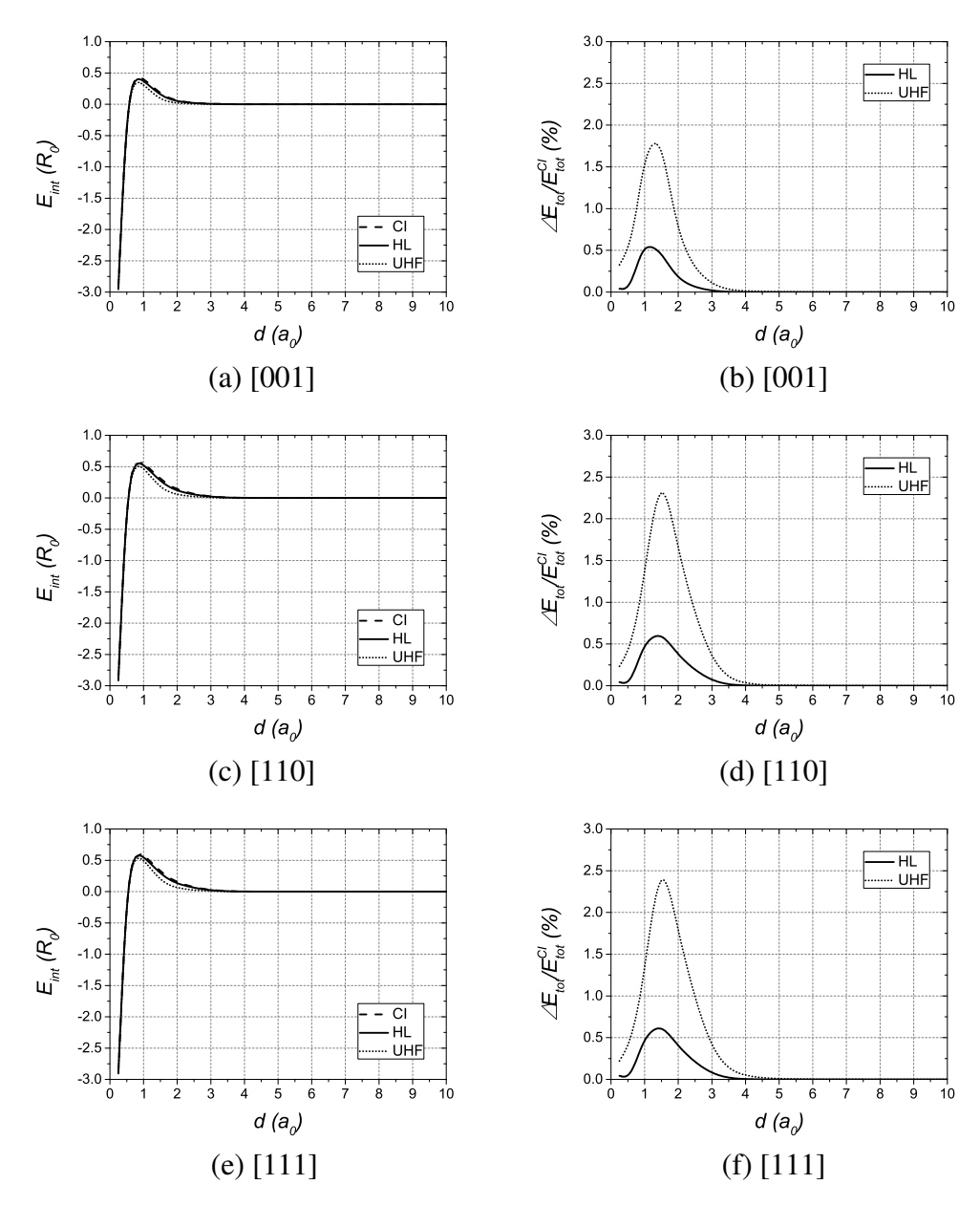


**Figure 4.3:** The interaction energy  $E_{\text{int}}$  of the ground state and the difference of the total energy  $E_{\text{tot}}$  towards the full CI calculation in three typical directions for a pair of acceptors: (a) the interaction energy  $E_{\text{int}}$  in the [001] direction, (b) the difference of the total energy  $E_{\text{tot}}$  in the [001] direction, (c) the interaction energy  $E_{\text{int}}$  in the [110] direction, (d) the difference of the total energy  $E_{\text{tot}}$  in the [110] direction, (e) the interaction energy  $E_{\text{int}}$  in the [111] direction, (f) the difference of the total energy  $E_{\text{tot}}$  in the [111] direction. For (a), (c), (e), the dashed line is for the full CI calculation, the solid line is for the HL approximation, the dotted line is for the UHF method, all the differences are in the percentage of the full CI result.

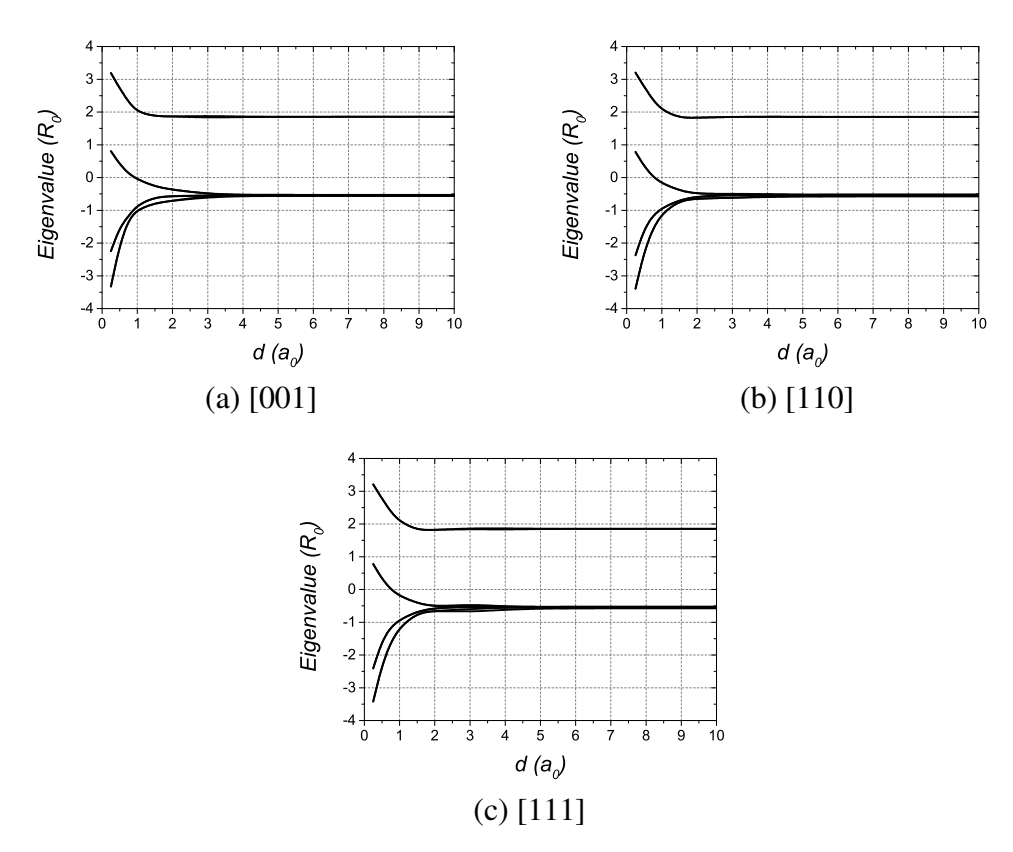


**Figure 4.4:** The behavior of the Fock matrix eigenvalues in different directions for a pair of acceptors: (a) the [001] direction, (b) the [110] direction, (c) the [111] direction.

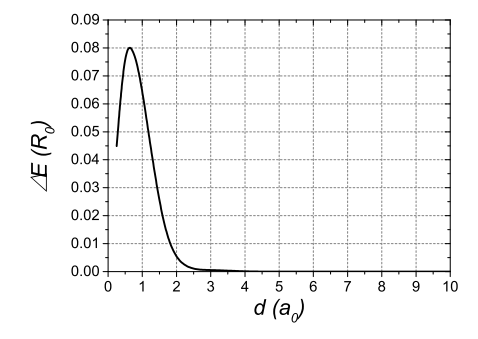


**Figure 4.5:** The difference between the ground state and the first excited state in the [001] direction for the full CI calculation.

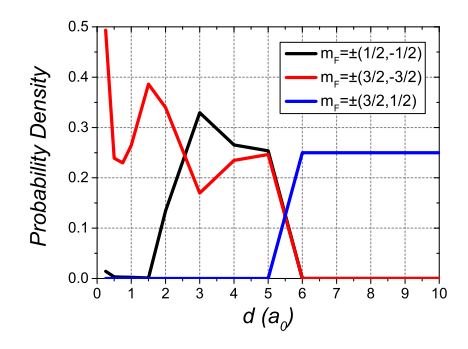
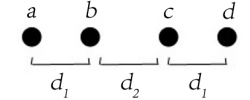
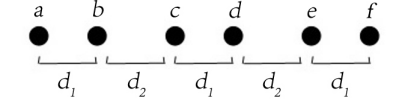


**Figure 4.6:** The probability density for three different components in the ground state in the [001] direction for the full CI calculation. The black line is corresponding to  $m_F = \pm (\frac{1}{2}, -\frac{1}{2})$  component, the red line is corresponding to  $m_F = \pm (\frac{3}{2}, -\frac{3}{2})$  component, the blue line is corresponding to  $m_F = \pm (\frac{3}{2}, \frac{1}{2})$  component.

ground state appears at the top of the pictures as this is a calculation for acceptors. Each line represents a pair of doubly-degenerate states within the error tolerance; since there are two holes, only the doubly-degenerate ground state at the top of the diagram will be filled. There is a large gap between the filled and empty states at all separations; this is generated by the strong hole-hole repulsion within the selfconsistent field. We will see that this feature persists in the calculations on larger systems. By investigating the eigenvector of the UHF results, we can find that the Mott transition for different directions happens at different separations. It happens between  $1a_0$  and  $1.5a_0$  for [001] and [111] direction, but happens between  $2a_0$ and  $3a_0$  for [110] direction. Here we distinguish the Mott transition by checking the first symmetry-breaking point where the broken symmetry implies that holes can be localised on particular acceptors (equivalent to the insulator side of the Mott transition). We checked the diagonal matrix elements of the density matrices. When the elements corresponding to the same spin on different acceptors not equivalent to each other, the inversion symmetry is breaking. Compared with the result from experiments  $(2.45a_0)$  [16], it can be seen that the Mott transition happens for smaller separations in some directions in 1D. The reason could be that the experimental result  $2.45a_0$  is based on a randomly doping in a 3D system. So the value is an average separation involving all directions which are not equivalent to each other due to the symmetry of the system $(T_d)$ , and the average coordination number in the



(a) 4-acceptor linear chain



(b) 6-acceptor linear chain

**Figure 4.7:** Schematics of the linear chains studied in this chapter. a, b, c, d, e, f are the labels of acceptors;  $d_1 < d_2$  is known as the 'short-long arrangement',  $d_1 > d_2$  is known as the 'long-short arrangement'.

3D experiments is higher than the coordination number in the 1D and 2D systems. These mean that the predictions from the 1D and 2D system could move away from the experimental result. As the prediction depends on the directions involved in the calculations and the coordination number in 1D system is lowest, it is reasonable that the Mott transition for a 1D calculation happens far away from the experimental result in some directions. In  $\S 5.3.3$ , we will see that the Mott transition happens at the separation closer to the experimental result  $(2.45a_0)$  in the 2D honeycomb lattice.

In the absence of cubic anisotropy, Durst et~al.~[10] argue that the long-range interaction between two acceptors is dominated by quadrupolar effects, which they find favour a doubly degenerate state with total angular momentum  $M_F=\pm 2$  about the core axis. This corresponds to partially aligned pairs of holes, with  $m_F=\pm \left(\frac{3}{2},\frac{1}{2}\right)$  on the two acceptors. However, with the inclusion of significant cubic anisotropy appropriate for Si  $(\delta>0$  and indeed  $\delta\sim\mu$  as shown in §2.1), we find that the pair ground state in the quantized direction (the [001] direction) only crosses over to this form for very large separations  $d>5a_0$  in the full CI calculation as shown in Figure 4.6; for smaller separations in the full CI case, the multi-hole ground state is non-degenerate as shown in Figure 4.5 and dominated by anti-ferromagnetically coupled configurations such as  $m_F=\pm\left(\frac{3}{2},-\frac{3}{2}\right)$  (for  $d\leq 2a_0$ ) and  $m_F=\pm\left(\frac{1}{2},-\frac{1}{2}\right)$  for  $2a_0< d\leq 5a_0$ . The same results are found in the HL cases.

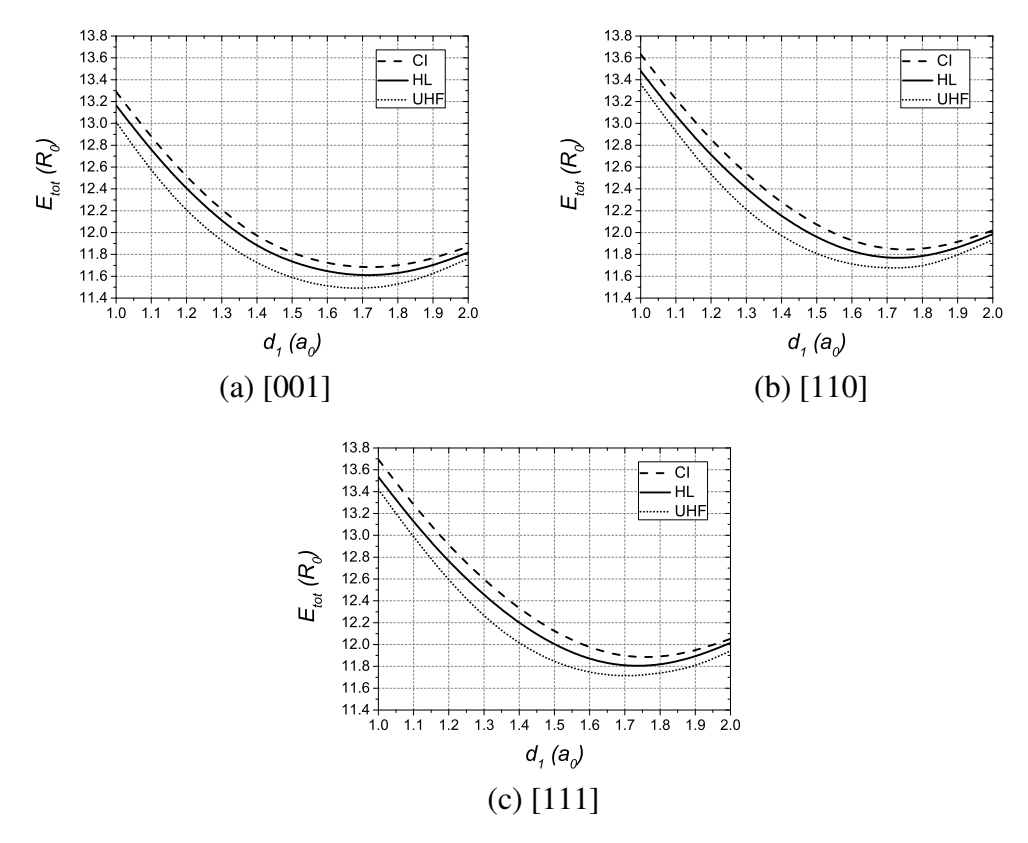


**Figure 4.8:** The behavior of the total energy of the ground state under different arrangements in three typical directions for the small-separation case  $(d_1 + d_2 = 3a_0)$  of the 4-acceptor linear chain: (a) the [001] direction, (b) the [110] direction, (c) the [111] direction. The dashed line is for the full CI calculation, the solid line is for the HL approximation, the dotted line is for the UHF method.

### 4.2.2 Finite dimerised linear chains

We next consider chains of 4 and 6 acceptors, with one hole per acceptor and with the separations  $(d_1,d_2)$  alternating to form a dimer chain as shown in Figure 4.7. When  $d_1 < d_2$ , we will refer to a 'short-long arrangement' throughout the rest of the chapter, while when  $d_1 > d_2$  we will call it a 'long-short arrangement'. We investigate two different regimes, each defined by a fixed value of  $d_1 + d_2$ : a 'small-separation' case with  $d_1 + d_2 = 3a_0$  in §4.2.2.1, and a 'large-separation' case with  $d_1 + d_2 = 6a_0$  in §4.2.2.2.

### 4.2.2.1 Small-separation case $(d_1 + d_2 = 3a_0)$

The hole-hole repulsion term now strongly influences the distribution of the holes: although the parabolic potential due to the negative acceptor cores found in the one-

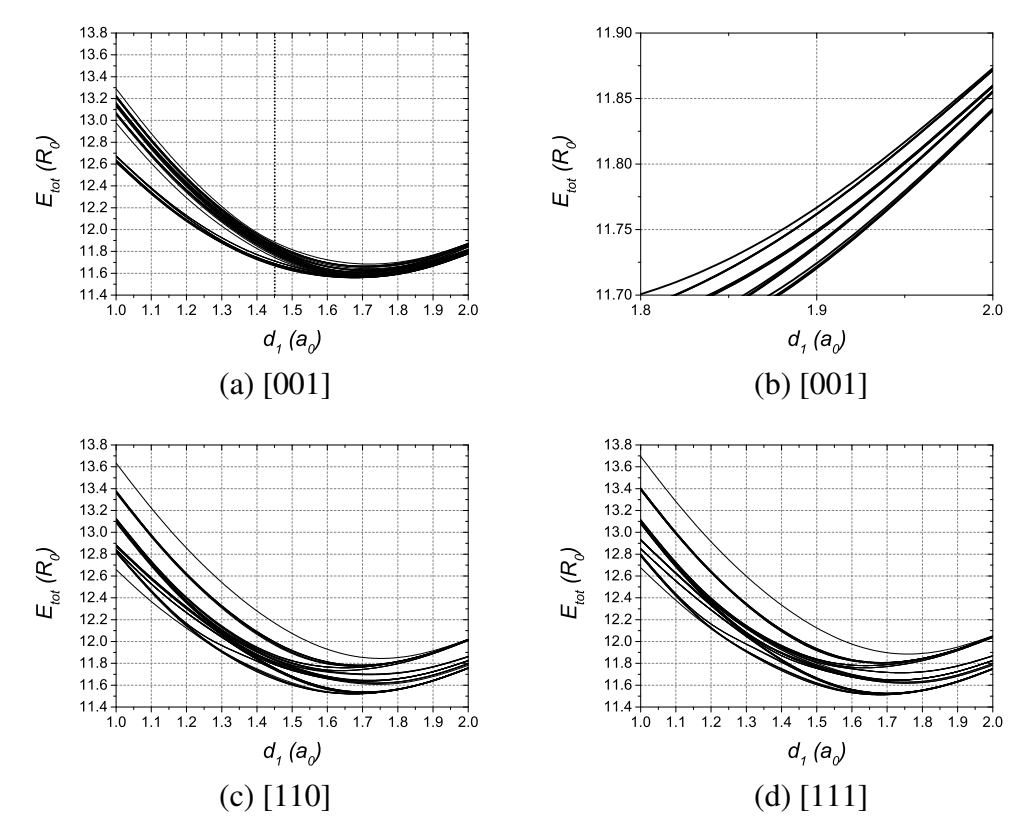


**Figure 4.9:** The behavior of the total energy of the highest 50 energy states of the full CI result under different arrangements in three typical directions for the small-separation case  $(d_1 + d_2 = 3a_0)$  of the 4-acceptor linear chain with the changing point: (a) the [001] direction, (b) details of the long-short arrangement side in the [001] direction, (c) the [110] direction, (d) the [111] direction. In Picture (a), the dotted line is for the changing point.

hole system in §3.2.2 is still present, the holes are no longer concentrated in the middle of the chain but are kept apart by their mutual Coulomb repulsion and have a nearly uniform distribution along the chain. This nearly one-hole-per-acceptor distribution implies the system is on the insulating side of the Mott transition, which suggests that the one-hole-per-acceptor distribution should play a more important role than the others in the ground state and low-lying excited states, so the HL approximation can naturally be applied and may be expected to give good results.

For chains of 4 acceptors, the ground-state total energy was obtained from all the methods mentioned in §4.1 along three high-symmetry directions, and is shown in Figure 4.8. Both the HL and UHF methods are reasonable approximations to the full CI result in all directions, with the HL approach offering a better agreement

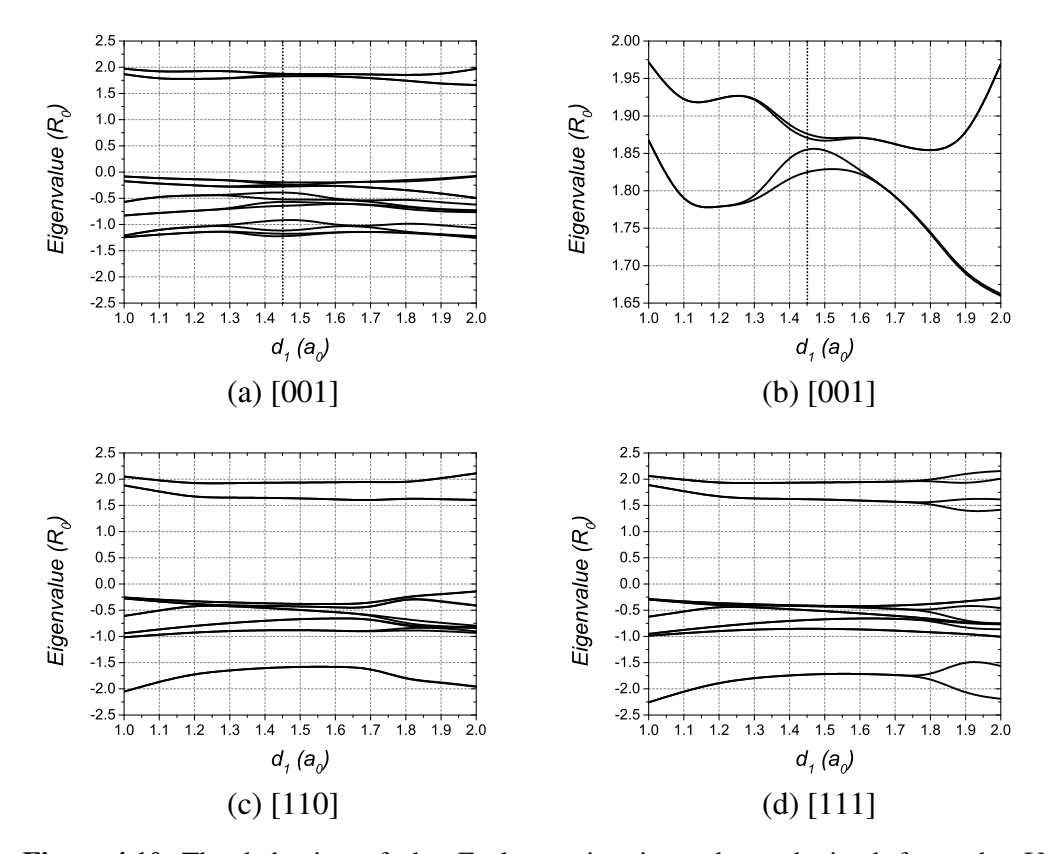


**Figure 4.10:** The behavior of the Fock matrix eigenvalues obtained from the UHF method under different arrangements in three typical directions for the small-separation case  $(d_1 + d_2 = 3a_0)$  of the 4-acceptor linear chain with the changing point: (a) the [001] direction, (b) details of the highest 4 eigenvalues in the [001] direction,(c) the [110] direction, (d) the [111] direction. For (a) and (b), the dotted lines are for the changing points.

with the full CI calculation. The difference between the full CI and the HL results reduces as the arrangement changes from short-long to long-short; the HL approximation should be more accurate when the average separation between each pair of acceptors is larger. Here the average separation is defined as  $d_{average} = \frac{L}{n-1}$ , where L is the length of the chain, n is the number of acceptors. For a 4-acceptor chain,  $d_{average} = \frac{2}{3}d_1 + \frac{1}{3}d_2$ , so the average separation grows as  $d_1$  increases. The result can then be understood by noting that the accuracy of the HL method for a pair remains roughly constant from  $d = 1a_0$  to  $d = 1.5a_0$  (see the right column of Figure 4.3) but then improves from  $d = 1.5a_0$  to  $d = 2a_0$ . The UHF approximation also becomes more accurate for the larger system, but the significant discrepancies in the energy of a pair with separations around  $1.5a_0$  (Figure 4.3) are reflected in significant er-

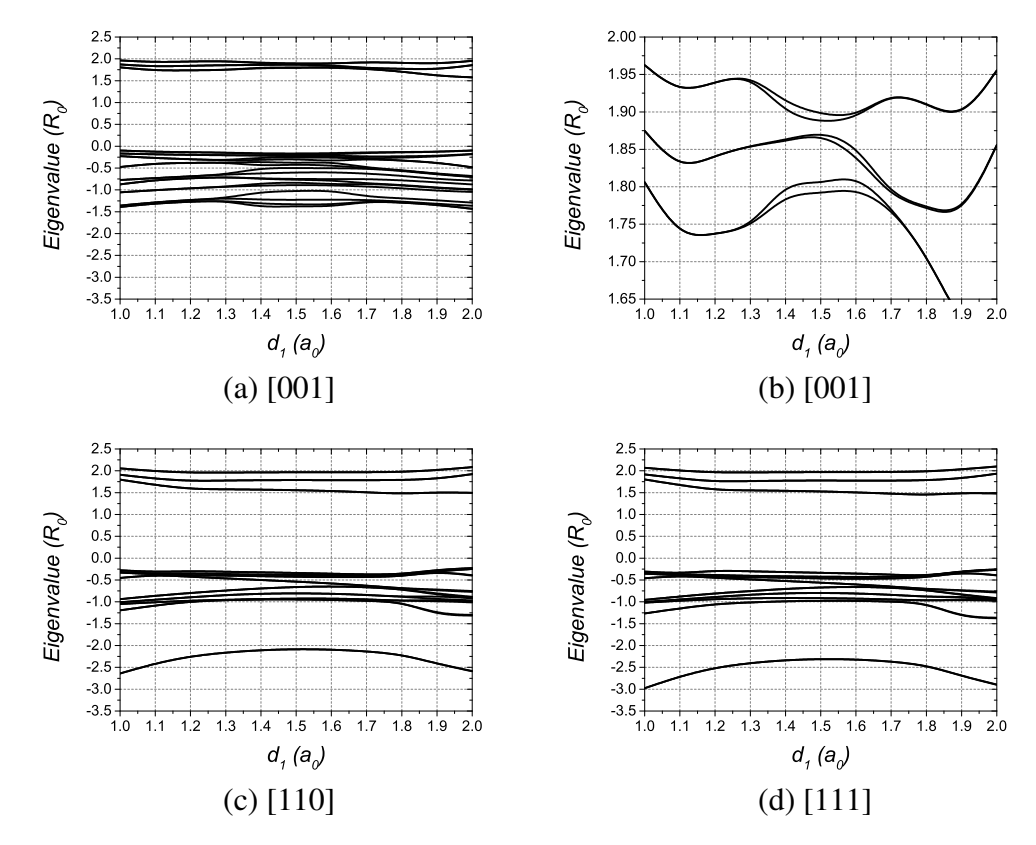


**Figure 4.11:** The behavior of the Fock matrix eigenvalues obtained from the UHF method under different arrangements in three typical directions for the 6-acceptor linear chain when  $d_1 + d_2 = 3a_0$ : (a) the [001] direction, (b) details of the highest 6 eigenvalues in the [001] direction, (c) the [110] direction, (d) the [111] direction.

rors in the middle of Figure 4.8, where  $d_1 \approx d_2 \approx 1.5a_0$ . We also computed results for chains of 6 acceptors, using the HL and UHF methods only; the behaviour of the total energies was similar.

We analyse the full CI ground-state eigenvector by looking at the dominant components (those with largest absolute values) in the basis of single-acceptor states described in §4.1. We can separate the 4 degenerate states of an isolated acceptor into two groups, those derived from  $m_F = \pm \frac{3}{2}$  and those from  $m_F = \pm \frac{1}{2}$ . We refer to the ground state as 'un-hybridized' if the dominant components contain either  $m_F = \pm \frac{3}{2}$  or  $m_F = \pm \frac{1}{2}$  single-acceptor states (but not both), while we refer to it as 'hybridized' if they contain both types of single-acceptor states.

In Figure 4.9, we show the behaviour of the 50 highest-energy (hence, most favourable) states of the full CI calculation under different arrangements of the

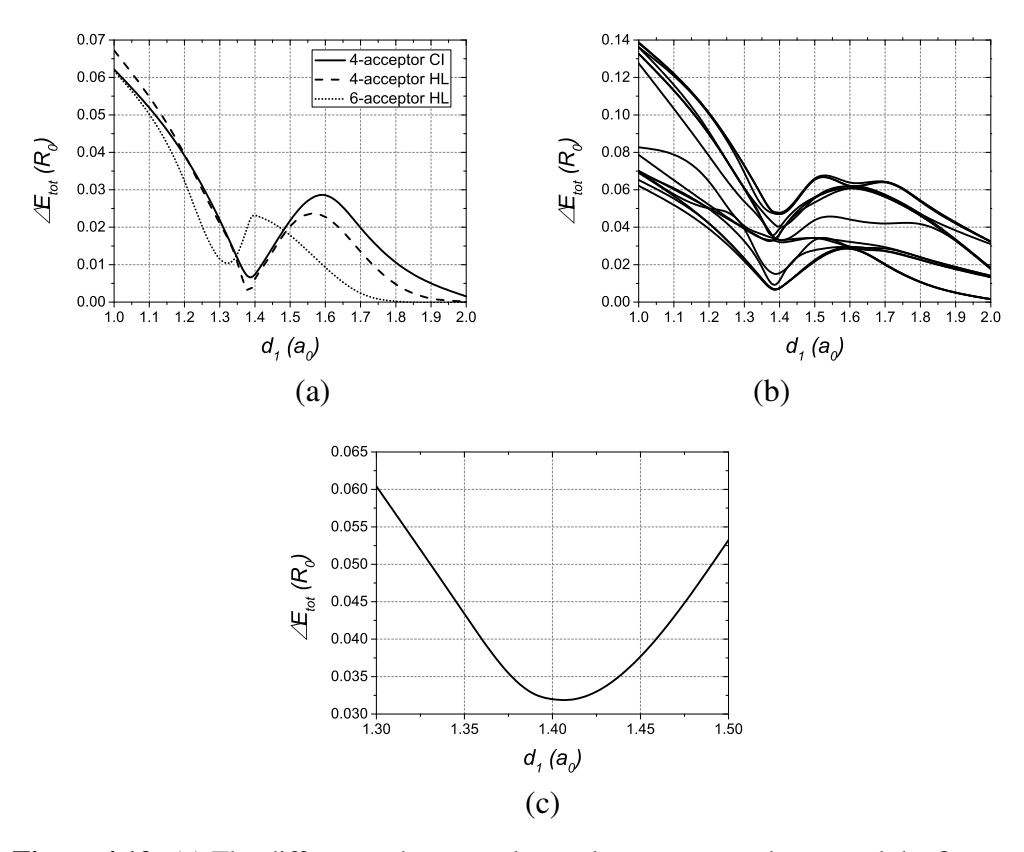


**Figure 4.12:** (a) The differences between the total energy ground state and the first excited state in different systems under different models in the [001] direction when  $d_1 + d_2 = 3a_0$ : the solid line is for the 4-acceptor full CI calculation, the dashed line is for the 4-acceptor HL calculation, the dotted line is for the 6-acceptor HL calculation, (b) The differences between the total energy ground state and the first 15 excited states for the full CI calculation in the [001] direction when  $d_1 + d_2 = 3a_0$ , (c) The differences between the old and new total energy ground state during the anti-crossing for the full CI calculation in the [001] direction when  $d_1 + d_2 = 3a_0$ .

bonds along three high-symmetry directions. For the [001] direction, the ground state is non-degenerate on the left-hand (short-long) side of the picture, while it joins three other states and forms a 4-fold-degenerate state on the right-hand side (long-short arrangement side) which is followed in energy by a 8-fold-degenerate state and another 4-fold-degenerate state as shown in Figure 4.9 (b). We observe that among the dominant components, only the states on the acceptors at the end of the chain change between these states; the dimensionality 16 of these highest manifolds comes from the 4 levels on one end multiplied by 4 levels on the other end, implying the existence of a manifold of edge states. The situation is similar for the

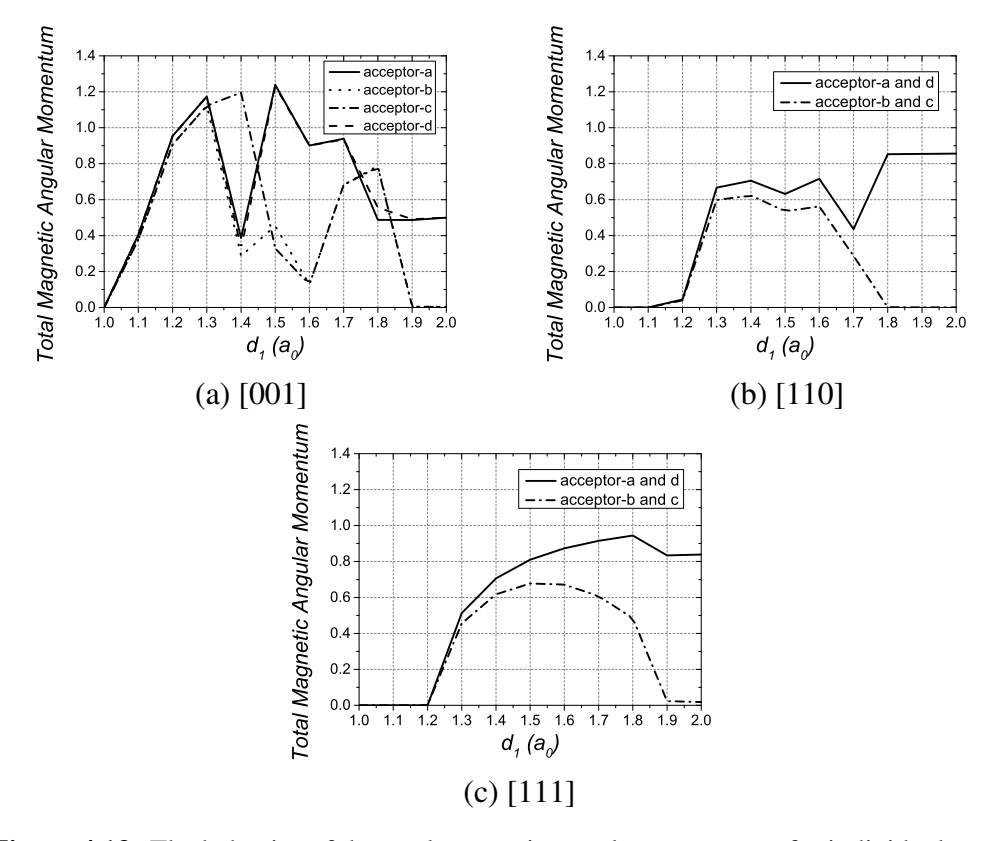


**Figure 4.13:** The behavior of the total magnetic angular momentum for individual acceptor obtained from the UHF method under different arrangements in three typical directions for the small-separation case  $(d_1 + d_2 = 3a_0)$  of the 4-acceptor linear chain: (a) the [001] direction, (b) the [110] direction, (c) the [111] direction.

other directions; we analyse the structure of this manifold in more detail in §4.2.5. It also can be seen that the ground state crosses with the nearest exited states between  $d_1 = 1.4a_0$  and  $d_1 = 1.5a_0$  in the [001] direction; the dominant components of the ground state are unhybridized to the left of the dotted line but become hybridized to the right of it. We will refer to the separation where the crossing (or anti-crossing) between the states happens as the 'crossing point', and the separation where the dominant component of the ground state changes as the 'changing point'. We see that within the resolution of the step size used  $(0.1a_0)$ , the crossing point and the changing point are the same in the [001] direction.

For the UHF calculations we can understand the overall state most clearly in terms of the behaviour of the Fock matrix eigenvalues, shown for different directions in Figure 4.10 (4-acceptor chain) and Figure 4.11 (6-acceptor chain). Here the states are usually doubly degenerate (corresponding to Kramers degeneracy un-

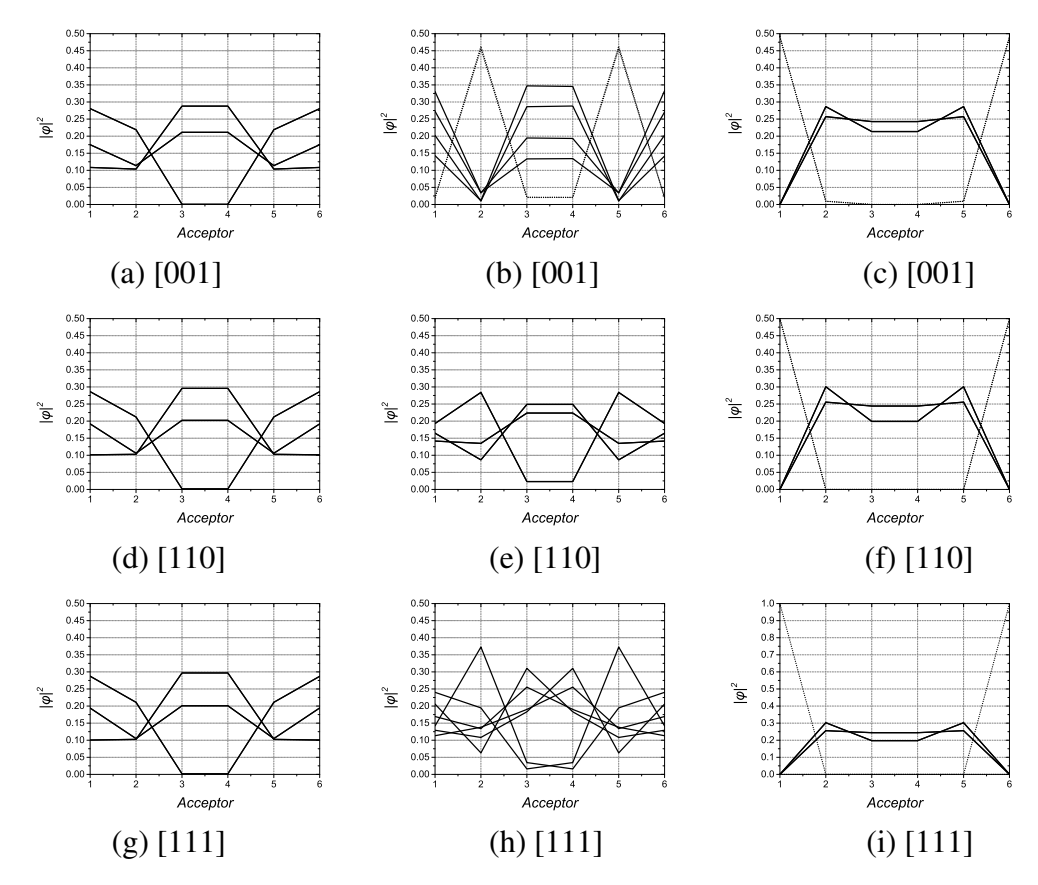


**Figure 4.14:** The total charge distribution among acceptors under different arrangements in three typical directions for the 6-acceptor linear chain when  $d_1 + d_2 = 3a_0$ : (a) the short-long arrangement in the [001] direction, (b) the uniform chain case in the [001] direction, (c) the long-short arrangement in the [001] direction, (d) the short-long arrangement in the [110] direction, (e) the uniform chain case in the [110] direction, (f) the long-short arrangement in the [110] direction, (g) the short-long arrangement in the [111] direction, (h) the uniform chain case in the [111] direction, (i) the long-short arrangement in the [111] direction. For (c), (f) and (i), the dotted lines are for the states localized at the acceptors at the end of the chain, which are always the highest states among the states involved to form the total energy ground state here. All the lines in (a), (c), (d), (e), (f), (g), the dotted line in (b) and the solid lines in (i) are doubly-degenerate.

der time-reversal symmetry) but show splittings for certain acceptor arrangements where the symmetry is lower (see §4.2.3). The four highest states in Figure 4.10, and the six highest in Figure 4.11, will be occupied by holes. In all cases there is a large gap between filled and empty states due to the effect of the strong hole-hole repulsion. Compared with Figure 4.4 for a dimer, the two significant differences are (i) the splitting of degenerate states, and (ii) the crossing between filled states in the [001] direction in Figure 4.10 (b). In general we find that the self-consistency cycle in the UHF method breaks the symmetry of the system, with different sets of eigenvectors of the Fock matrix corresponding to the same total energy; we analyse this symmetry breaking further in §4.2.3. The crossing occurs close to the changing point identified in the CI calculation, so the change in the single-acceptor energy levels in the dominant component of the CI ground state is related to a change in the ordering of single-electron states in UHF. For the 6-acceptor chain, it can be seen from Figure 4.11 that another crossing appears around  $d_1 = 1.7a_0$ , implying another similar crossing between the total energy ground state and higher excited states around that separation in the full CI and HL calculations.

The HL approach for the 4-acceptor chain (not shown) gives similar results to the CI method, including a 4-fold-degenerate ground state when  $d_1 > d_2$  and the presence of a changing point where the composition of the ground state changes; however, the changing point now appears between  $d_1 = 1.3a_0$  and  $d_1 = 1.4a_0$ , while the crossing point is still around  $d_1 = 1.4a_0$ . It once again suggests that the one-hole-per-acceptor distribution is the most important distribution for the holes in the ground state and low-lying excited states, and the system is on the insulating side of the Mott transition. This supports that the HL method is a good approximation for both the ground state and low-lying excited states, and preserves some of the main features of the energy spectrum. For the 6-acceptor chain there is only one obvious crossing between the ground state and the first excited states, as the degenerate states appear for significantly smaller values of  $d_1$  than before. But we now see two changing points for the eigenvectors: one is between  $d_1 = 1.3a_0$  and  $d_1 = 1.4a_0$ , the other is between  $d_1 = 1.6a_0$  and  $d_1 = 1.7a_0$ .

To understand in more detail the behavior of the energy gap, we show in Figure 4.12 (a) the difference between the total-energy ground state and first excited state in the [001] direction as a function of  $d_1$ . There are two regions of particular interest; the first is the neighbourhood of the crossing/changing point where the gap reduces and then increases again ( $d_1 = 1.3a_0$  to  $d_1 = 1.4a_0$ ). The minimum gap for 4 acceptors is around  $1.4a_0$  for both the CI case (solid line) and the HL case (dashed line), but shifts to shorter separations for 6 acceptors (dotted line). To show the details of the crossings among the first few states, a good choice is to show the energy difference between the ground-state and excited states as the energies shift dramatically from the short-long arrangement to the long-short arrangement according to Figure 4.9 (a). In this way, the crossings between excited states are shown as usual, while the crossing between the ground state and excited states will be reflected by the value of the difference. Here for the convenience of the further discussion, we refer to the ground state before the changing point as  $|\phi_0\rangle$ , and the ground state after the changing point as  $|\phi_0'\rangle$ . In Figure 4.12 (b), we show the energy difference between the ground-state and first 15 excited states for the full CI calculation, where we find a small gap between excited states around  $1.4a_0$ , which appears to make the 'crossings' here into anti-crossings as  $|\phi_0^{'}
angle$  is found above this gap before the changing point. It is also reasonable to believe the other 'crossings' between the ground state and the nearest excited state in the [001] direction in the full CI calculation and HL approach are anti-crossings as they arise due to the same reason. As there is a band of excited states with similar energies in Figure 4.12 (b), it is helpful to follow the energy difference between the ground state and the excited state that crosses with it, rather than the minimum gap; in Figure 4.12 (c), we show the energy difference between the previous and new ground states during the anti-crossing. This suggests that the true anti-crossing is between  $d_1 = 1.40a_0$ and  $d_1 = 1.41a_0$ , a slightly larger value than in the HL approach. The second region of interest is the right-hand side (large  $d_1$ ), where the 4-fold-degenerate manifold of ground states in the 6-acceptor system forms for smaller values of  $d_1$  than in the 4-acceptor system; alternatively, for a given  $d_1 > d_2$ , the degeneracy of the ground

state becomes better as more acceptors are involved (the same is true for the following 8-fold-degenerate and 4-fold-degenerate manifolds). This is what would be expected if the degeneracy arises from almost independent sets of localised edge states at either end of the chain because the edge states become isolated from one another more easily in the longer chain (see §4.2.5).

Figure 4.13 shows that the magnitude of the expectation value of the angular momentum vector on each acceptor in the symmetry-broken UHF solution. At the smallest values of  $d_1$  (the short-long case) the angular momentum is zero everywhere, whereas for large  $d_1$  (the long-short case) it is dominantly located at the ends of the chain. To see if this is related to possible non-trivial edge states, we show the hole distributions from each eigenvector of the Fock matrix for different arrangements in the three high-symmetry directions in Figure 4.14. Here 'shortlong' refers to  $d_1 = 1a_0$ ,  $d_2 = 2a_0$ , and 'long-short' to  $d_1 = 2a_0$ ,  $d_2 = 1a_0$ . The one-hole states do not localize at any particular acceptor under the short-long or uniform arrangements; however, for the long-short case, two states localize at the ends of the chain (the dotted lines in Figure 4.14 (c), (f) and (i)), while the others have a nearly uniform distribution across the middle. The states localized at the ends (the dotted lines in Figure 4.14 (c), (f) and (i)) are always the lowest (i.e. least favourable) states occupied by holes, which may imply the existence of the nontrivial edge states occurring in the long-short case (Since the the parabolic potential is balanced by the hole-hole repulsion, the charge rearrangements we previously identified in the non-interacting case in §3.2.2 no longer force the states localized at the end of the chain to be the highest ones and intervene to shift the edge states to the short-long limit.).

### 4.2.2.2 Large-separation case $(d_1 + d_2 = 6a_0)$

For the large-separation case, we show the behaviour of the ground-state total energy obtained from all the methods mentioned in §4.1 for a 4-acceptor chain along high-symmetry directions in Figure 4.15. The HL and UHF results are closer to the full CI results than in the small separation case, consistent with the better agreement found between the methods for larger separations in the case of pairs (Figure 4.3).

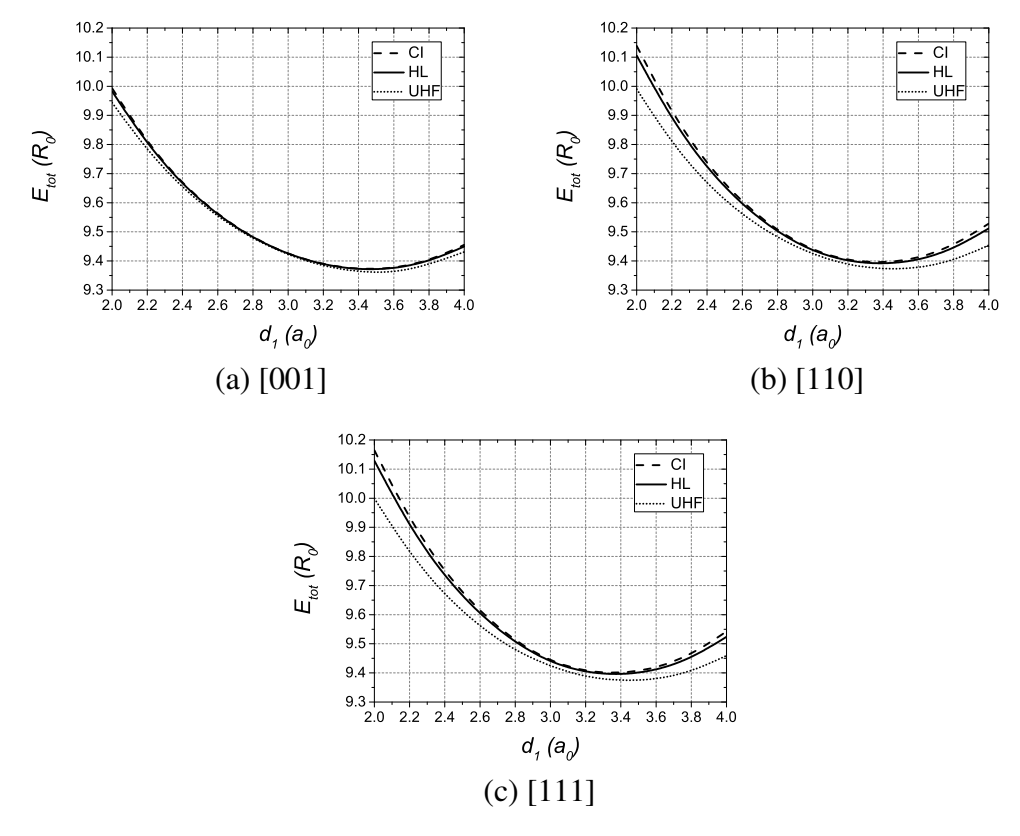


**Figure 4.15:** The total energy of the ground state in three high-symmetry directions for the large-separation case  $(d_1 + d_2 = 6a_0)$  of the 4-acceptor linear chain: (a) the [001] direction, (b) the [110] direction, (c) the [111] direction. The dashed line is for the full CI calculation, the solid line is for the HL approximation, the dotted line is for the UHF method.

The best agreement is around the uniform chain  $(d_1 = d_2 = 3a_0)$ ; once again, the HL approach offers a better approximation than UHF.

The highest 50 energy states from the full CI result are shown in Figure 4.16 and and the Fock matrix eigenvalues in Figure 4.17. In all three directions the ground-state is non-degenerate on the short-long side (small  $d_1$ ), although this is not clearly visible from Figure 4.16(a) for the [001] direction; as found for smaller spacings in §4.2.2.1, the ground state joins three other states in each case and forms a 4-fold-degenerate manifold on the right-hand side (large  $d_1$ ). This time there is no change in the character of the ground state and no (anti-)crossing visible among the states in Figure 4.16 or Figure 4.17; instead, the Fock eigenvalues show a group of four occupied states strongly separated from the unoccupied ones by the self-consistent potential. There are some small splittings visible among the eigenvalues

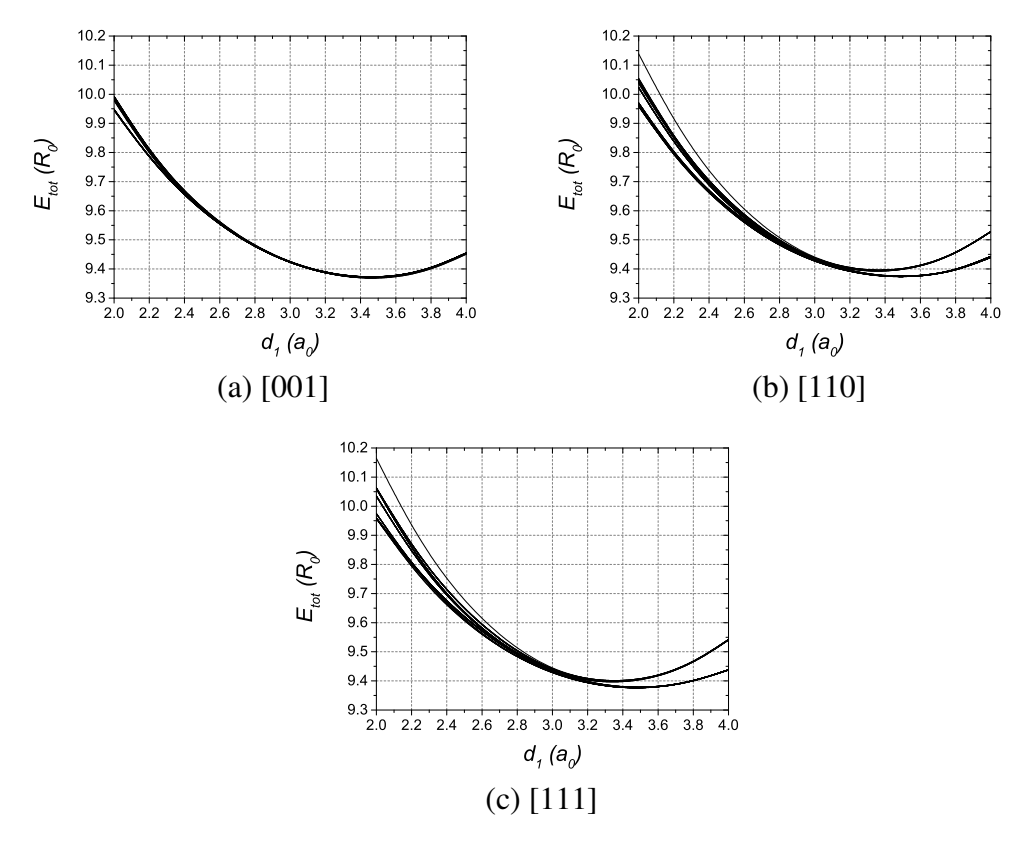


**Figure 4.16:** The total energies of the highest 50 states of the full CI result in three high-symmetry directions for the large-separation case  $(d_1 + d_2 = 6a_0)$  of the 4-acceptor linear chain: (a) the [001] direction, (b) the [110] direction, (c) the [111] direction.

in Figure 4.17 at particular geometries; these are due to the loss of symmetry in the UHF solution, as discussed in §4.2.2.1.

To compare the 4-fold-degenerate many-hole ground states obtained in the long-short limit for the small- and large-separation cases, and to understand how they relate to our previous results for non-interacting holes, we show in Figure 4.18 the energy difference between the ground state and 3 closest excited states as a function of Coulomb interaction strength for a 4-acceptor linear chain in the [001] direction (interpolating between the non-interacting and fully-interacting cases). We choose the 4-acceptor system because it provides a more straightforward comparison to the one-hole edge states of the non-interacting system, as there will be fewer other states complicating the picture. In both cases, there is a gap in the non-interacting limit, because one-hole edge states move apart in the long-short

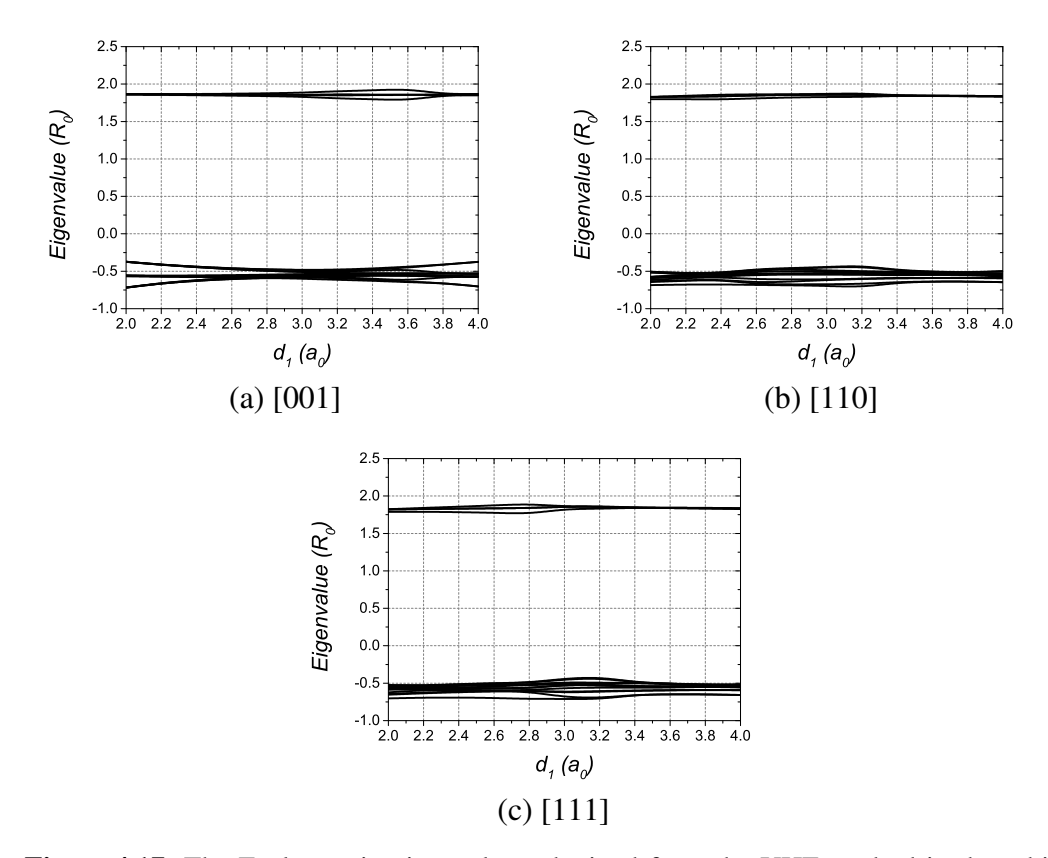


**Figure 4.17:** The Fock matrix eigenvalues obtained from the UHF method in three high-symmetry directions for the large-separation case  $(d_1 + d_2 = 6a_0)$  of the 4-acceptor linear chain: (a) the [001] direction, (b) the [110] direction, (c) the [111] direction.

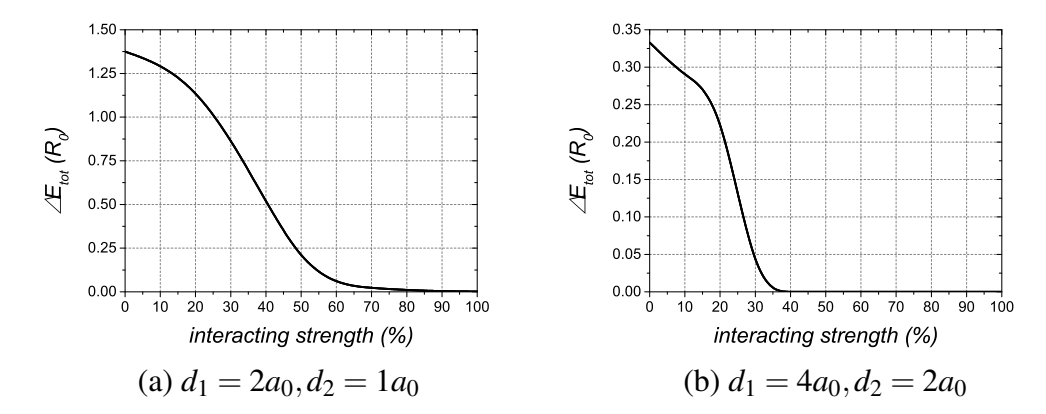


**Figure 4.18:** The energy difference between the ground state and 3 closest excited states as a function of Coulomb interaction strength (expressed as a percentage) in the long-short limit of the 4-acceptor linear chain in the [001] direction: (a) the small-separation case  $(d_1 = 2a_0, d_2 = 1a_0)$ , (b) the large-separation case  $(d_1 = 4a_0, d_2 = 2a_0)$ .

**Table 4.2:** The magnetic symmetry groups of the UHF ground states in different arrangements for the three high-symmetry directions in Hermann-Mauguin notation. Here the prime denotes operations that are only symmetries when accompanied by time reversal; the symbols m and m' are abbreviations for  $\frac{1}{m}$  and  $\frac{1}{m'}$  respectively. Here, 'FM' stands for 'ferromagnetic', 'AFM' stands for 'antiferromagnetic'

$d_1$	[001]	[110]	[111]		
Hamiltonian	$\frac{4}{m}\frac{2}{m}\frac{2}{m}1'$	$\frac{2}{m}\frac{2}{m}\frac{2}{m}1'$	$\bar{3}\frac{2}{m}1'$		
Small-separation case $(d_1 + d_2 = 3a_0)$ :					
$1.0a_0$	$\frac{4}{m}\frac{2}{m}\frac{2}{m}1'$	$\frac{2}{m}\frac{2}{m}\frac{2}{m}1'$	$\bar{3}\frac{2}{m}1'$		
$1.1a_0$	$\frac{4}{m'}\frac{2}{m'}\frac{2}{m'}(AFM)$	$\frac{2}{m}\frac{2}{m}\frac{2}{m}\frac{2}{m}1'$	$\bar{3}\frac{2}{m}1'$		
$1.2a_0$	$\frac{4}{m'}\frac{2}{m'}\frac{2}{m'}(AFM)$	$\frac{2'}{m}\frac{2'}{m}\frac{2}{m'}(AFM)$	$\bar{3}\frac{2}{m}1'$		
$1.3a_0$	$\frac{4}{m'}\frac{2}{m'}\frac{2}{m'}$ (AFM)	$\frac{2'}{m}\frac{2'}{m}\frac{2}{m'}(AFM)$	$\frac{2}{m'}(AFM)$		
$1.4a_0$ - $1.5a_0$	4m'm'	$\frac{2'}{m}\frac{2'}{m}\frac{2}{m'}$ (AFM)	$\frac{2}{m'}(AFM)$		
$1.6a_0$ - $1.7a_0$	$\frac{4}{m'}\frac{2}{m'}\frac{2}{m'}(AFM)$	$\frac{2'}{m}\frac{2'}{m}\frac{2}{m'}$ (AFM)	$\frac{2}{m'}$ (AFM)		
$1.8a_0$	4m'm'	$\frac{2}{m}\frac{2'}{m'}\frac{2'}{m'}(\text{FM})$	$\frac{2}{m'}$ (AFM)		
$1.9a_0$ - $2.0a_0$	$\frac{4}{m}\frac{2'}{m'}\frac{2'}{m'}(\text{FM})$	$\frac{2}{m}\frac{2'}{m'}\frac{2'}{m'}(\text{FM})$	$\frac{2'}{m'}(\text{FM})$		
Large-separation case $(d_1 + d_2 = 6a_0)$ :					
$2.0a_0$ - $3.2a_0$	$\frac{4}{m}\frac{2'}{m'}\frac{2'}{m'}(\text{FM})$	$\frac{2}{m}\frac{2'}{m'}\frac{2'}{m'}(\text{FM})$	$\frac{2'}{m'}(\text{FM})$		
$3.4a_0$ - $3.6a_0$	$\frac{\frac{4}{m}\frac{2'}{m'}\frac{2'}{m'}(FM)}{\frac{2}{m}}$	2'mm'	m'		
$3.8a_0$ - $4.0a_0$	4m'm'	2'mm'	m'		

limit to join two different bulk bands as shown in Figure 3.4; the 4-fold-degenerate ground state forms once the interaction strength exceeds a critical value, which is smaller in the large-separation case than in the small separation-case. This can be understood because the energy scale set by the non-interacting part of the Hamiltonian is weaker in the large-separation case, so a smaller hole-hole interaction is sufficient to overcome the parabolic confining potential.

### 4.2.3 Symmetry breaking in the UHF calculation

To investigate the symmetry breaking, we determined the symmetry of the one-hole reduced density matrices, both in the full CI case and after the convergence of the UHF calculation; the results for the UHF case are shown using the Hermann-Mauguin notation for magnetic point groups in the upper part of Table 4.2 for the small-separation case, and in the lower part for the large-separation case. For the full CI case, the results agree with the symmetry for the core Hamiltonian shown in the table. We observe that for small separations, the UHF solution always begins (for

small  $d_1$ ) with the same symmetry as the CI calculation (and the core Hamiltonian). This is a 'grey' magnetic group that contains the time-reversal operation 1', meaning that no magnetic moment has developed. The group then loses some symmetry elements as  $d_1$  increases, as magnetic moments develop; it would be more accurate to describe these missing symmetry operations as 'hidden' rather than 'lost', because they map different members of a manifold of degenerate self-consistent solutions to the UHF equations, each individually having lower symmetry, onto one another. At the points in the [001] direction where the symmetry is lowest  $(d_1 = 1.4a_0, 1.5a_0)$ and  $1.8a_0$ ), the convergence of the SCF procedure is poorer than for other separations. The origins of those lowest symmetry points are actually different. For  $1.4a_0$ to  $1.5a_0$ , the broken symmetry is due to the crossings between the occupied eigenvalues of the Fock matrix in Figure 4.10 (b). The origin of symmetry breaking is more complicated for  $1.8a_0$ . The ground state begins to show good degeneracy from  $d_1 = 1.8a_0$  according to Figure 4.9 (a), while the symmetry in the [001] direction case changes from  $\frac{4}{m'}\frac{2}{m'}\frac{2}{m'}$  (antiferromagnetic) at 1.7 $a_0$  to  $\frac{4}{m}\frac{2'}{m'}\frac{2'}{m'}$  (ferromagnetic) at  $1.9a_0$  in Table 4.2. For  $1.8a_0$ , the angular momentum is the mixture of those two along the z-axis: the two acceptors at the end show the ferromagnetic behavior while the two in the middle show the antiferromagnetic behavior. It is reasonable to believe that the further reduction of symmetry at  $1.8a_0$  is because of the changing of the degeneracy of the total energy states in full CI calculation. There the arrangement of holes begins to change but still not reach the new symmetry as the degeneracy is still not good enough at  $d_1 = 1.8a_0$ . Comparing to the behaviour of the total magnetic angular momentum for each acceptor in the different chain orientations in Figure 4.13, the breaking of symmetry is also reflected by non-zero total magnetic angular momentum and splitting into two or (at the lowest-symmetry arrangements in the [001] direction) four different inequivalent sets. The magnetization pattern shows that non-zero magnetization becomes increasingly concentrated at the ends of the chain as  $d_1$  increases, which is also true in the large-separation case. The 6-acceptor system behaves similarly to the 4-acceptor system, so we do not show the results here.

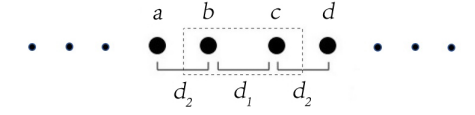


**Figure 4.19:** The schematic of the linear chain with periodic boundary conditions. a, b, c, d are the labels of acceptors,  $d_1 < d_2$  is known as the 'short-long arrangement',  $d_1 > d_2$  is known as the 'long-short arrangement'.

In the large-separation case, the symmetry is broken with respect to the underlying Hamiltonian at all separations. As previously, the broken symmetries are not really lost, but now map different solutions within the manifold of degenerate states (all having non-zero magnetic moments) into one another. For values of  $d_1$  greater than some critical value, (which depends on the direction), the symmetry is further reduced; comparing with Figure 4.16, we see this further reduction occurs when the 4-fold-degenerate ground states in the full CI calculation show very small energy differences between each other so they are hard to distinguish in the UHF calculation. By checking each data point, the switching from antiferromagnetically aligned case to ferromagnetically aligned case is found across the central ( $d_2$ ) bond as it shortens. This is closely related to the changing of the symmetry: when the inversion symmetry i is preserved but the combination (i) between i and the time reversal symmetry T is lost, the system will show the ferromagnetic behavior; when i is lost but i is preserved, the system will show the antiferromagnetic behavior.

### 4.2.4 Linear chain with periodic boundary conditions

We now turn to periodic boundary conditions. A schematic of the system is shown in Figure 4.19; (a,b,c,d) label four adjacent acceptors, with b,c in the same unit cell, and  $d_1, d_2$  are the separations. (We have swapped the separation labels relative to the convention used in the one-hole system.) Approaches based on full diagonalization (full CI calculation and the HL approach) are not extensive and hence not useful with periodic boundary conditions as discussed in §4.1.1, but the UHF method is still suitable. Since the behaviour of finite chains is found to be quite similar in the small- and large-separation cases, we report results for infinite chains only for smaller separations  $(d_1 + d_2 = 3a_0)$ .

Figure 4.20 shows the band structures of the Fock matrix eigenvalues. We only

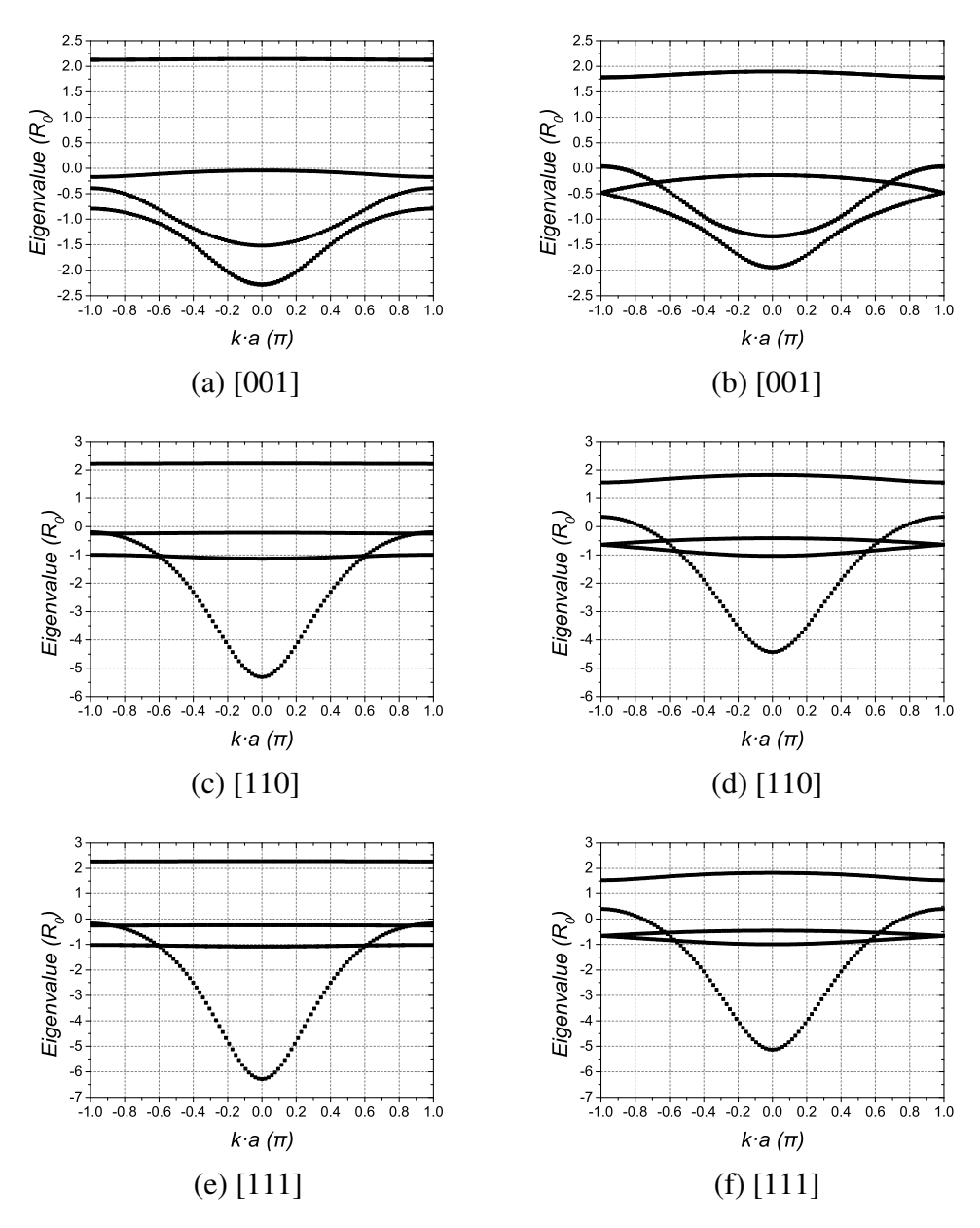


**Figure 4.20:** The band structures of the Fock matrix eigenvalues under different arrangements in three typical directions when  $d_1 + d_2 = 3a_0$ : (a) the short-long arrangement in the [001] direction, (b) the uniform chain case in the [001] direction, (c) the short-long arrangement in the [110] direction, (d) the uniform chain case in the [110] direction, (e) the short-long arrangement in the [111] direction, (f) the uniform chain case in the [111] direction.

show the results for the 'short-long' arrangement ( $d_1 < d_2$ ) in each high-symmetry direction, along with the uniform chains ( $d_1 = d_2$ ), as the short-long arrangements are equivalent to long-short under periodic boundary conditions. All the single-hole states are doubly-degenerate, so the two states at the top of each picture will be filled (two holes per cell). There is a large gap between the filled and empty bands in the short-long dimerised arrangement; for uniform chains, the bands move closer but this gap does not close, showing the existence of a cell-doubling perturbation from the self-consistent field. This is related to the broken symmetries found in the corresponding finite chain calculations: as shown in Table 4.2, we found the inversion symmetry is broken (becomes hidden) for some uniform-chain cases. It is reasonable that this also occurs under periodic boundary conditions (as shown later), leading to an inequivalence of the two atoms in the cell even for a uniform chain and implying that the band structure of the two-atom cell cannot be obtained by simply folding the bands for the one-atom cell.

In Figure 4.21, we show the behavior of the total magnetic angular momentum for individual acceptors obtained from the UHF method under different arrangements in three typical directions for the small-separation case  $(d_1 + d_2 = 3a_0)$  of the infinite chain. The labels for acceptors correspond to Figure 4.19. It can be seen that there will be broken symmetries for the nearly uniform cases in all directions, which agrees with the finite uniform cases in §4.2.3 and explains the existence of the gap found in the infinite uniform chains in Figure 4.20. Here we can also find that the symmetries are not broken near the short-long arrangement side and the long-short arrangement side in the [110] and [111] directions while the symmetries there are broken in the [001] direction. The particular form of the broken symmetry near the short-long arrangement side and the long-short arrangement side in the [001] direction is affected by the nonequivalent distribution of holes under those arrangements in the [001] direction. We will see it later in §5.3.1 that this can be fixed by including the most important next nearest transitions (all the hoping between the next nearest neighbours, and the direct hole-hole interactions between the next nearest neighbours) in the calculations. The influence of the nonequiva-

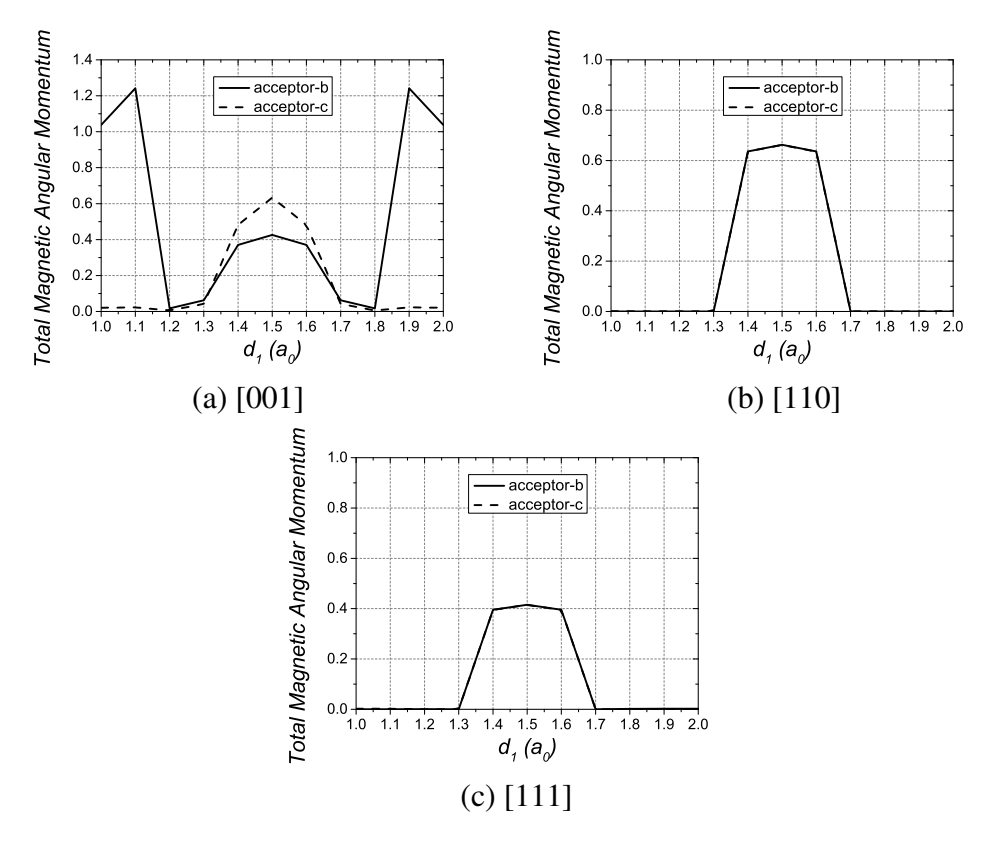


**Figure 4.21:** The behavior of the total magnetic angular momentum for individual acceptors obtained from the UHF method under different arrangements in three typical directions for the small-separation case  $(d_1 + d_2 = 3a_0)$  of the infinite chain: (a) the [001] direction, (b) the [110] direction, (c) the [111] direction.

lent distribution of holes is also discussed in §5.3.1. Here we will only compare the results from the case with nearest transitions only and the case with the most important next nearest transitions. The behavior of the magnetic angular momentum components with nearest transitions only and with the most important next nearest transitions under different arrangements in the [001] direction for the small-separation case  $(d_1 + d_2 = 3a_0)$  of the infinite chain is shown in Figure 4.22. We can see the broken symmetries are still there, but the origins of them are different. In the calculations with nearest transitions only, the x-components are non-zero near the short-long arrangement side and the long-short arrangement side in Figure 4.22 (a) and the systems are ferromagnetic as the non-zero values share the same sign; in the calculation with the most important next nearest transitions, the z-components are non-zero near the short-long arrangement side and the long-short arrangement side in Figure 4.22 (f) and the systems are antiferromagnetic as the non-zero values have

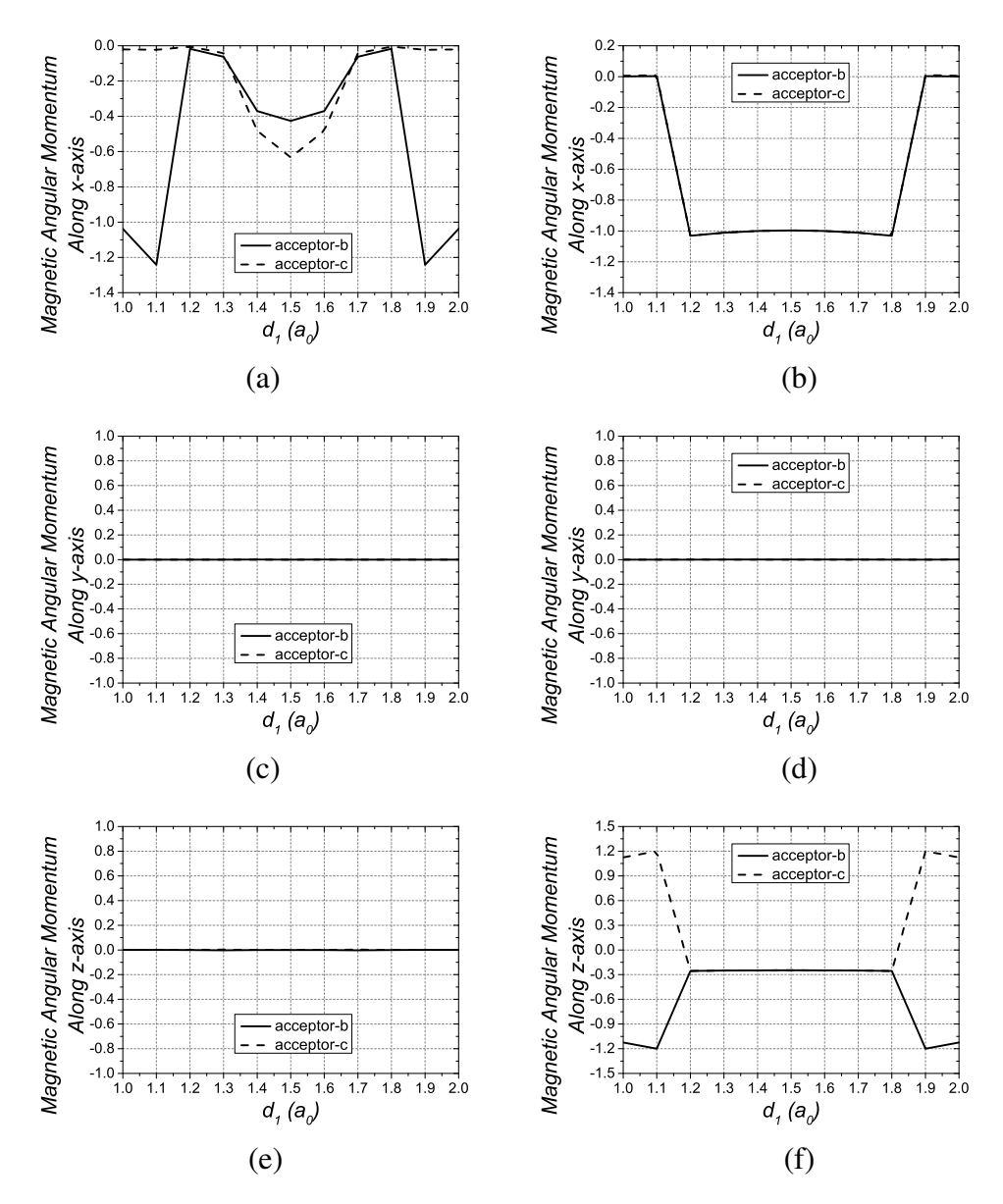


**Figure 4.22:** The behavior of the magnetic angular momentum components with nearest transitions only and with the most important next nearest transitions under different arrangements in the [001] direction for the small-separation case  $(d_1 + d_2 = 3a_0)$  of the infinite chain: (a) the x-component for the calculation with nearest transitions only, (b) the x-component for the calculation with the most important next nearest transitions, (c) the y-component for the calculation with nearest transitions only, (d) the y-component for the calculation with nearest transitions only, (f) the z-component for the calculation with nearest transitions only, (f) the z-component for the calculation with the most important next nearest transitions.

different signs. Considering including the most important next nearest transitions nearly doubles the time of the calculations and still provides the same results for the quantities listed in §4.1.5 which we are interested in, we only include the nearest transitions in our other calculations for the infinite chain.

### 4.2.5 Structure of the edge states

In order to understand the nature of the edge states, we examine the many-hole states from the full CI calculation and compare them to the UHF single-particle states, for both small-separation and large-separation cases in the 4-acceptor finite chain. Both methods show edge states localized at the acceptors at the end of the chain in the long-short arrangement  $(d_1 > d_2)$ ; however, the signatures are different. The CI method shows a manifold of almost degenerate states spanned by a basis of the form

$$|\psi_{m,n}\rangle = |\psi_m^A\rangle \otimes |\psi^{\text{bulk}}\rangle \otimes |\psi_n^B\rangle,$$
 (4.13)

where A labels the left end of the chain (acceptor a in Figure 4.7 (a)), B labels the right end (acceptor d in Figure 4.7 (a)), and  $|\psi^{\text{bulk}}\rangle$  is a common state residing in the interior of the chain (acceptors b and c in Figure 4.7 (a)). The indices m and n label different states of the ends, and the pair (m,n) together label a member of the almost degenerate manifold. The transformation from state  $|\Psi_{m,n}\rangle$  to  $|\Psi_{m',n'}\rangle$  can therefore be carried out by a unitary operator

$$\hat{U} = \hat{U}^A \otimes \hat{1}^{\text{bulk}} \otimes \hat{U}^B$$
 with  $\hat{U}^A = |\psi_{m'}^A\rangle\langle\psi_m^A|;$   $\hat{U}^B = |\psi_{n'}^B\rangle\langle\psi_m^B|.$  (4.14)

For finite chains, the eigenstates are particular linear combinations of the  $|\psi_{m,n}\rangle$  which are almost (but not quite) degenerate; the splittings decay to zero as  $d_1$  is increased, or as the chain becomes longer (see Figure 4.12). It is therefore important to look at the whole space spanned by the  $|\psi_{m,n}\rangle$ , especially when the splittings

become very small. The UHF method instead picks out a single symmetry-broken many-hole ground state in which one pair of occupied single-particle states is localized at the chain ends (acceptors a and d in Figure 4.7 (a)) while the other pair is spread over the interior (acceptors b and c in Figure 4.7 (a)). The single-hole edge states can be written as linear combinations of particular one-hole kets  $|\phi^A\rangle$  and  $|\phi^B\rangle$  localized at either end.

We can also examine the symmetries of the edge states  $|\psi_m^A
angle, |\psi_n^B
angle$  in the light of the classification of the topological phases of one-dimensional interacting fermions proposed by Reference [46]; in the long-short limit we find the characteristic phases are  $(\mu = 0, \phi = 0, \kappa = \pi)$ , hence the state is topologically non-trivial with 4-fold degeneracy, while in the short-long arrangement they are  $(\mu = 0, \phi = 0, \kappa = 0)$  (topologically trivial, non-degenerate). However, we find some differences between the small- and large-separation cases. For the 4-acceptor chain, when  $d_1 + d_2 = 3a_0$ ,  $|\psi_m^A\rangle$ ,  $|\psi_n^B\rangle$  involve only  $m_F = \pm 1/2$  states in the [001] direction, while  $|\psi^{\text{bulk}}\rangle$  includes only  $m_F=\pm 3/2$  states. This is because in the long-short arrangement case, the system can be considered as two single acceptors at the chain ends and a closely-coupled pair of acceptors between them. In that case,  $|\psi^{\text{bulk}}\rangle$  is dominated by the central pair, while  $|\psi_m^A\rangle, |\psi_n^B\rangle$  are dominated by the single-acceptor ends. Since the doubly-degenerate occupied bands at the top of Figure 4.20 (a) and (b) in the [001] direction are always formed predominantly from linear combinations of the  $\pm 3/2$  states on the two acceptors in the cell, and a single acceptor perturbed by another acceptor always has a ground state of  $m_F=\pm 1/2$ symmetry as shown in the middle range case  $(2a_0 < d \le 5a_0)$  in §4.2.1 (the influence from another acceptor can be treated as a perturbation there as the ground state and first excited state are degenerated according to Figure 4.5, and the separations for the middle range case are not too far away from the value  $2a_0$  used here), it is reasonable that  $|\psi^{\text{bulk}}\rangle$  and  $|\psi_m^A\rangle$ ,  $|\psi_n^B\rangle$  only involve  $m_F=\pm 3/2$  and  $\pm 1/2$  states respectively. When  $d_1 + d_2 = 6a_0$ , although  $|\psi^{\text{bulk}}\rangle$  is similar, the  $\{|\psi_m^A\rangle, |\psi_n^B\rangle\}$  involve also the superpositions  $\pm\{|3/2\rangle,|1/2\rangle\}$  in two of the four degenerate states. In the large-separation case the degeneracy is more nearly exact, so the properties

of individual eigenstates are not clearly defined and we should consider the space spanned by all four degenerate states together. For the 6-acceptor system (which we treat in the HL approximation), we always find the edge states composed purely of  $m_F = \pm 1/2$  states at the end of the chain (as for 4 acceptors).

We can also calculate the Zak phase for the occupied UHF states in the infinite system by using (4.11) in §4.1.4. We find that Zak phase is 0 for all arrangements in all directions, even although we find the edge states in the finite chains have non-trivial symmetries; this is consistent with the preservation of a gap in the single-particle UHF energy spectrum for all arrangements. The Zak phase is calculated by using the single-hole UHF eigenvectors, and its correspondence with the topological properties of an interacting system is still unclear; it is not surprising that it fails to describe the topological properties of the interacting system in the same way, as was previously noted for the bosonic case [61]. In the absence of a rigorously defined topological quantum number for an infinite system with interactions, the direct study of the quantum numbers characterising the edge states of the finite system, introduced by Turner *et al.*[46], provides a better insight into their topological nature.

## 4.3 Summary

In this chapter, we constructed multi-hole models for one-dimensional multi-acceptor chains based on three different methods: full configuration interaction, the Heitler-London approximation, and the unrestricted Hartree-Fock method. The HL approximation solves some of the problems with the full CI method, but the UHF method is able to calculate infinite chains under periodic boundary conditions. We found the full CI ground state is non-degenerate under the short-long arrangement in all directions, but joins other three states to form a 4-fold-degenerate manifold under the long-short arrangement for finite chains, which is followed in energy by an 8-fold-degenerate state and another 4-fold-degenerate state. By checking the dominant components of these 16 states, we found that only the levels on the acceptors at the end of the chain change between different members of the manifold, and the

overall 16-fold degeneracy comes from the product of separate sets of 4 levels on each end. The topological nature of these edge states is confirmed by the presence of non-trivial phases in the classification of one-dimensional fermion edge states by Turner et al. In the small-separation case where  $d_1 + d_2 = 3a_0$ , an anti-crossing occurs between the ground state and excited states in the [001] direction, resulting in a switch from in unhybridized ground state dominated by  $m_F = \pm 3/2$  states to a hybridized state where  $m_F = \pm 1/2$  states are also present. We found this transition is related to the crossing between the filled UHF single-particle states. The UHF solution loses part of the symmetry of the Hamiltonian. We also found the further broken symmetries related to the crossing between Fock matrix eigenstates and changing of the degeneracy of the total energy states in full CI calculation in the [001] direction. The loss of symmetry corresponds to the emergence of static moments on each acceptor in the UHF approach. We also obtained the UHF band structures of the Fock matrix eigenvalues. We found there is a large gap between the filled and empty states in a dimerised chain, which does not fully close in the uniform case, showing the existence of a period-doubling perturbation. Since a gap is maintained throughout the transition from short-long to long-short arrangements, the Zak phase is constant (and equal to zero), despite the observation of non-trivial many-body edge states in the long-short case. Hence, this method does not capture the formation of topological edge states, while the previous method introduced by Turner et al (which was designed for interacting systems) can well characterise their topological properties. The nature of the bulk-edge correspondence in such interacting systems requires further investigations.

## **Chapter 5**

# **Two-dimensional Systems**

In this chapter we will investigate the acceptors in two-dimensional system under both one-hole model and multi-hole models. For the one-hole model, we will study rectangular structures, ladders and zigzag structures; for the multi-hole model, we will study 4-acceptor rectangles (by full CI and UHF), infinite ladders and honeycomb lattice (by UHF only). In 2D systems, we have the possibility to form topological insulators, where counter-propagating edge states are rigorously protected by time-reversal symmetry. So the condition for the forming of topological insulators will be investigated.

# 5.1 Two-dimensional system

Now we are going to investigate two-dimensional ordered systems. Two dimensions can show richer behaviours than one dimension as a new degree of freedom is introduced into the system. So, besides the competition between acceptor-hole Coulomb interactions and the hole-hole interactions in the multi-hole model, the new degree of freedom also could introduce some new symmetry protected topological states.

We consider several different types of rectangular structure. First, we consider finite rectangular systems under the one-hole model, where a one-dimensional line of atoms is closed in two dimensions to form a rectangular loop, as a function of the bond lengths between the acceptors. As the system is 2-dimensional, there are several inequivalent ways of varying the bond lengths. We lower the symmetry in three different ways, starting from the two arrangements shown in Figure 5.1. It

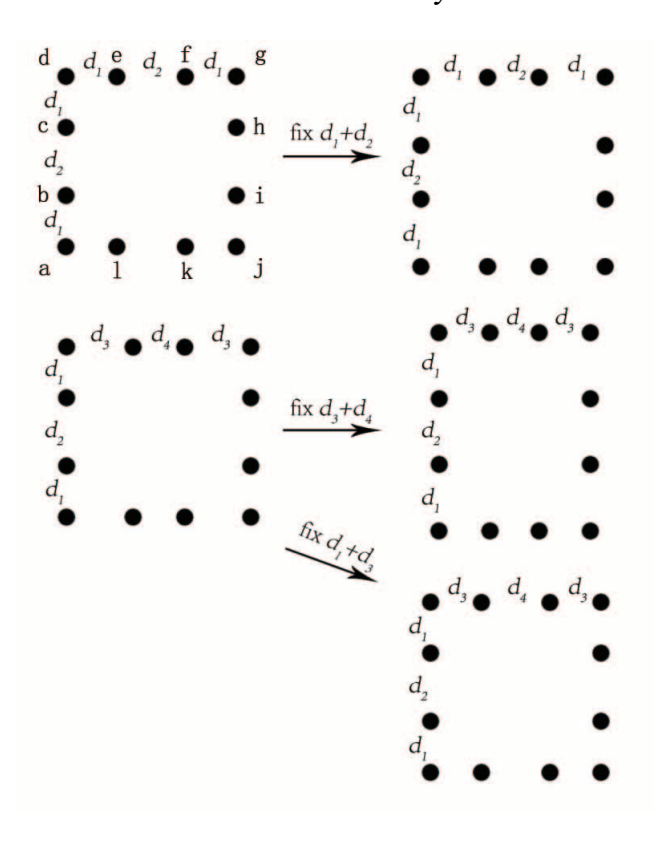


**Figure 5.1:** Three different evolutions from two arrangements. The left column shows two initial arrangements, the arrows pointing to the right column stands for three possible evolutions, the texts above arrows give the fixed sum while the separations not mentioned there are fixed separately. There are always 12 acceptors in the system.

can be seen that there are two kinds of arrangements in the left column: one of them requires four different bond lengths, and the other requires two different bond lengths. In order to illustrate the evolution of the electronic structure as a function of a single parameter, as in the previous finite chain calculations, we fix the sum of one of the pairs of separations in each case, as labeled in Figure 5.1.

Next we move on to consider structures that have some two-dimensional character but which are infinite in only one direction. The simplest such structure is a ladder. It can be described as consisting of two acceptor chains close to each other, so that an acceptor in one chain can interact with the neighbouring acceptor in the other chain. In this case, we can not only do the calculation for ladders of finite length, but also investigate the properties of an infinite ladder by carrying out the calculation in momentum space. Once again we allow for the possibility of alternat-

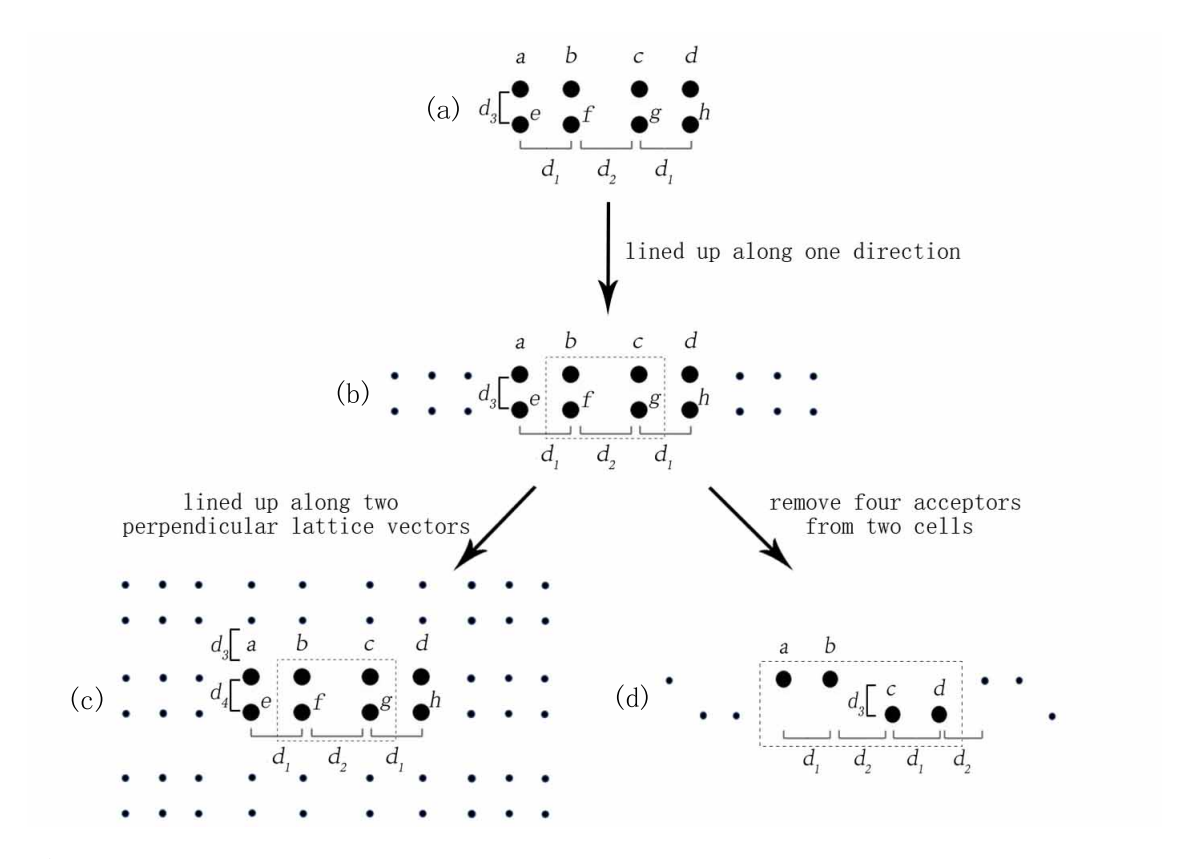


**Figure 5.2:** The arrangement for the ladder, the rectangle lattice and the zigzag structure: (a) the finite ladder, (b) the infinite ladder, (c) the rectangle lattice, (d) the infinite zigzag structure.

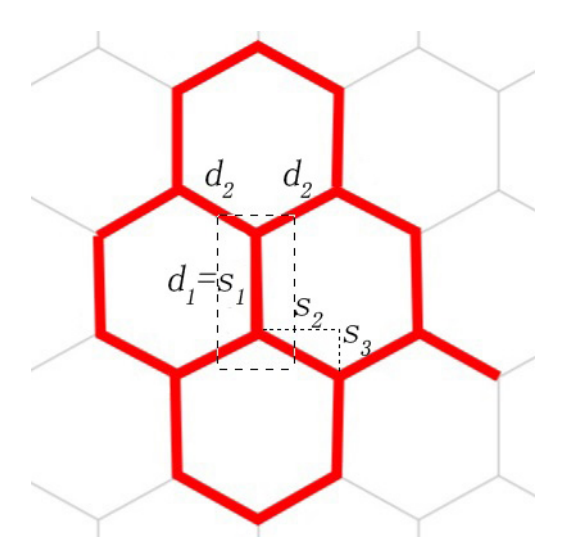


**Figure 5.3:** The arrangement for the honeycomb lattice:  $d_i$  and  $s_i$  are the separations where  $d_1 = s_1$  and  $d_2^2 = s_2^2 + s_3^2$ .  $s_i$  will only be used in the non-equivalent case (where  $d_1 \neq d_2$ ).

**Table 5.1:** The localizing of the highest 16 states under the long-short arrangement:  $\{d_1, d_2\}$  stands for the rectangle with two groups of separations when  $d_1 + d_2 = 7a_0$ ,  $\{d_3, d_4\}$  stands for the rectangle with four groups of separations when  $d_3 + d_4 = 7a_0$ ,  $\{d_1, d_3\}$  stands for the rectangle with four groups of separations when  $d_1 + d_3 = 7a_0$ .

Evolution	Localizing
$\{d_1, d_2\}$	$\{b,c,e,f,h,i,k,l\}$
$\{d_3, d_4\}$	$\{a,d,g,j\}$
$\{d_1,d_3\}$	$\{e,f,k,l\}$

ing bond lengths along each chain, so a unit cell will contain four acceptors.

After doing those calculations, a fully two-dimensional rectangular lattice can be generated by bringing more acceptor-ladders close to each other. There are now two perpendicular lattice vectors. Alternatively, another arrangement could be obtained from the ladder is the zigzag; as shown in Figure 5.2, it can be obtained by removing a total of four acceptors from two adjacent cells in the infinite ladder, leaving once again four acceptors per unit cell.

The final 2-dimensional arrangement we consider is the honeycomb lattice. This is known to display interesting topological properties in other contexts [62, 63, 64]. Here we will first discuss the perfect honeycomb lattice, which has the same separation between any two nearest neighbours, so there are two acceptors in one cell and  $d_1 = d_2 = d$  as shown in Figure 5.3. Then we will investigate distortions of the honeycomb structure that would be appropriate to implantation of acceptors onto the (010) plane of a (cubic) silicon crystal, in the real doped silicon to see whether the property found in the perfect honeycomb lattice still exist or not. There  $d_1 \neq d_2$  so we will use  $s_i$  in Figure 5.3 to describe the system.

# 5.2 Two-dimensional non-interacting system results

### 5.2.1 Finite systems without hole-hole interactions

For the calculation without hole-hole interactions, we will follow the same model which is introduced in Chapter 3. The separations towards the third neighbour is at least  $7a_0$  in the system studied here, so the cutoff of the acceptor potential will be same (we will only consider the next nearest influence due to the same reason

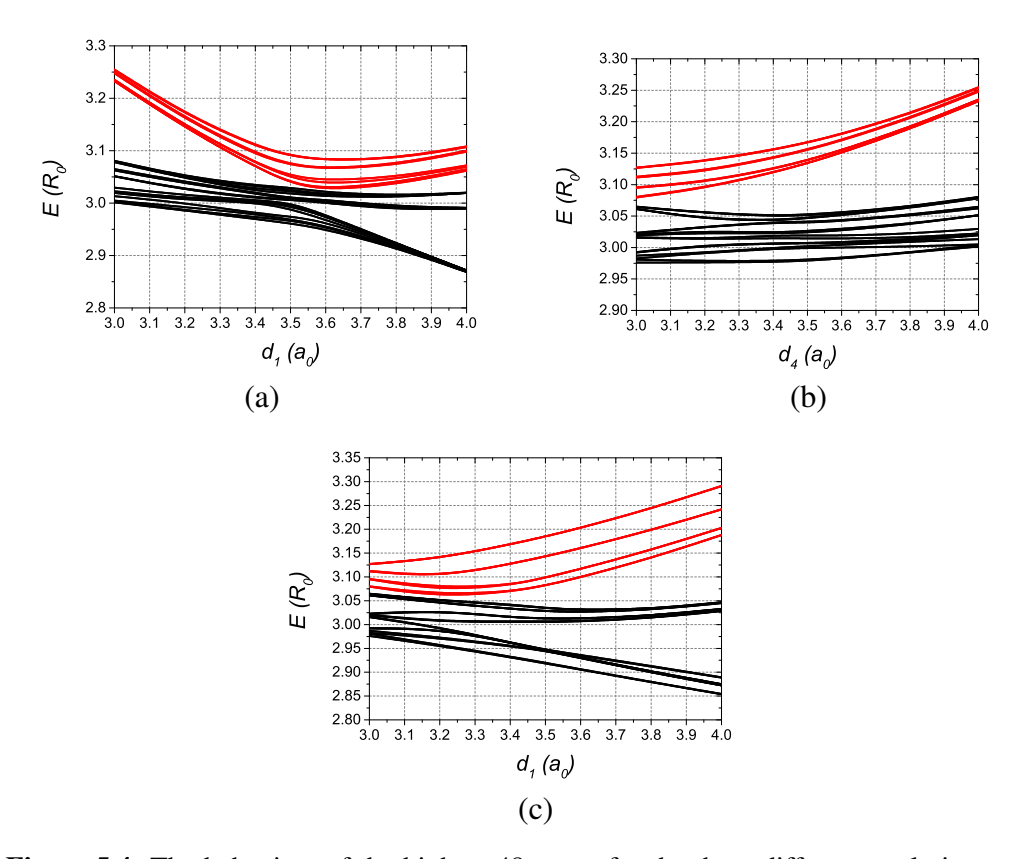


**Figure 5.4:** The behaviors of the highest 48 states for the three different evolutions under the one hole model: (a) the rectangle with two groups of separations when  $d_1 + d_2 = 7a_0$ , (b) the rectangle with four groups of separations when  $d_1 = 3a_0$ ,  $d_2 = 4a_0$  and  $d_3 + d_4 = 7a_0$ , (c) the rectangle with four groups of separations when  $d_1 + d_3 = 7a_0$ ,  $d_2 = 4a_0$  and  $d_4 = 3a_0$ . The red lines are for the 16 states split away from the others.

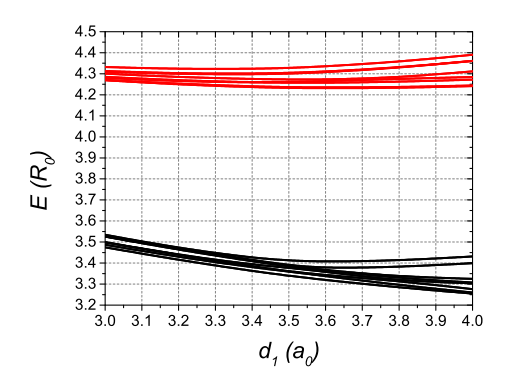


**Figure 5.5:** The behaviors of the highest 32 states for finite length ladder when  $d_1 + d_2 = 7a_0$  and  $d_3 = 4a_0$ .

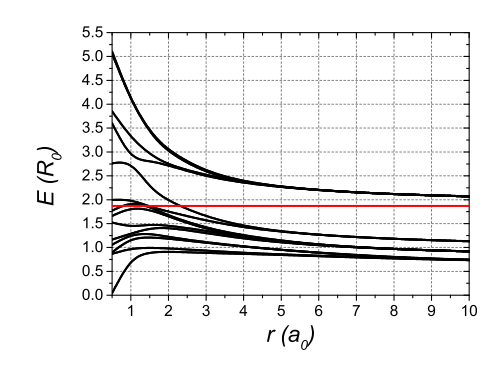


**Figure 5.6:** Eigenenergies in a pair of acceptors as a function of separation r for the cubic case in the [001] direction and the single acceptor ground state. The black lines are for the acceptor pair, the red line is for the single acceptor.

mentioned in §3.2.1).

### 5.2.1.1 Rectangles

For the convenience of calculation we put all the acceptors in the x-z plane with two perpendicular sides being parallel to the x-axis and z-axis respectively. The behaviors of the highest 48 states for the three different evolutions when the fixed length equals to  $7a_0$  are shown in Figure 5.4. Here we only show the highest 48 states because there are 4 degenerate ground states on each of the 12 acceptors, and there will be a large gap between those states and others. We still name the case where  $d_1 < d_2$  the short-long arrangement (short bond nearest the corner of the rectangle, the left hand side of Figure 5.4 (a)) and the case where  $d_1 > d_2$  the long-short arrangement (long bond nearest the corner of the rectangle, the right hand side of Figure 5.4 (a)). In the same way, we can name  $d_3 < d_4$  the shortlong arrangement (the right hand side of Figure 5.4 (b)) and  $d_3 > d_4$  the long-short arrangement (the left hand side of Figure 5.4 (b)) for Figure 5.4 (b), while  $d_1 < d_3$ the short-long arrangement (the left hand side of Figure 5.4 (c)) and  $d_1 > d_3$  the long-short arrangement (the right hand side of Figure 5.4 (c)) for Figure 5.4 (c). It can be seen that the highest 16 states (red states) will split away from the others at the right-hand side of the pictures in all cases as well as the left-hand side of Figure 5.4 (a). Considering the arrangements for the left-hand side of Figure 5.4 (a) and the right-hand side of Figure 5.4 (b) are same, there are only three distinct arrangements

(three different arrangements at the right-hand side of the pictures). So from now we will only consider three distinct arrangements. By investigating the eigenvectors of the highest 16 states (red states), we find that those states will be localized at some particular acceptors as shown in Table 5.1. By checking the electrostatic terms, it can be found that this localization is the result of the nonequivalent potential as we found for 1D arrays in §3.2.2. Those acceptors have more short-bonded neighbours connected to them and a short-bonding will be accompanied with a large attractive Coulomb potential, which will force the hole to localize at those acceptors in an independent-hole model. So the nonequivalent potential here plays the same role as the parabolic potential in one-dimensional case, and we can expect that these localized states will also appear in a large loop. But in the multi-hole model, the nonequivalent potential will be balanced by the hole-hole interactions as discussed in §4.2.2.1, so this localization should disappear there.

#### 5.2.1.2 Finite ladders

Here we consider the smallest system for a ladder strucutre, so there are 8 acceptors in the system. We show the highest 32 states for the finite length ladder when  $d_1 + d_2 = 7a_0$  and  $d_3 = 4a_0$  in Figure 5.5. It needs to be pointed out that there is no gap between those states and the others at the long short end (the right hand side of Figure 5.5), instead, the gap is between the highest 16 states (red states) and the rest. This occurs because the system will behave like two strongly-bonded pairs with separation  $r = 3a_0$  and four single acceptors at the long short end (the right hand side of Figure 5.5). According Figure 5.6, the ground state energy for the single acceptor drops into the gap between the ground states and others in the acceptor pair when  $r \geq 3a_0$ . This makes the eigenvalues of the ladder split into two parts under the long-short arrangement: the energy level above the red line (the single acceptor ground state) in Figure 5.6 forms the red lines in Figure 5.5, the rest (the red line and the black line below it in Figure 5.6) form the bulk band (black lines in Figure 5.5). By investigating the eigenvectors of the highest 16 states (red states), we find that those states will be localized at acceptors {b,c,f,g} only for all the cases. And again, this localization is due to the nonequivalent potential. Comparing

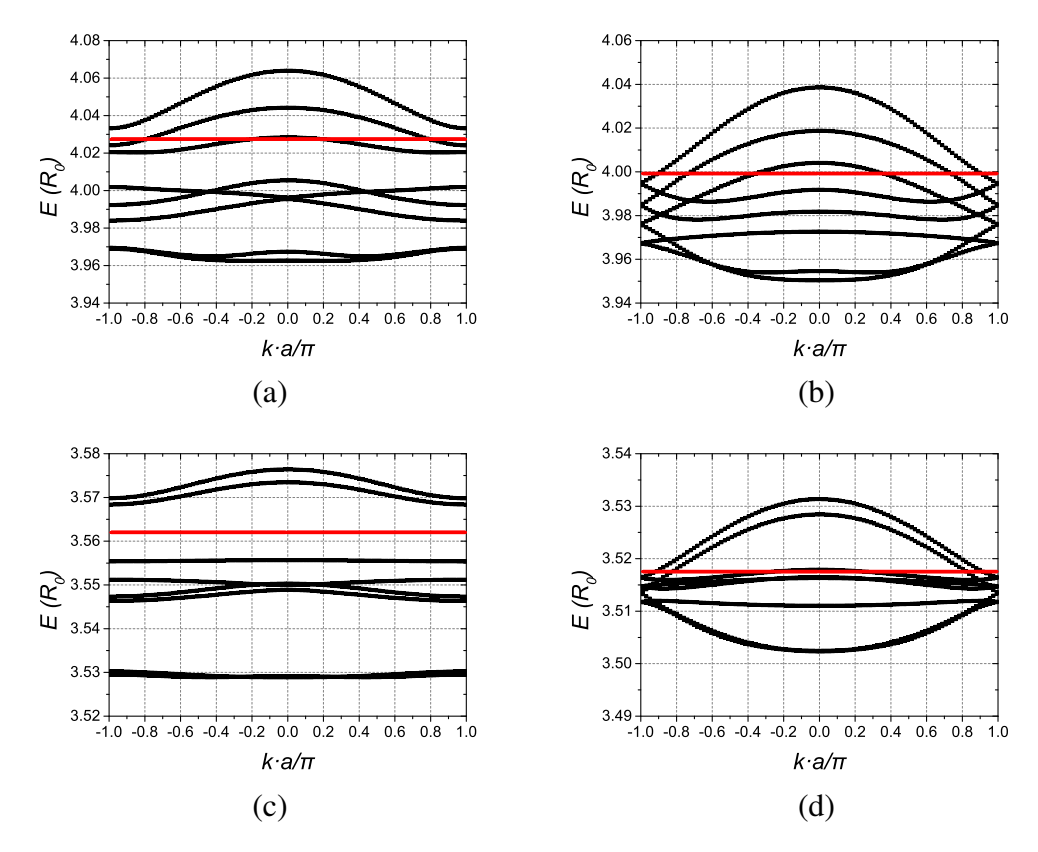


**Figure 5.7:** The band structure of the highest 16 states for the infinite ladder under different arrangements when  $d_1 + d_2$  and  $d_3$  are fixed separately. (a) the small separation case when  $d_1 = 3.5a_0$ ,  $d_2 = 4.5a_0$ , and  $d_3 = 4.5a_0$ , (b) the small separation case when  $d_1 = d_2 = 4a_0$ , and  $d_3 = 4.5a_0$ , (c) the large separation case when  $d_1 = 4a_0$ ,  $d_2 = 6a_0$ , and  $d_3 = 6a_0$ , (d) the large separation case when  $d_1 = d_2 = 5a_0$ , and  $d_3 = 6a_0$ . The black lines stand for the bands, the red lines stand for the Fermi energy.

to the results in §3.2.2, it is not surprising to find that those acceptors correspond to the one next to the end of the chain in the one-dimensional case. So, again, the nonequivalent potential here plays the same role as the parabolic potential in the one-dimensional case. It means that these localized states are true edge states as indicated in §3.2.2 and could also be expected to appear in a longer ladder. As the edge states found in one-dimensional case are topological states, we can also expect the edge states in the ladder to be topological. In the next section, the topological origin of the edge states under the short-long arrangement (the left hand side of Figure 5.5) will be proved.

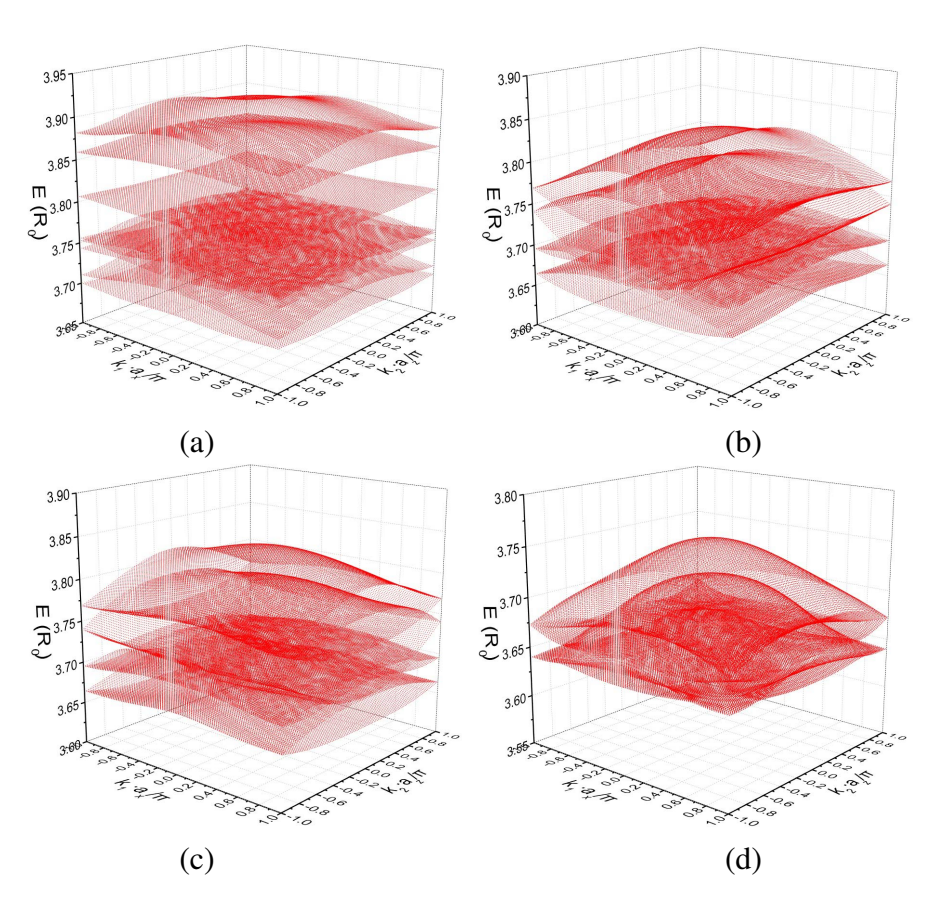


**Figure 5.8:** The band structure of the highest 16 states for the rectangle lattice under different arrangements when  $d_1+d_2$  and  $d_3+d_4$  are fixed separately. (a)  $d_1=d_3=3.5a_0$  and  $d_2=d_4=5.5a_0$ , (b)  $d_1=d_2=4.5a_0$ ,  $d_3=3.5a_0$  and  $d_4=5.5a_0$ , (c)  $d_1=3.5a_0$ ,  $d_2=5.5a_0$  and  $d_3=d_4=4.5a_0$ , (d)  $d_1=d_2=d_3=d_4=4.5a_0$ .

**Table 5.2:** The Zak phase Z computed under a variety conditions under cubic one-hole model after mod  $2\pi$  in the 2D systems.

Arrangement	Long-short	Short-long
Infinite ladder (level 1 and 2)	0	π
Infinite ladder (level 3 and 4)	0	π
Zigzag structure (level 1 and 2)	π	0
Zigzag structure (level 3 and 4)	0	0

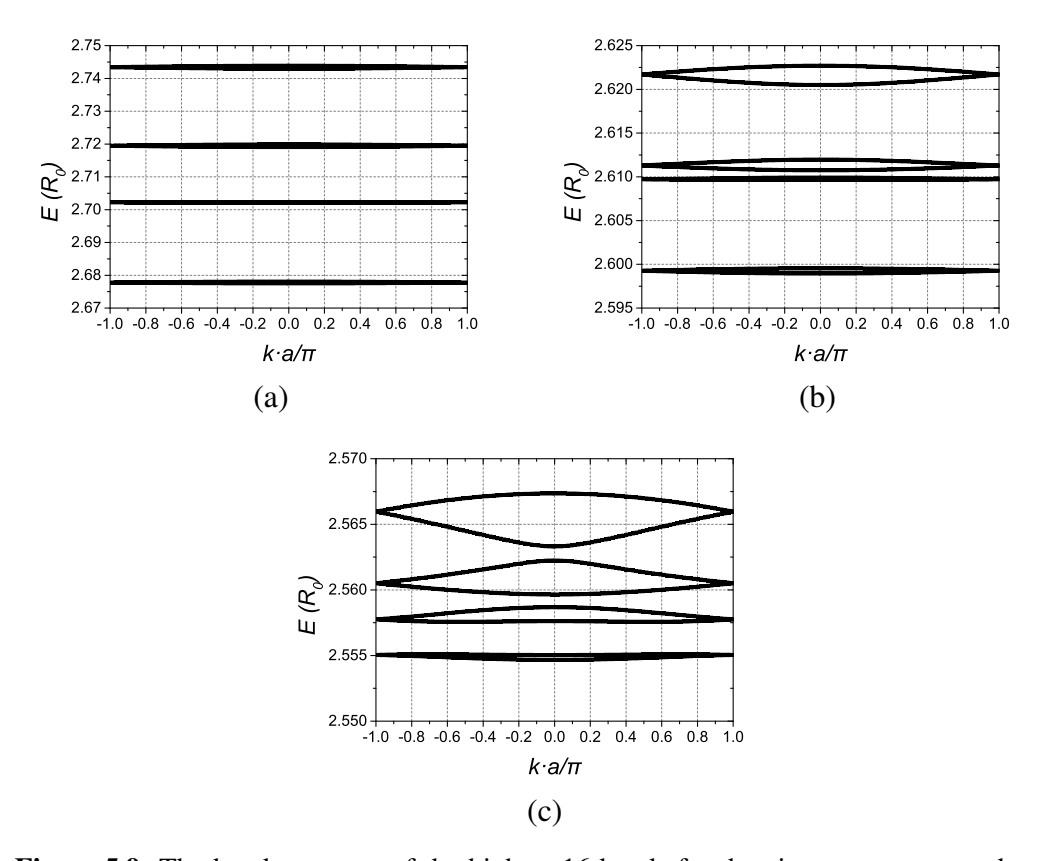


**Figure 5.9:** The band structure of the highest 16 bands for the zigzag structure under different arrangements when  $d_1 + d_2$  and  $d_3$  are fixed separately. (a)  $d_1 = 3.5a_0$ ,  $d_2 = 5.5a_0$ , and  $d_3 = 5a_0$ , (b)  $d_1 = d_2 = 4.5a_0$ , and  $d_3 = 5a_0$ , (c)  $d_1 = 5.5a_0$ ,  $d_2 = 3.5a_0$ , and  $d_3 = 5a_0$ .

### 5.2.2 Infinite systems without hole-hole interactions

Now we are going to investigate three infinite systems: the infinite ladder, the rectangular lattice and the zigzag strucutre. As mentioned in §5.2.1, all the acceptors are in the x-z plane and two perpendicular sides are parallel to the x-axis and z-axis separately. Here following previous chapters, we will call it 'the short-long arrangement' when  $d_1 < d_2$ , and call it 'the long-short arrangement' when  $d_1 > d_2$ . Here we should point out that the names of arrangements correspond to the structure shown in Figure 5.2. As  $d_1$  is the inter-cell separation in the infinite ladder and become intra-cell separation in the zigzag strucutre, the short-long arrangement in the zigzag strucutre actually corresponds to the long-short arrangement in the infinite ladder and *vice versa*.

The band structures for the infinite ladder, the rectangular lattice and the zigzag

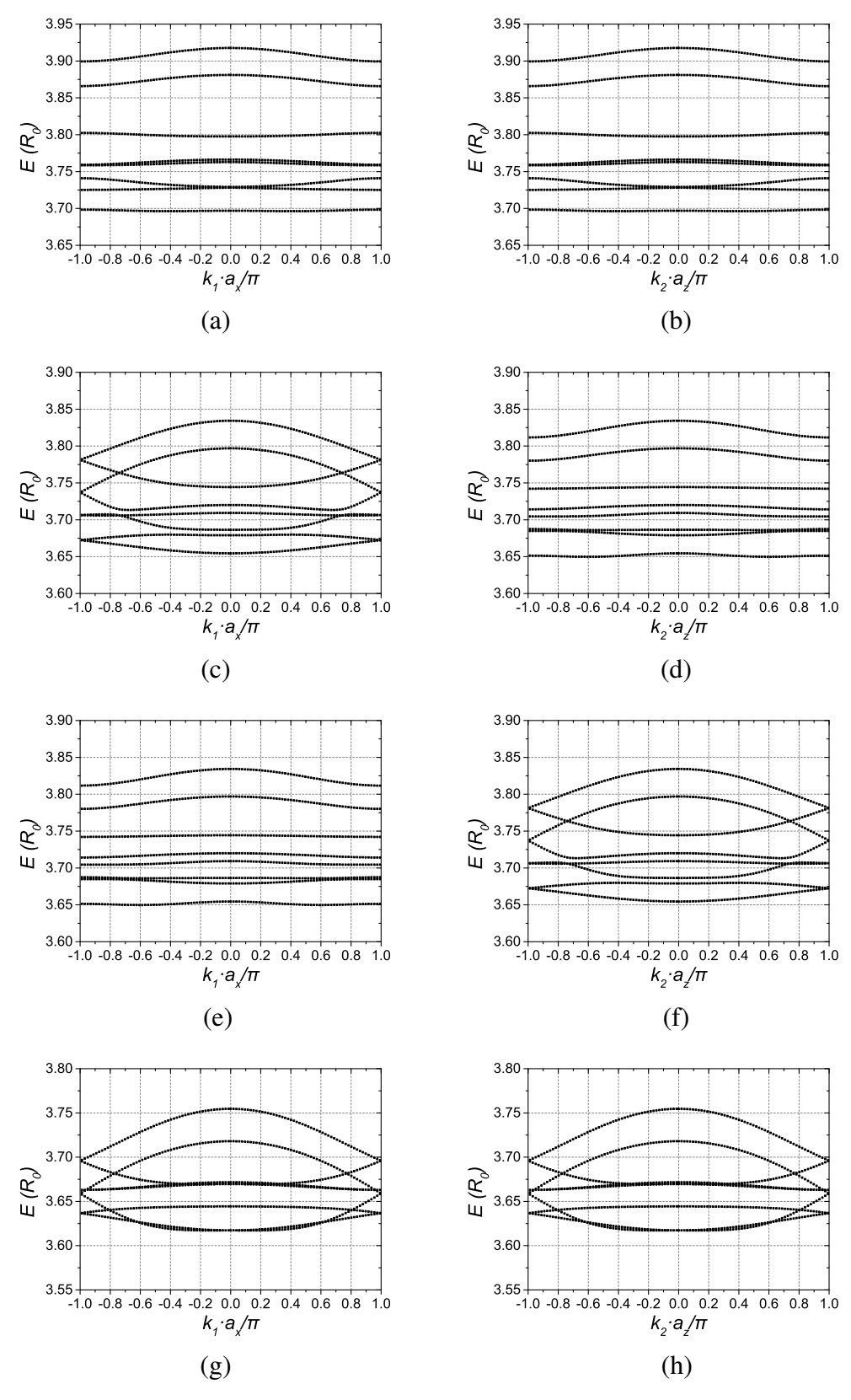


**Figure 5.10:** The cuts through of the highest 16 states for the rectangle lattice under different arrangements when  $d_1 + d_2$  and  $d_3 + d_4$  are fixed separately. (a)  $d_1 = d_3 = 3.5a_0$  and  $d_2 = d_4 = 5.5a_0$ , while  $k_2 = 0$ , (b)  $d_1 = d_3 = 3.5a_0$  and  $d_2 = d_4 = 5.5a_0$ , while  $k_1 = 0$ , (c)  $d_1 = d_2 = 4.5a_0$ ,  $d_3 = 3.5a_0$  and  $d_4 = 5.5a_0$ , while  $d_4 = 5.5a_0$  and  $d_4 = 5.5a_0$  and  $d_4 = 5.5a_0$  and  $d_4 = 5.5a_0$ , while  $d_4 = 5.5a_0$  and  $d_5 = 5.5a_0$  and  $d_6 = 5.5a_0$  and  $d_7 = 5.5a_0$  and  $d_8 = 5.5a_0$  and  $d_8 = 6.5a_0$  and

strucutre are shown in Figure 5.7, Figure 5.8 and Figure 5.9 respectively. We also show cuts through the two-dimensional band structure for the rectangle lattice in Figure 5.10 for the convenience of further discussion. Here it should be pointed out that the short-long arrangement and the long-short arrangement along any direction are same for the infinite ladder and the rectangle lattice, but these arrangements will become different systems in the zigzag case. So we still only need to show one of them in the figures for the infinite ladder and the rectangle lattice, while all pictures are required for the zigzag strucutre. It can be seen that infinite ladder is insulating under the short-long or long-short arrangement of the large separation case only, while the other cases shown in Figure 5.7 are metallic. Comparing Figure 5.7 with Figure 3.6, it can be seen that the result for the infinite ladder looks like two copies of the results for the infinite chains. And as a ladder can be considered as two interacting chains, the interactions between them will lead to the splitting between two copies of the results for the infinite chains. Comparing Figure 5.7 with Figure 5.10, we can see that the cuts through of the rectangle lattice result will show the strucutre of the relevant infinite ladder result. It can also be seen that Figure 5.8 (b) is similar to Figure 5.8 (c), as each system can be achieved from another by rotating  $\frac{\pi}{2}$  in the x-z plane. It also can be seen that only the rectangular system in Figure 5.8 (a) is insulator while the others are metallic. From Figure 5.9, it can be seen that the zigzag structures are always insulating. We can also find an anti-crossing between the filled states and empty states under the long-short arrangement ( $d_1 = 5.5a_0$ ,  $d_2 = 3.5a_0$ , and  $d_3 = 5a_0$ ). Comparing Figure 5.9 with the infinite chain cases in Figure 3.6, the results for the zigzag structure looks like the results for the infinite chain after slightly moving the bands close to each other. Considering the zigzag structure is a 2D system which can be achieved by moving a cell away from the cells next to it in the perpendicular direction of the one dimensional chain in Figure 3.1 (b), the difference in the band structure can be explained. Although the zigzag structure is a 2D system, it works like a one dimensional system, where the 2D transition between acceptor-b and acceptor-c in Figure 5.2 (d) can be treated as a 1D transition with a effective separation  $d_{eff}$ . The effective separation  $d_{eff}$  is larger



**Figure 5.11:** The arrangement for the 4-acceptor rectangle.

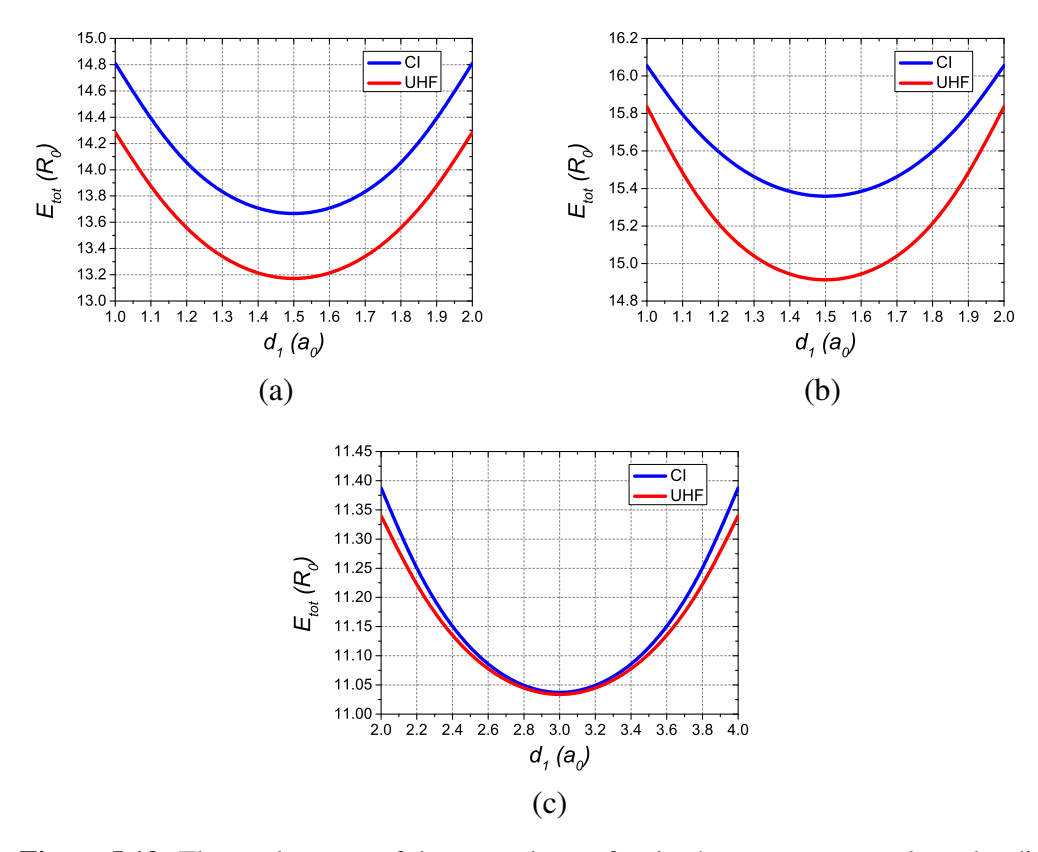
than  $d_2$ . So the long-short arrangement of the zigzag structure is closer to a uniform chain than the uniform arrangement of the zigzag structure.

We also calculate the Zak phase value for the infinite ladder and the zigzag strucutre with the Equation 4.11 as these systems are infinite only along one direction. The Zak phase values are shown in Table 5.2. Comparing with Table 3.2, it can be seen that the Zak phase values for the infinite ladder agree with the results of one-dimensional chain; they are all going to be nontrivial topological edge states under the short-long arrangements for all filled levels (highest 2 levels for the infinite chain and highest 4 levels for the infinite ladder). Considering the parabolic potential in the finite chain as well as the nonequivalent potential in the finite ladder will force the states to be localised on the acceptors at the end of the relevant systems under the one hole model, here the states localised on the acceptors next to the end of the ladder under the short-long arrangement in the finite ladder are topological edge states, which agrees with what we found in the finite chain in §3.2.2. For the zigzag structure, nontrivial states can only be achieved by the first two level (level 1 and 2) under the long-short arrangement. Remembering the long-short arrangement in the zigzag structure are actually corresponding to the short-long arrangement in the infinite ladder and results for the infinite ladder agree with results for the infinite chain, results for the zigzag structure also agree with results for the infinite chain.

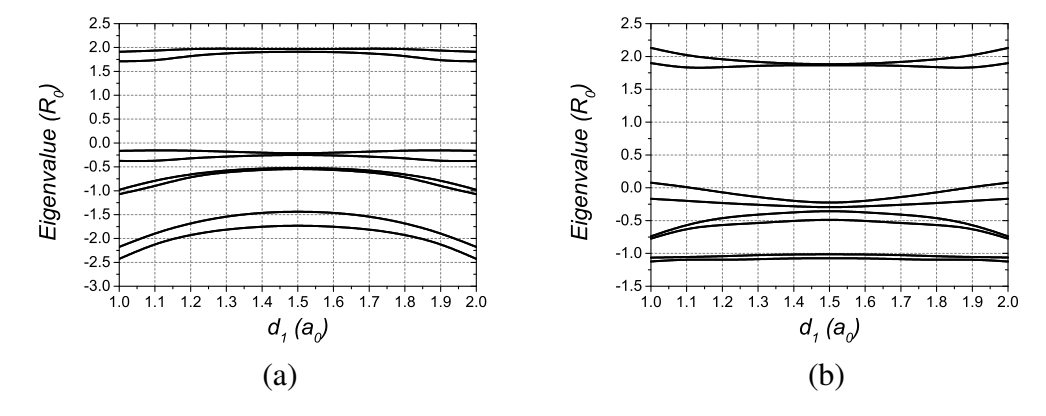
# 5.3 Two-dimensional interacting system results

### **5.3.1** Finite system with hole-hole interactions

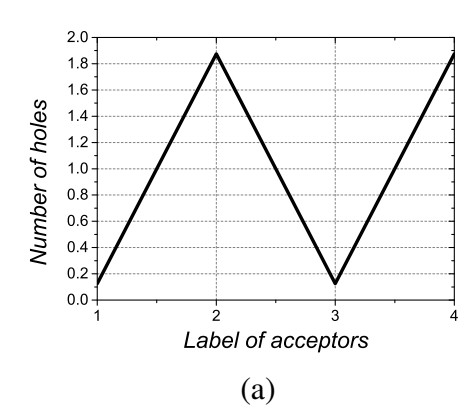
We now introduce interactions between the holes. We expect these will screen out some of the differences in electrostatic potential that dominated the independenthole calculations, as well as potentially introducing new physics arising from cor-



**Figure 5.12:** The total energy of the ground state for the 4-acceptor rectangle under different multi-hole models: (a) small separation  $(d_1 + d_2 = 3a_0)$  calculations with nearest transitions only, (b) small separation  $(d_1 + d_2 = 3a_0)$  calculations with all possible transitions, (c) large separation  $(d_1 + d_2 = 6a_0)$  calculations with all possible transitions. The blue line is for the full CI calculation, the red line is for the UHF method.



**Figure 5.13:** The behavior of the Fock matrix eigenvalues obtained from the UHF method under different arrangements for the small separation case  $(d_1 + d_2 = 3a_0)$  of the 4-acceptor rectangle: (a) calculations with nearest transitions only, (b) calculations including next-nearest transitions.



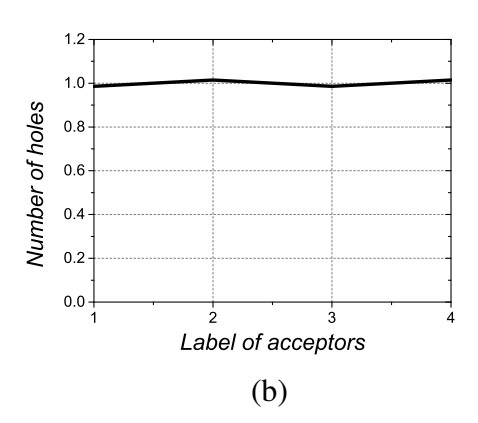


**Figure 5.14:** The distributions of holes under the UHF model for the small separation uniform chain case  $(d_1 = d_2 = 1.5a_0)$  of the 4-acceptor rectangle: (a) calculations with nearest transitions only, (b) calculations including next-nearest transitions.

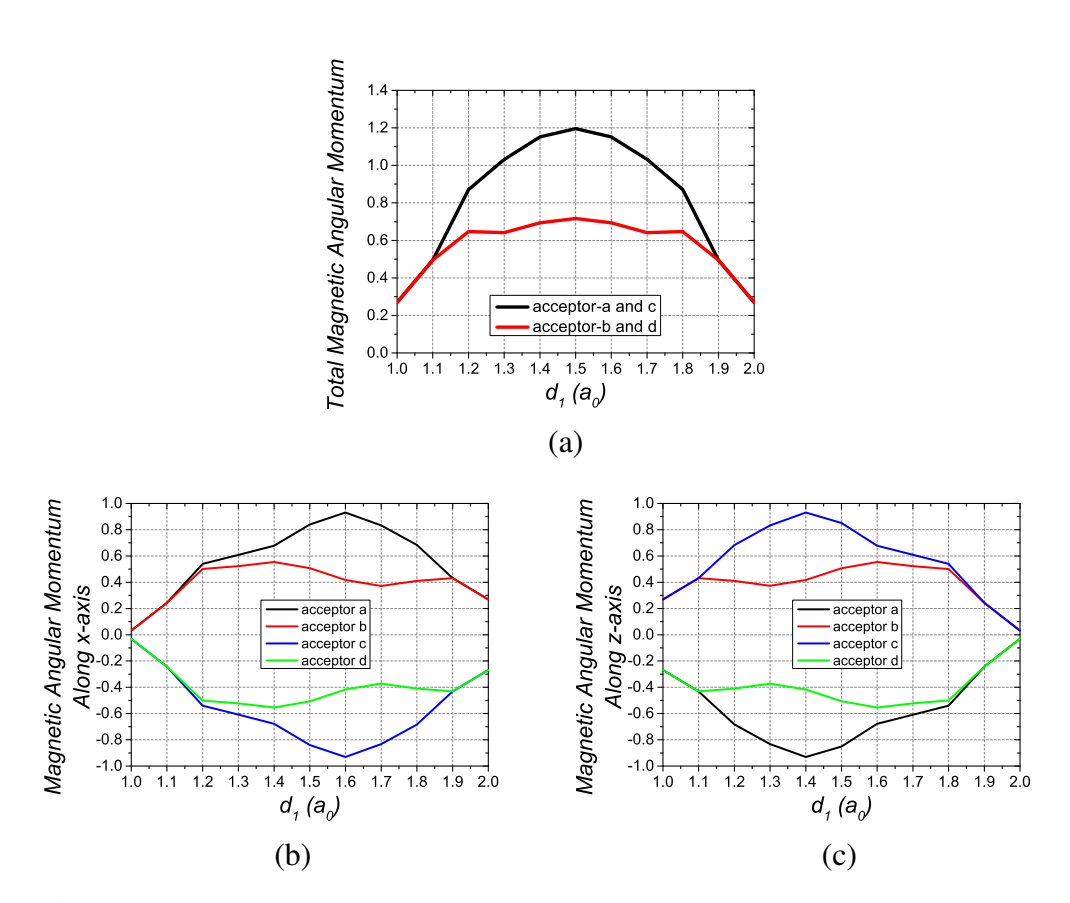


**Figure 5.15:** The behavior of the magnetic angular momentum obtained from the UHF method with all possible transitions for the small separation case  $(d_1 + d_2 = 3a_0)$  of the 4-acceptor rectangle: (a) the total magnetic angular momentum for individual acceptor, (b) the magnetic angular momentum along x-axis, (c) the magnetic angular momentum along z-axis.

**Table 5.3:** The largest fractional differences of the total energy between the full CI calculation and the UHF method in 4-acceptor chains and rectangles for the small separation cases  $(d_1 + d_2 = 3a_0)$ .

Systems	Largest fractional difference
4-acceptor chain in [001] direction	2.51%
4-acceptor chain in [110] direction	2.67%
4-acceptor chain in [111] direction	2.70%
4-acceptor rectangle with nearest transitions only	3.63%
4-acceptor rectangle with all possible transitions	2.91%

relations. We use two of the same methods as in Chapter 4: the full CI method (which includes all hole-hole correlations but scales exponentially with the size of the system) and the UHF method (which treats the interactions between the holes in mean-field theory). As it is pointed out in §4.1, the full CI method can provide the most accurate result, while the UHF method is easier to deal with.

As the calculations under the multi-hole model could be very expensive for a large system with many acceptors, we will discuss only a small finite 2D system here, the 4-acceptor rectangle as shown in Figure 5.11. Here we consider two case: the case with all the acceptor-hole and hole-hole interactions, and the case with only the nearest-neighbour transitions and hole-hole interactions. The total energy of the ground state under different multi-hole models is shown in Figure 5.12. It can be seen that the large separation case  $(d_1 + d_2 = 6a_0)$  is more accurate than the small separation case  $(d_1 + d_2 = 3a_0)$  as the difference between the full CI and UHF results is smaller in the large separation case. The largest fractional difference of the total energy between two methods for the small separation cases are shown in Table 5.3. Comparing with the result of the one-dimensional chain, it can be seen that the rectangle case with all possible transitions shows the similar value of the largest fractional differences towards the the one-dimensional case while the case only with the nearest influence has a slightly larger fractional difference. So the UHF method is still a valid approximation towards the full CI calculation for the cases with all possible transitions, especially for the large separation one  $(d_1 + d_2 = 6a_0)$ . By comparing the eigenvectors of the full CI results and the UHF results, we also find that the arrangement of holes in the UHF calculation is corresponding to one of the largest components of the ground state in the full CI case. The other largest components are obtained by applying the inversion or time-reversal operations to that component, which help to protect the inversion symmetry and the time reversal symmetry in the full CI case.

The behavior of the Fock matrix eigenvalues obtained from the UHF method under different arrangements for the small separation case  $(d_1 + d_2 = 3a_0)$  is shown in Figure 5.13. It can be seen that the Fock matrix eigenvalues behave in the similar way, so the next-nearest transitions will not dramatically change the behavior of the Fock matrix eigenvalues. The distributions of holes under the UHF model for the small separation uniform chain case are shown in Figure 5.14. The distribution with only the nearest transitions corresponds to the breaking of symmetry by a charge density wave, while including next nearest transitions provides a better prediction for the distribution of holes as the one-hole-per-acceptor arrangement is expected on the insulator side of the Mott transition due to the geometry symmetry of the system. The eigenvectors of the full CI calculation show that the dominant components of the ground state for the case with only the nearest transitions are also localized at a pair of particular acceptors. This will influence the symmetry of the ground state, so the next-nearest influence should be included in the calculations based on the symmetry of the ground state (such as the calculation of parity as the required inversion symmetry could be lost). For the calculations where the symmetry will not play an important role, considering the next nearest transitions will nearly double the time of the calculation, only taking the nearest transitions into account could be an option. But including the next nearest transitions is still the first choice to fix the nonequivalent distribution of holes. Here we should point out that this nonequivalent distribution of holes is not going to happen in every calculations without next-nearest transitions. So for the arrangements without the nonequivalent distribution of holes, the calculation only with the nearest transition can still provide an accurate prediction. According to our experience, the nonequivalent distribution of holes is more likely to happen in the system involving very small separations. We believe this is relative to the competition between hole-hole interactions and holecore Coulomb potentials. For the cases involving very small separations, removing the next-nearest transitions has larger influence on the hole-hole interactions than potentials, which makes it possible for holes to be localised on particular acceptors.

The behavior of the magnetic angular momentum obtained from the UHF method with all possible transitions for the small separation case  $(d_1+d_2=3a_0)$  is shown in Figure 5.15. The splitting of lines in Figure 5.15 (a) implies the symmetry breaking exists in the system according to the discussion in §4.2.3. It also can be seen that the total magnetic angular momentum for each individual acceptor is non-zero for all the tested arrangement. The angular momentum along x-axis and z-axis are also not zero for those arrangement. They will show the inverse behavior as switching the value of  $d_1$  and  $d_2$  is equivalent to rotating the system for  $\frac{\pi}{2}$  in the x-z plane. The lines in Figure 5.15 (b) and (c) also support that the symmetry will breaks in different way along x-direction and z-direction. It will be anti-ferromagnetic when the magnetic angular momentum component is along that direction, and ferromagnetic when the magnetic angular momentum component is perpendicular to that direction.

#### **5.3.2** Infinite ladder with hole-hole interactions

Now we introduce hole-hole interactions into the infinite ladder system introduced in §5.2.2. We still call it 'the short-long arrangement' when  $d_1 < d_2$ ; and call it 'the long-short arrangement' when  $d_1 > d_2$ . Here we take  $d_1 + d_2 = 3a_0$  and  $d_3 = 1.5a_0$  as an example, because the finite system is calculated under the similar separations. For the convenience of calculations, only the nearest transitions are included, as our main target is to investigate the uniform ladder and there is no nonequivalent distribution of holes in the uniform ladder without next-nearest transitions. According to §5.3.1, although this may change the charge distribution and the eigenvectors for the other arrangements, the energy will not change dramatically for those cases. So the following discussions for the uniform ladder are based on the accurate perdition of the system, while the energy behaviors for the other arrangements are also reliable.

The band structures of the Fock matrix eigenvalues under different arrangements when  $d_1 + d_2 = 3a_0$  and  $d_3 = 1.5a_0$  are shown in Figure 5.16. Here the sys-

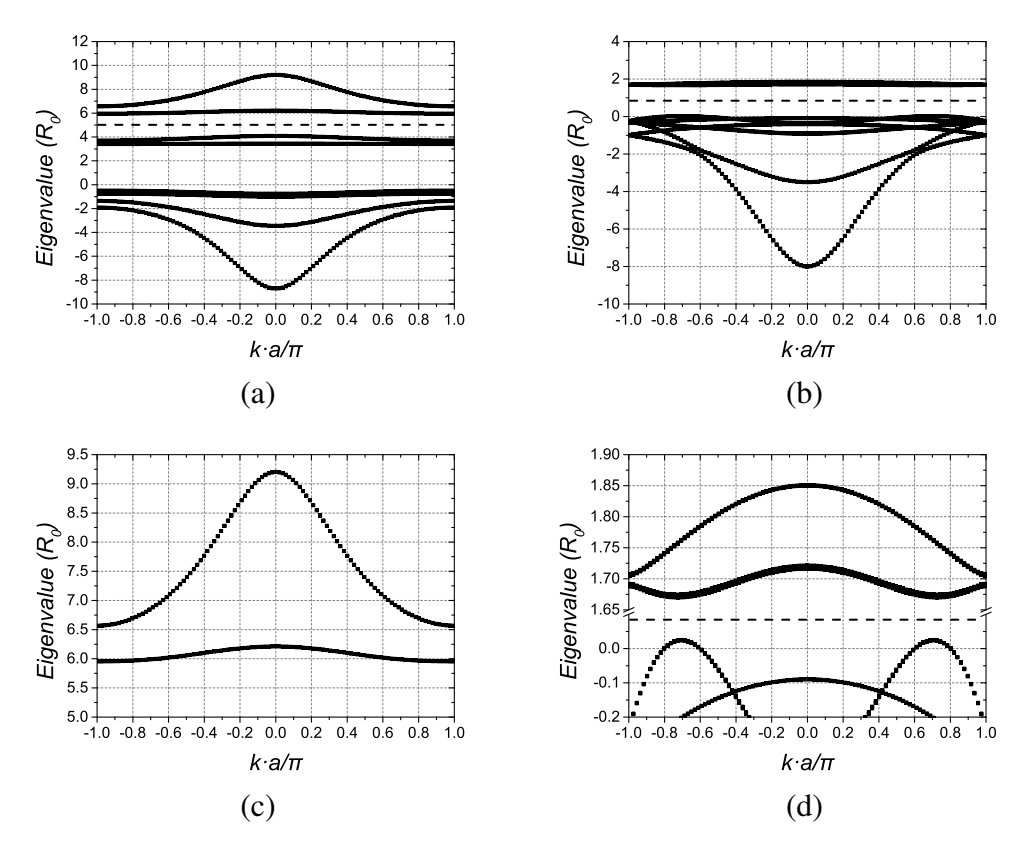


**Figure 5.16:** The band structures of the Fock matrix eigenvalues under different arrangements for the infinite ladder when  $d_1 + d_2 = 3a_0$  and  $d_3 = 1.5a_0$ : (a) the short-long arrangement, (b) the uniform ladder, (c) the detail of the highest 4 eigenvalues in the short-long arrangement, (d) the detail of the high energy eigenvalues in the uniform ladder. The dash line is the Fermi energy.

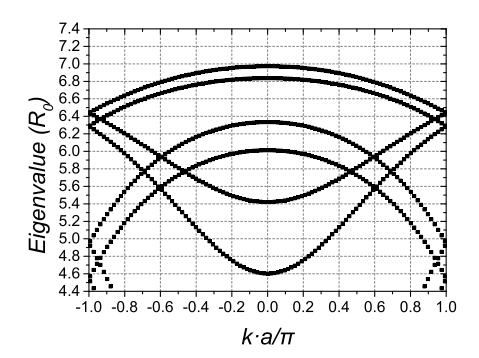


**Figure 5.17:** The band structures of the Fock matrix eigenvalues for the high energy states of the infinite ladder without hole-hole interactions when  $d_1 = d_2 = d_3 = 1.5a_0$ .

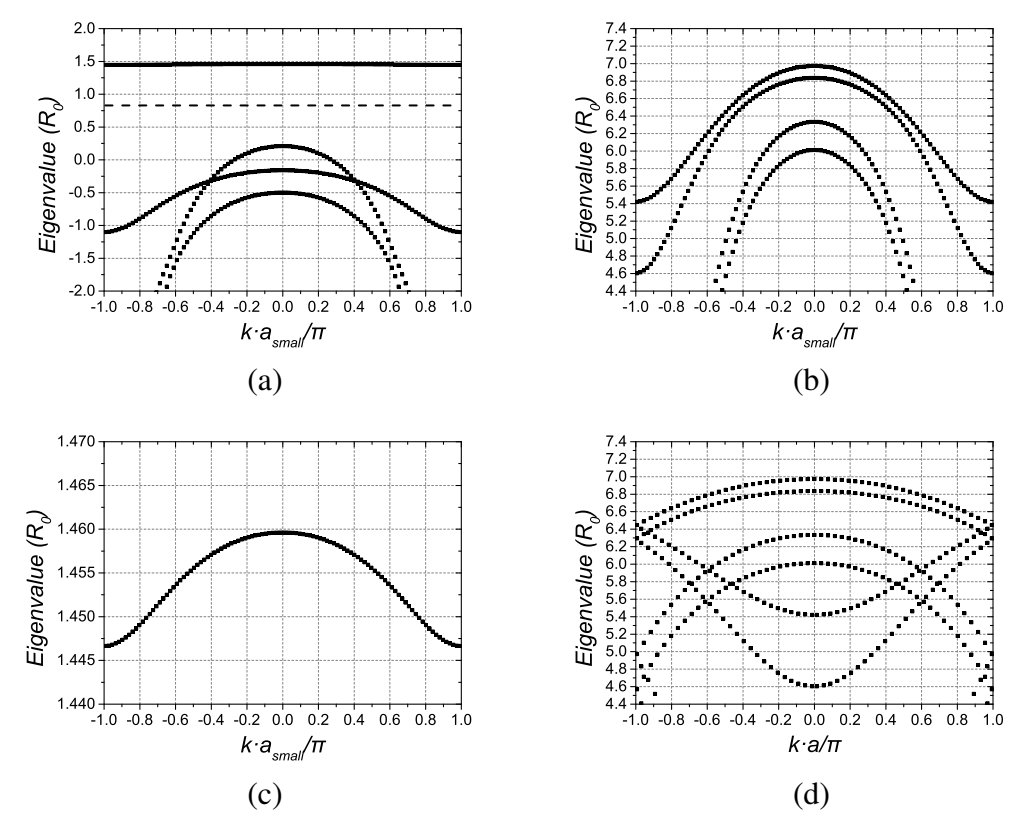


**Figure 5.18:** The band structures of the Fock matrix eigenvalues in the small cell case (2 acceptors/cell) with and without interacting between holes for the high energy states when  $d_1 = d_2 = d_3 = 1.5a_0$ : (a) the band structure with interactions between holes, the dash line is the Fermi energy, (b) the original band structure without interactions between holes, (c) the details of the band structure for highest 2 states with interactions between holes, (d) the zone folding version of band structure for the small cell without interactions between holes.

tems for the short-long arrangement and the long-short arrangement are same, so we will only show the short-long arrangement case. All the systems are insulating here as the filled states (the topest band) are above the Fermi energy in Figure 5.16. Remember there will be 4 holes in total as it has 1 hole per acceptor, it can be found that there are two anti-crossing points between the filled states and empty states in the uniform ladder. The further calculations show that the anti-crossing will disappear once  $d_3$  reaches 1.9 $a_0$ . Remember the anti-crossing in the one dimensional chain along [001] direction in §4.2.2.1 leads to some interesting behaviors (like symmetry breaking in §4.2.3), it is necessary to investigate the origin of the anti-crossing here.

The band structures of the Fock matrix eigenvalues without hole-hole interac-

**Table 5.4:** The parity of 4 typical symmetry points and the relevant  $Z_2$  invariant v for different separation d.

d	$\delta_{11}$	$\delta_{12}$	$\delta_{21}$	$\delta_{22}$	ν	System Parity
$2.3a_0$	1	1	1	-1	1	Odd
$2.35a_0$	1	1	1	-1	1	Odd

tions for the high energy states when  $d_1 = d_2 = d_3 = 1.5a_0$  are shown in Figure 5.17. The calculation is done by only removing the hole-hole interactions, so any differences between Figure 5.16 (d) and Figure 5.17 correspond to the effect of the hole-hole interactions. Comparing with Figure 5.16 (d), it can be seen that the anticrossing in Figure 5.16 (d) and the crossing in Figure 5.17 show up at the similar places. As we found earlier in the one dimensional system, it will open a gap between the filled states and empty states among the eigenvalues of Fock matrix when the UHF method is used. So the anti-crossing in Figure 5.16 (d) is coming from the crossing in Figure 5.17 when a gap is opened by the hole-hole interactions. To give a clear picture of how the crossing (and the anti-crossing as well) is generated, we show the band structures of the Fock matrix eigenvalues in the small cell (2 acceptors/cell) with and without interactions between holes for the high energy states when  $d_1 = d_2 = d_3 = 1.5a_0$  in Figure 5.18. We also show the zone folding version of band structure for the small cell case without interaction between holes, where we replaced the cell constant  $a_{small}$  by a in the previous large cell case. We can find that there is no anti-crossing in Figure 5.18 (a), and the large cell case with interactions has a larger value for the total energy than the corresponding small cell case. By taking a small cell, we allow the symmetry breaking in limited ways without changing the physical structure of the system. The large cell is equivalent to two small cells, and therefore allows broken symmetries that double the periodicity of the system. These cannot occur in the small cell, and one of them makes the system reach a more stable ground state in our calculation.

#### **5.3.3** Honeycomb lattice with hole-hole interactions

As introduced in §5.1, the 2D honeycomb lattice offers interesting topological properties in other contexts [62, 63, 64]. So the topological states are likely to be

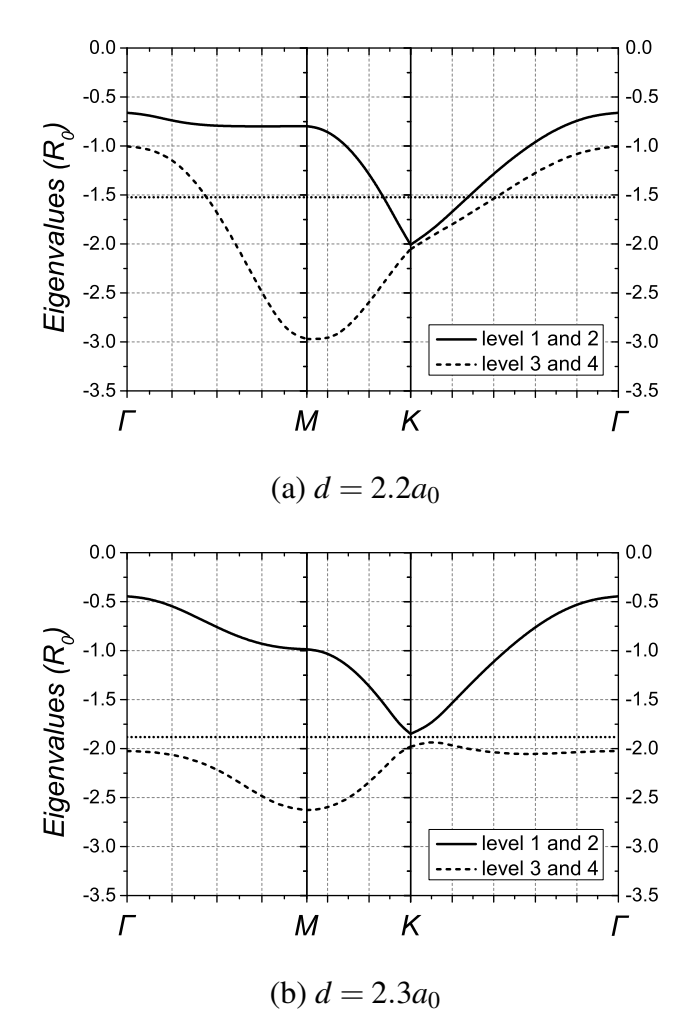


**Figure 5.19:** The band structure of the highest 4 Fock matrix eigenvalues for the honeycomb lattice when  $d = 2.2a_0$  and  $d = 2.3a_0$ : (a)  $d = 2.2a_0$ , (b)  $d = 2.3a_0$ . The dot line is the Fermi energy.

achieved in this kind of structure. Previously, calculations for the honeycomb lattice under the spherical one-hole model (without the cubic symmetry term in Equation 2.1 and hole-hole interactions) were done by S. Bhattacharyya under a summer project [65]. There he found nontrivial topological edge states for the perfect honeycomb lattice when  $d_1 = d_2 = 6a_0$ . He also investigated the existence of the nontrivial topological edge states by varying the angles with  $d_1 = d_2 = 6a_0$ . It was found that these states will be hold until the angle  $\angle_{12}$  between  $d_1$  and  $d_2$  decreases to  $0.54\pi$ . The detail can be found in S. Bhattacharyya's unpublished report [65].

After proving the nontrivial topological origin of the edge states in the honeycomb lattice under the spherical one-hole model, the next step is to investigate the

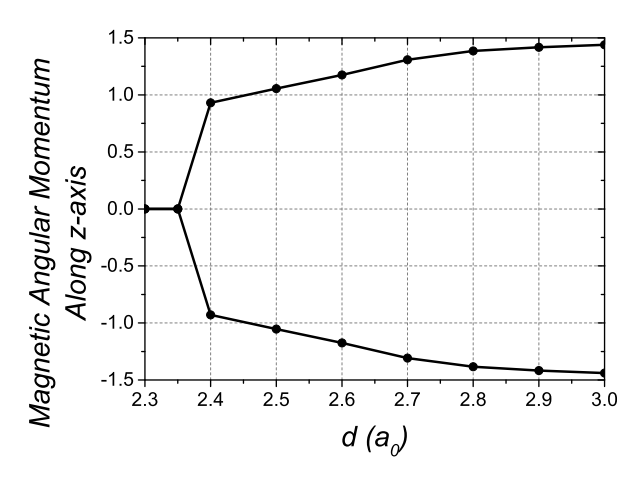


**Figure 5.20:** The magnetic angular momentum along z-axis on different acceptors in the unit cell for the honeycomb lattice: two lines are for two different acceptors in the cell.

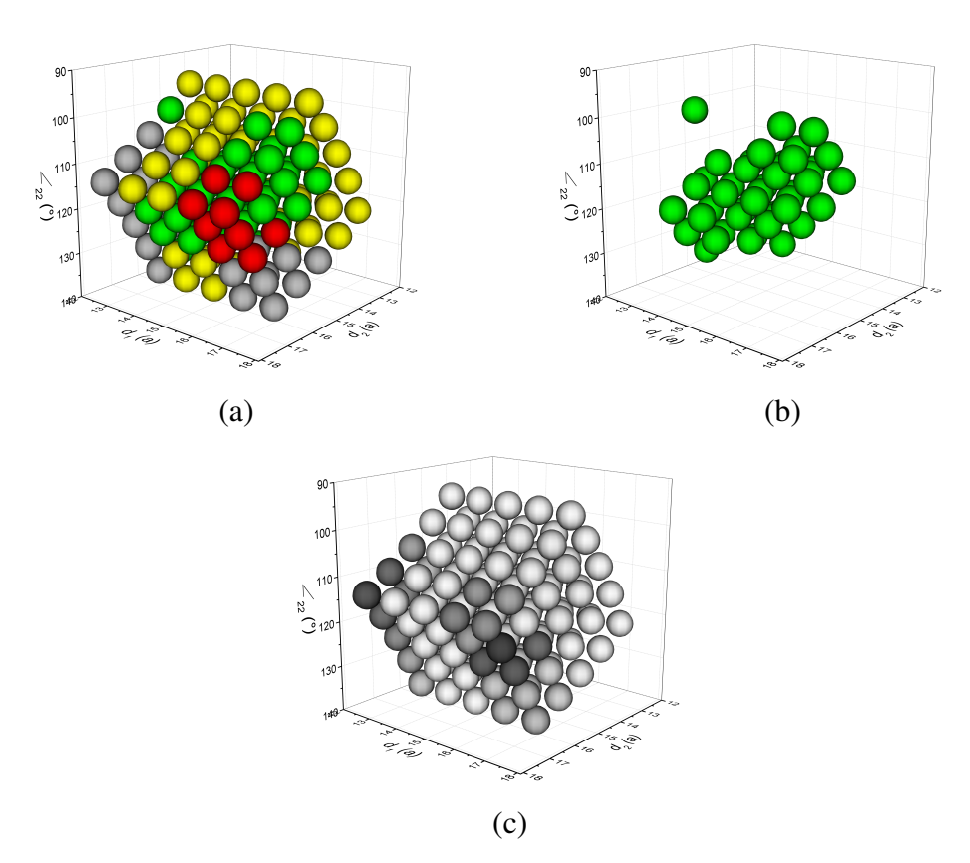


**Figure 5.21:** (a) The parity of the ground states, yellow balls are for metals, green balls are for topological insulators, red balls are for the insulators with broken symmetry (anti-ferromagnetic), gray balls are for trivial insulators. (b) The parity of the ground states for the topological insulators only (green balls in (a)). (c) The band gap between the lowest filled state and the highest empty state, the colour of the balls stands for the value of gap, white balls are for the metals (closed gap), and the darker colour stands for the larger gap.

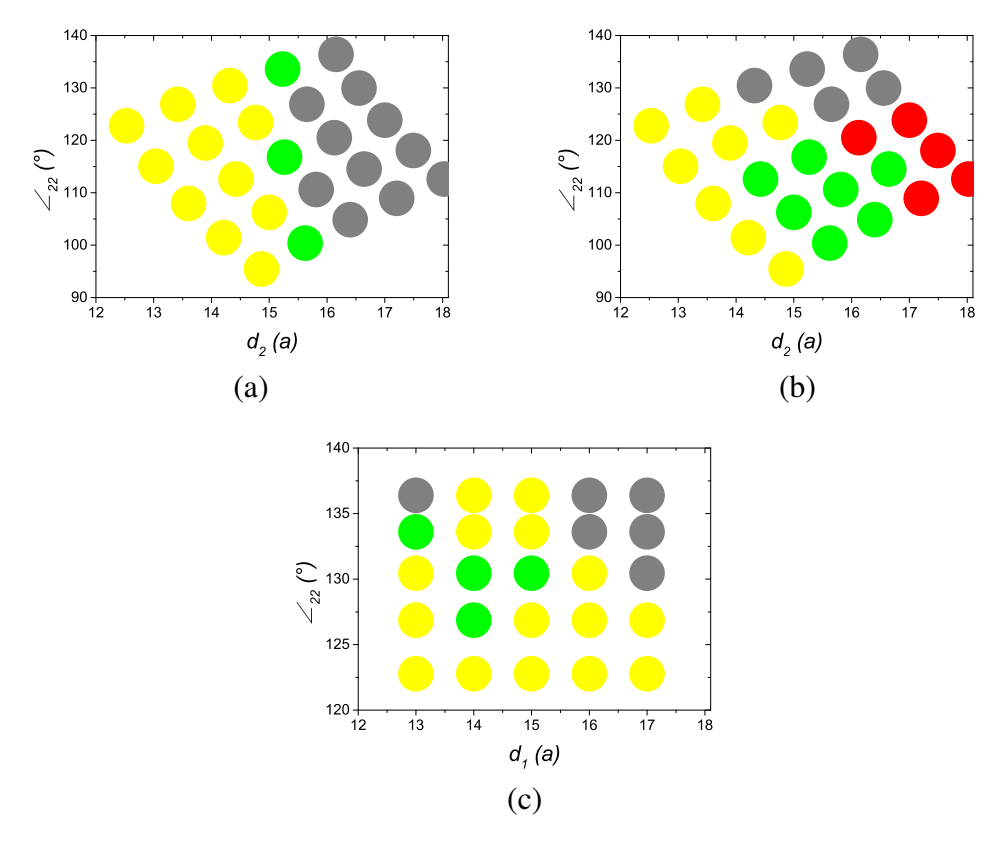


**Figure 5.22:** The parity of the ground states for different layers, yellow circles are for the metals, green circles are for the topological insulators, red circles are for the insulators with the broken symmetry (anti-ferromagnetic), gray circles are for the trivial insulators. (a)  $d_1 = s_1 = 13a$ , (b)  $d_1 = s_1 = 17a$ , (c)  $s_3 = 6a$ .

honeycomb lattice under the cubic multi-hole model (with the cubic symmetry term in Equation 2.1 and hole-hole interactions). For the multi-hole model, the UHF approximation is the easiest one to be done as we are only interested in the ground state. Here the most important next nearest transitions (all the hopping between the next nearest neighbours, and the direct hole-hole interactions between the next nearest neighbours) are included in the following calculations to achieve a better prediction for the distribution of holes (a better prediction for the symmetry as well) as the further calculations are based on the inversion symmetry as well as the time reversal symmetry. Firstly, we consider the case where the two acceptors in the cell in Figure 5.3 are set along the the z-axis. To investigate the topological property of the ground state, we need to calculate the parity of the filled states (highest 2 states as there are 2 acceptors/cell) and get the value of  $Z_2$  invariant v by following

Equation 1.7 in §1.5 which is based on the time-reversal symmetry. Since the insulating behavior is also required to form a topological insulator, an open gap without band overlapping between filled states and empty states is also required. The band structure of the highest 4 Fock matrix eigenvalues when  $d = 2.2a_0$  and  $d = 2.3a_0$  is shown in Figure 5.19. We find band overlapping between filled and empty states when  $d < 2.3a_0$ , so the system shows the metallic behavior for those separations and will become an insulator when  $d \ge 2.3a_0$ . Here we should point out that some states of level 3 and 4 around  $\Gamma$  point (the part of the dash line above the Fermi energy) in Figure 5.19 (a) have higher energies than part of bands 1 and 2, resulting in a metallic system. So we need to allow the holes to fill those states so that the right band structures can be achieved, which leads to the partial-filled UHF model used here. It is worth pointing out that this is the first example studied in this thesis that is predicted to be metallic within the UHF model.

By calculating the magnetic angular momentum along the z-axis (which is the only non-zero component and shown in Figure 5.20), it is found that the broken symmetry shows up when  $d = 2.4a_0$  and the system will be anti-ferromagnetic when  $d > 2.4a_0$ . The symmetry breaking not only means the parity calculation cannot be done due to the loss of the inversion symmetry but also leads to the loss of the time reversal symmetry. So we cannot calculate the  $Z_2$  invariant v using Equation 1.7. Therefore, we only need to test the parity from  $d = 2.3a_0$  to  $d = 2.35a_0$ . The parity of 4 typical symmetry points and the relevant  $Z_2$  invariant  $\nu$  for different separation d are shown in Table 5.4. The odd parity can be achieved for all the separations in this range, so the honeycomb lattice contains non-trivial topological states from  $d = 2.3a_0$  to  $d = 2.35a_0$  when the two acceptors in the cell are set along the the z-axis. We should point out that although we find the topological insulator occurs here, it does not mean the topological insulator cannot be achieved outside this zone. As explained in §4.2.3, the symmetry breaking is a result of the UHF approximation, which makes the calculation of the  $Z_2$  invariant cannot be done. So it still possible to be topological when  $d \ge 2.4a_0$ . This requires further investigations under other improved methods. The multiconfiguration self consistent field theory

may be helpful [58]. There a linear combination of the broken symmetry states can be used as the approximation of the full CI ground state, which could still contain the symmetry required for the calculation of the  $Z_2$  invariant. Also, considering that the broken symmetry is introduced by the UHF method, the general slave-rotor method mentioned in Reference [66] also offers an option to solve the problem here as it may not lead to the broken symmetry.

In (010) plane for the real doped silicon, the silicon atoms will be organized in a square structure which is rotated from z-axis by 45° towards x-axis. To predict the behavior of the honeycomb structure in the the real doped silicon with a cubic unit cell, a better choice is to set the cell in Figure 5.3 along [101] direction in the x-z plane according to the structure of the silicon lattice. It means the lattice will be rotated by 45° towards x-axis while the basic structure remains the same. So it is not surprising to see that it shows similar behavior that we have shown above. By doing the calculations for this rotated system, it can be found that we will have a topological insulator from  $d = 2.2a_0$  to  $d = 2.3a_0$ . It is not surprising to see the range for the topological insulator changes as we have seen many small differences in the energy behaviors between the [001] direction and the [110] direction under both the one hole model in Chapter 3 and the multi-hole model in Chapter 4.

Now we can try to achieve a topological insulator in the real doped silicon by locating all the acceptors on silicon lattice sites and choosing a proper separation according to our calculations above. Since electrically active acceptors are substitutional impurities at a silicon site,  $d_1$  and  $d_2$  will be different in this case. The system is not a perfect honeycomb lattice as calculated above, instead it is an almost-perfect honeycomb lattice with a slight distortion in the angles and a small difference between  $d_1$  and  $d_2$ . As we know the topological edge states are maintained when the angles are changed slightly under the spherical one-hole model [65], it is reasonable to believe that this almost-perfect honeycomb lattice could also show topological properties. We chose  $s_1 = d_1 = 15a$ ,  $s_2 = 13a$ ,  $s_3 = 8a$  (see Figure 5.3) as our target arrangement, where  $a = \frac{\sqrt{2}}{2}a_s$  is the nearest-neighbour spacing along [101] and  $a_s = 5.43 \text{Å}$  is the silicon lattice constant. This is the arrangement that most

closely approaches the perfect honeycomb lattice and also falls in the region of the stable topological insulator achieved above (from  $d = 2.2a_0$  to  $d = 2.3a_0$ ). As the distorted honeycomb lattice still has inversion symmetry, the previous test can still be applied. It is proved to contain the topological edge state under this arrangement by following the same steps in the earlier test.

Considering the precision of doping attainable in the real experiment described in §1.4, we also test misplaced arrangements close to the target one, giving 124 other possible arrangements which are achieved by adding either 1a or 2a to or taking either 1a or 2a from  $s_1$ ,  $s_2$  or  $s_3$  and any possible combinations of them. The parity of the resulting ground states and the band gap between the lowest filled state and the highest empty state are shown in Figure 5.21. For the convenience of following discussions, pictures are shown in the coordinate system labeled by  $d_1$ ,  $d_2$  and the angle between the two nearest-neighbour bonds with separation  $d_2$  ( $\angle_{22}$ ). In Figure 5.21 (a), yellow balls are for metals, green balls are for topological insulators, red balls are for the insulators with broken symmetry (anti-ferromagnetic), gray balls are for trivial insulators. In Figure 5.21 (b), only the green balls (topological insulators) are shown for the convenience to see the inner part. In Figure 5.21 (c), the colour of the balls stands for the value of gap, white balls are for the metals (closed gap), and the darker colour stands for the larger gap. It is found that the system is predicted to be a topological insulator in 44 cases among 125 in total, including 23 cases among 27 most likely misplaced arrangements (achieved by adding 1a to or taking 1a from  $s_1$ ,  $s_2$  or  $s_3$  and any possible combinations of them). We should also point out that the systems where we add 1a to or taking 1a from one of  $s_1$ ,  $s_2$  or  $s_3$  are all topological insulators. Considering there will only be a limited number of acceptors move away from the target arrangement in the experiment and those system with broken symmetry could still contain topological state, the topological property should be achieved in the real doped silicon under this target arrangement.

In Figure 5.21 (a), some systems have regions of trivial states (gray balls) which do not appear in the previous perfect honeycomb lattice. This is due to distortions in the honeycomb structure (large changes in the angles and the large

difference between  $d_1$  and  $d_2$ ). The parities of the ground states for different layers (two with constant  $d_1$ , one with constant  $s_3$ ) are shown in Figure 5.22. It can be seen that the trivial states appear when  $d_2$  is large in the  $d_1 = s_1 = 13a$  layer, while they appear when both  $d_2$  and  $\angle_{22}$  are large in the  $d_1 = s_1 = 17a$  layer. For the small  $d_1$ case (when  $d_1 = s_1 = 13a$ ), the intracell interactions are strong. When  $d_2$  is so large that the intercell interactions are too small to influence the transition of holes, the system will break up into many acceptor-pairs and there will be trivial states. For the large  $d_1$  case (when  $d_1 = s_1 = 17a$ ), the system is sensitive towards the changing in the angles. According to Figure 5.22 (c), the systems will transfer from metals to topological insulators when the angles are not far away from the equivalent case (120°), while they will transfer from metals to trivial insulators when the angles are large enough. The similar behavior is found in the spherical model as mentioned at the beginning of this section [65]. It also can be found that in some places trivial insulators directly adjoin topological insulators. This is because the separations used in those calculations are not continuous, with the finite step length being the nearest-neighbour spacing along [101] ( $a = 0.15a_0 = 3.84\text{Å}$ ). Considering the gaps between the lowest filled state and the highest empty state shown in Figure 5.21 (c) are very small for the topological insulators (green balls), the system could pass through a metallic region between the green ball and the gray ball even though they are next to each other. Fortunately, there is a good example when  $s_2 = 13a$  and  $s_3 = 6a \; (\angle_{22} = 130.45^{\circ} \text{ in Figure 5.22 (c)}).$  The system shows metallic behaviours (yellow circle) when  $d_1 = 13a$  and becomes a topological insulator (green circle) when  $d_1 = 14a$ . After that, before reaching the trivial zone (gray circle) at  $d_1 = 17a$ , the system shows metallic behaviours (yellow circle) again when  $d_1 = 16a$ . It suggests that trivial insulators indeed do not directly adjoin topological insulators. The system will be metallic between them, which is not shown due to the discrete separations used here.

#### 5.4 Summary

In this chapter, we showed the energy states for the finite rectangle arrangements as well as the band structures for periodic boundary condition cases under both the one-hole model and the multi-hole model.

For the one hole model, we find the 2D systems will behave like the corresponding one dimensional systems. Compared with the one-dimensional finite chain in §3.2.2, there will be some states localized at particular acceptors due to the nonequivalent potential. And the non-trivial topological edge states found in the infinite ladders and zigzag structures agree with the results for the infinite chains in §3.2.3.

For the multi-hole model, we compared the full CI result with the UHF one, and found the nonequivalent distribution of holes in the cases only with the nearest transitions, which can be fixed by including next-nearest transitions. This nonequivalent distribution of holes is not going to happen in every calculation without next-nearest transitions. So for the arrangements without the nonequivalent distribution of holes, the calculation only with the nearest transitions can still provide an accurate prediction. According to our experience, the nonequivalent distribution of holes is more likely to happen in the system involving very small separations.

In the infinite chain case, we found anti-crossings between the filled states and empty states, which come from the crossings in the non-interacting case. There we find different choices of the unit cell could lead to different results as the symmetries are different. A large unit cell can achieve a more stable total energy state under the broken symmetry which cannot be realized by a small unit cell.

Then we demonstrated the existence of the topological edge states in the infinite honeycomb lattice by calculating the  $Z_2$  invariant. To predict the behavior in the real doped silicon lattice, we chose a proper separation according to both the silicon lattice structure and our previous calculations for the continuous case, and found that the system will be a topological insulator under that arrangement. Considering the precision of doping in the real experiment, we also test misplaced arrangements close to the target one (124 in all) to verify that the topological property is highly

likely to show up in a real experiment. We predicted that the system will be a topological insulator in 44 cases among 125 in total, including 23 cases among 27 most likely misplaced arrangements. We also pointed out that the systems where we add 1a to or taking 1a from one of  $s_1$ ,  $s_2$  or  $s_3$  are all topological insulators. Considering only a limited number of acceptors could move away from the target arrangement in the experiment and those system with broken symmetry could still contain topological state, the topological property should be achieved in the real doped silicon under this target arrangement. Then we investigated the origin of the trivial states under some arrangements, which is due to distortions in the honeycomb structure (large changes in the angles and the large difference between  $d_1$  and  $d_2$ ).

To detect the topological edge states in the experiment, spin-polarized photoemission and circular dichroism photoemission may be helpful [67, 68, 69]. As they can distinguish the states with different spins, the time reversal symmetry of the  $Z_2$ invariant can be tested.

Here we should point out that the topological state found here is different from the one predicted in the Graphene [70, 66]. Although the spin-orbit coupling was found in both systems, the physical origin of the term is very different. In 2005, C. Kane and E. Mele developed a model (KM model) to study the effects of spin orbit interactions on the low energy electronic structure of a single plane of graphene [70]. The spin-orbit term in the KM model in k-space can be written as

$$\hat{H}_{so}(\vec{k}) = 2\lambda \sum_{\sigma\sigma'} \sigma_{\sigma\sigma'}^{z} (\hat{a}_{\vec{k}\sigma}^{\dagger} \hat{a}_{\vec{k}\sigma'} - \hat{b}_{\vec{k}\sigma}^{\dagger} \hat{b}_{\vec{k}\sigma'}) \left[2\cos(\frac{3}{2}k_{z}a)\sin(\frac{\sqrt{3}}{2}k_{x}a) - \sin(\sqrt{3}k_{x}a)\right]$$

$$\equiv \hat{\psi}_{\vec{k}}^{\dagger} \gamma(\vec{k}) \sigma^{z} \tau^{z} \hat{\psi}_{\vec{k}}$$
(5.1)

where  $\hat{\psi}_{\vec{k}} = (\hat{a}_{\vec{k},\uparrow}, \hat{b}_{\vec{k},\downarrow}, \hat{b}_{\vec{k},\downarrow}, \hat{b}_{\vec{k},\downarrow})$ ,  $\hat{a}^{\dagger}, \hat{a}, \hat{b}^{\dagger}, \hat{b}$  are creation and annihilation operators for different acceptors in the cell,  $\gamma(\vec{k}) = 2\lambda \left[2\cos(\frac{3}{2}k_z a)\sin(\frac{\sqrt{3}}{2}k_x a) - \sin(\sqrt{3}k_x a)\right]$ , and  $\lambda$  is the spin-orbit coupling. It is odd under sublattice reversal, odd under spin reversal and odd under reversal of  $\vec{k}$  since  $\gamma(-\vec{k}) = -\gamma(\vec{k})$ . If we write down a tight-binding model to describe the hopping interactions between acceptors, it must include the difference between spin- $\pm \frac{1}{2}$  states and spin- $\pm \frac{3}{2}$  states. So we have the

 $\delta$ -dependent part of the interaction

$$\hat{H}_{\text{bond}ik} = \delta \sum_{m,m'} Q_{m,m'}^{\text{bond}} (\hat{a}_{i,m}^{\dagger} \hat{b}_{k,m'} + \hat{b}_{i,m}^{\dagger} \hat{a}_{k,m'})$$
 (5.2)

where  $Q^{\text{bond}} = (J^{\text{bond}})^2 - \frac{5}{4}$  is the quadrupole operator along the bond direction, and  $\delta$  is the hoping difference between spin- $\pm \frac{1}{2}$  states and spin- $\pm \frac{3}{2}$  states. So this is odd under sublattice reversal as above, but becomes even under spin reversal and even under reversal of  $\vec{k}$ . These are the opposite symmetries to the graphene case.

#### Chapter 6

#### **Conclusions**

We have developed an LCAO model to describe the properties of acceptor arrays in tetrahedrally bonded semiconductors by using the cubic model, within the independent-hole approximation. We have used it to predict the high-energy states of acceptor dimers (the states close to the ground state) and linear acceptor chains in silicon. In particular we have studied the highest few energy states in the finite chain, arising from linear combinations of the  $1\Gamma_8^+$  acceptor ground states. For the case of a single hole in the chain we find a complex interplay between the long-range Coulomb interaction and the topological properties of the chain; the electrostatic attraction between the hole and the acceptors in the interior of the chain 'splits off' a state localised on the end acceptor, and the transition between topological and non-topological states then takes place in the remainder of the chain. This has the consequence that a single hole has twofold-degenerate topological bound states derived from the highest energy band in the 'short-long' arrangement (where the chain ends in a short, rather than a long, bond) that merge into the bulk bands in the 'long-short' arrangement; these bound states are mainly localised on the *next-to*end acceptors, and their topological origin can be confirmed by computing the Zak phase in the corresponding infinite chain model.

In an array with many holes the long-range interactions are likely to be screened out by the motion of other holes. We approximate this effect by introducing a 'short-range model' in which phenomenological screening removes the effect of acceptors beyond the nearest neighbour of each pair. In this case the elec-

trostatic splitting off of the states localised on the end acceptors disappears, and the topological states of the highest band appear for the 'long-short' arrangement instead (where the chain ends in a long bond). The situation in the next-highest band is more complex and we trace this to a non-monotonic dependence of the effective hopping matrix element between these states on the acceptor spacing.

We note that even with the inclusion of screening, we would not expect our model to be accurate at large spacings (where the Coulomb interactions are expected to dominate over the inter-acceptor tunneling). For dimerised geometries we would expect the behavior to cross over from a band insulator (at small spacings) to an antiferromagnetic spin model (at large spacings); a similar transition is found in models of donor arrays [53]. The system would, however, remain insulating throughout. For the equally spaced case  $(d_1 = d_2)$  we would expect a true metal-insulator transition to occur in the real system which, being driven by interactions, is not captured in our independent-hole model. Experimental evidence from randomly doped p-type bulk Si (Si:B) suggests this occurs at densities around  $4.11 \times 10^{18} \, \text{cm}^{-3}$  as shown in the previous paper[16], corresponding to spacings around 6.24 nm  $\approx 2.45 a_0$ ; this is within the range of the typical separations (2 $a_0$ to  $5a_0$ ) considered in our calculations. Hence, even when we are working on the insulating side of the transition, our system is relatively close to the phase boundary and we might expect our results to remain qualitatively correct except when  $d_1=d_2$ (where we fail to predict the correct insulating behavior). The cases with  $d_1 \neq d_2$ , showing the topological behavior, should be qualitatively correct.

We also constructed multi-hole models for neutral, one-dimensional multi-acceptor chains based on three different methods: full configuration interaction, the Heitler-London approximation, and the unrestricted Hartree-Fock method. The HL approximation solves some of the problems with the CI method, but only the UHF method is able to cope with infinite chains under periodic boundary conditions.

From reference calculations on a pair of acceptors, we found that both the HL approach and the UHF method give good approximations to the ground state of the full CI calculation, with the HL approach offering a better result in the regimes

studied (which are on the insulating side of the Mott transition). The UHF method is less useful for the calculation of excited states, so we use the HL approximation to simplify the calculation of high-lying excitations when interactions are strong. The converged UHF state has a large gap between the filled and empty states, due to the self-consistent potential generated by the hole-hole interactions.

Comparing with the 3D measurements reported in Reference [13]  $(2.45a_0)$ , we find the Mott transition happens for smaller separations in some directions in 1D (between  $1a_0$  and  $1.5a_0$  for the [001] and [111] directions, between  $2a_0$  and  $3a_0$ for [110] the direction). In the 2D honeycomb lattice (discussed later), the Mott transition occurs at separations close to the experimental result of  $2.45a_0$  (between  $2.2a_0$  and  $2.3a_0$  when the cell is along the [001] direction, between  $2.35a_0$  and  $2.4a_0$  when the cell is along the [101] direction). The reason could be that the experimental result  $2.45a_0$  is based on random doping in a 3D system. So, this value is an average separation involving all directions which are not equivalent to each other due to the symmetry of the system  $(T_d)$ , and the average coordination number in the 3D experiments is also higher than the coordination number in the 1D and 2D systems. These mean that the predictions from our 1D and 2D calculations could differ from the experimental result. As the prediction depends on the directions involved in the calculations and the coordination number in 1D system is the lowest, it is reasonable that our predicted Mott transition in a 1D calculation happens far away from the experimental result in some directions.

For finite chains, the CI ground state is non-degenerate in the short-long arrangement in all directions, but joins three other states to form a 4-fold-degenerate manifold in the long-short arrangement, which is followed in energy by an 8-fold-degenerate state and another 4-fold-degenerate state. By checking the dominant components of these 16 states, we found that only the levels on the acceptors at the end of the chain change between different members of the manifold; the overall 16-fold degeneracy comes from the product of separate sets of 4 levels on each end acceptor. The topological nature of these edge states is confirmed by the presence of non-trivial phases in the classification of one-dimensional fermion edge states

by Turner et al. In the small-separation case where  $d_1+d_2=3a_0$ , an anti-crossing occurs between the ground state and the next excited states in the [001] direction, resulting in a switch from in unhybridized ground state dominated by  $m_F=\pm 3/2$  states to a hybridized state where  $m_F=\pm 1/2$  states are also present; this transition is related to the crossing between the filled UHF single-particle states. The UHF solution loses part of the symmetry of the underlying Hamiltonian; for particular arrangements, we found the further broken symmetries related to the crossing of Fock matrix eigenstates and changing of the degeneracy of the total energy states in full CI calculation in the [001] direction. The loss of symmetry corresponds to the emergence of static moments on each acceptor in the UHF approach.

We obtained the UHF band structures of the Fock matrix eigenvalues for infinite 1D systems. We found there is a large gap between the filled and empty states in a dimerised chain, which does not fully close in the uniform chain, showing the existence of a period-doubling perturbation. Since a gap is maintained throughout the transition from short-long to long-short arrangements, the Zak phase is constant (and equal to zero), despite the observation of non-trivial many-body edge states in the long-short case. Hence, this method does not capture the formation of edge states, while the previous method introduced by Turner et al can well characterise their topological properties. The nature of the bulk-edge correspondence in such interacting systems requires further investigation.

For 2D system, we showed the energy states for finite rectangular arrangements as well as the band structures for periodic boundary condition cases under both the one-hole model and the multi-hole model. For the one-hole model, we find the 2D systems will behave like the corresponding one-dimensional systems. Compared with the one-dimensional finite chain in §3.2.2, there will be some states localized at particular acceptors due to the nonequivalent electrostatic potential at different sites. Furthermore, the non-trivial topological edge states found for the infinite ladders and zigzag structures agree with the results for the infinite 1D chains in §3.2.3.

For the multi-hole model, we compared the full CI result with the UHF one,

and found an inequivalent distribution of holes (equivalent to the formation of a charge density wave) in some cases if we included only nearest-neighbour transitions; we showed this was an artefact which could be fixed by including next-nearest transitions. However, this inequivalent distribution of holes does not happen in all calculations without next-nearest transitions; we argued that, for the arrangements where the inequivalent distribution of holes does not occur, the calculation with nearest-neighbour transitions only can still provide accurate predictions. In our experience, the inequivalent distribution of holes is more likely to happen in systems with very small separations. In the infinite-chain case, we found anti-crossings between the filled states and empty states which derive from the crossings in the non-interacting case. We also find different choices of the unit cell can lead to different results as the allowed symmetries are different: a large unit cell can achieve a more stable state by exploiting broken symmetry which cannot be realized within a small unit cell.

Next, we demonstrated the existence of topological edge states in the infinite honeycomb lattice by calculating the  $Z_2$  invariant. To predict the behavior in the real doped silicon lattice, we chose a set of acceptor separations consistent with both the silicon lattice structure and our previous calculations for the continuous case; we found that the system will indeed behave as a topological insulator under that arrangement. Considering the precision of doping likely to be attainable in a real experiment, we also test misplaced arrangements close to the target one (124 in all) to verify that the topological property is highly likely to show up in a real experiment. We predicted that the system will be a topological insulator in 44 cases among 125 in total, including 23 cases among the 27 most likely misplaced arrangements. We also pointed out that the systems where we add 1a to or take 1a from any one of the three integers  $s_1$ ,  $s_2$  or  $s_3$  defining the structure are all topological insulators. Considering only a limited number of acceptors might be expected to move away from the target arrangement in the experiment, and also that even those systems where we find broken symmetries could still contain topological states, it seems promising that topological properties could be achieved in real doped silicon structures under this target arrangement. Finally, we investigated the origin of the trivial states under some arrangements, which arise due to distortions in the honeycomb structure (large changes in the angles and large differences between the nearest-neighbour bond lengths  $d_1$  and  $d_2$ ).

To detect the topological edge states in an experiment, spin-polarized photoemission and circular dichroism photoemission may be helpful [67, 68, 69]. As these experiments can distinguish electron states with different spins, the time reversal symmetry of the  $Z_2$  invariant could be explicitly tested. We also pointed out that the topological states found here are different from those predicted in graphene, as the spin-orbit coupling term has a different physical origin.

For further investigation, we have four suggestions based on our work in this thesis. First, as discussed in  $\S5.3.3$ , further investigations for the honeycomb lattice under improved methods are still important. The broken symmetry is introduced into the system by the UHF method, which means the  $Z_2$  invariant cannot be calculated under some arrangements. A method without symmetry breaking will solve this problem and could find a wider region of stability for the topological insulator. As suggested earlier, multiconfiguration self-consistent field theory may be helpful [58]. There a linear combination of the broken-symmetry states can be used as an approximation to the full CI ground state, which could still contain the symmetry required for the calculation of the  $Z_2$  invariant. Considering that the broken symmetry is introduced by the UHF method, the general slave-rotor method mentioned in Reference [66] also offers an option to solve the problem that may not lead to broken symmetry.

Second, we can apply the current one-hole model and multi-hole model to 3D systems. As the models developed in this thesis appeared to provide reliable results on both 1D and 2D systems, we could expect that they are also valid in three dimensional cases. Where the Mott transition happens in the 3D system should agree more closely with the experimental measurements (at separations  $2.45a_0$ ). Just as topological edge states were found in both 1D and 2D cases, they should also exist in the 3D system under some particular arrangements. Based on the experience

of previous investigations into Graphene [71, 72], double-layer system could be a starting point. Although double-layer deterministic doping is still a challenge in experiments, a theoretical treatment should be possible. Other interesting 3D arrangements in Reference [73] are also predicted to contain topological states which form not on the surfaces but along the edges; these arrangements are also trying out in acceptor systems.

Another suggestion is try to combine the acceptor system with donors to investigate the behavior of p–n junctions. As discussed in §1.4, some experiments have been done about on p–n junctions, and considering the reliable results achieved by the current models for the individual donor and acceptor systems [3, 4, 5, 6, 7, 8, 9, 10, 65, 74, 75], it is reasonable to expect a good description of p-n junctions where some interesting behavior could arise from the interactions between acceptors and donors.

Also, some corrections for the basic model could be interesting and worth including in further investigations. It is found that the symmetry of the acceptor system plays an important role in some materials such as GaAs [76], where the fact that the true symmetry of the acceptor site is lower that the symmetry of effective mass theory results in a substantial change to the charge distribution. As a result, a central-cell correction is required to reflect the possible effects of tetrahedral symmetry in the core of the acceptors, and applying such a central-cell correction to the current models could offer the opportunity to assess the importance of these effects and to achieve more reliable results.

Last but not least, the current models could be applied to other 2D acceptor systems. In this thesis, we only investigated a few two-dimensional systems. So we can continue to work on other arrangements of acceptors (for example, nanoribbons with armchair edges or zigzag edges [77, 78, 79]) to search for further interesting behaviors.

#### Appendix A

## Modeling details for single-acceptor calculation

The calculations for a single acceptor are done by coding in Mathematica. We start from a list of spherical states which will be included in the calculation (up to a maximum of L=3 and  $F=\frac{9}{2}$  in our case). Then we can code Equations 2.1 to 2.4 with the help of the appendix in Reference [6]. The 3-j symbol and the 6-j symbol can be realized by using 'ThreeJSymbol' and 'SixJSymbol' commands in Mathmatica, while the 9-j symbol can be written in terms of 6-j symbols as follows:

$$\begin{cases}
j_1 & j_2 & j_3 \\
j_4 & j_5 & j_6 \\
j_7 & j_8 & j_9
\end{cases} = \sum_{x} (-1)^{2x} (2x+1) \begin{cases}
j_1 & j_4 & j_7 \\
j_8 & j_9 & x
\end{cases} \begin{cases}
j_2 & j_5 & j_8 \\
j_4 & x & j_6
\end{cases} \begin{cases}
j_3 & j_6 & j_9 \\
x & j_1 & j_2
\end{cases},$$
(A.1)

where x takes values from  $\max\{|j_1-j_9|, |j_4-j_8|, |j_2-j_6|\}$  to  $\min\{|j_1+j_9|, |j_4+j_8|, |j_2+j_6|\}$ .

We then calculate the matrix elements in the basis of these functions; next, we will transform these matrix elements into a set of basis functions belonging to the irreducible representations of the cubic double group, by using projectors connecting the  $|L,J,F,m_F\rangle$  basis to the cubic symmetry basis. According to the formulae given in Reference [48], the projection operator onto states of irreducible

representation  $\alpha$  can be written as

$$P^{(\alpha)} = \frac{s_{\alpha}}{g} \sum_{a} \chi^{\alpha*}(G_a) T(G_a), \tag{A.2}$$

where  $T(G_a)$  are the transformations induced by the elements  $G_a$  of a group G,  $\chi^{\alpha}(G_a)$  are the corresponding characters of representation  $\alpha$ , g is the order of the group G,  $s_{\alpha}$  is the dimensionality of the irreducible representation  $\alpha$  (the size of the basis for corresponding symmetry  $\alpha$ ). In our case, the group G is the cubic group  $O_h$ , so g=48,  $T(G_a)$  are rotation matrices and inversion transformations, and  $\alpha$  runs over  $\Gamma_6^{\pm}$ ,  $\Gamma_7^{\pm}$ ,  $\Gamma_8^{\pm}$ . As shown in Reference [48], rotation matrices are given in a basis of states of total angular momentum F by

$$D_{m'_{F}m_{F}}^{(F)}(\alpha,\beta,\gamma) = e^{-i(\alpha m'_{F} + \gamma m_{F})} \begin{pmatrix} 2F \\ F - m'_{F} \end{pmatrix}^{-\frac{1}{2}} \begin{pmatrix} 2F \\ F - m_{F} \end{pmatrix}^{\frac{1}{2}} \times \sum_{x} \begin{pmatrix} F + m_{F} \\ x \end{pmatrix} \begin{pmatrix} F - m_{F} \\ F + m'_{F} - x \end{pmatrix} \times (-1)^{F + m'_{F} - x} (\cos\frac{\beta}{2})^{2x - m_{F} - m'_{F}} (\sin\frac{\beta}{2})^{2F - 2x + m_{F} + m'_{F}}, \quad (A.3)$$

where  $\alpha, \beta, \gamma$  are Euler angles (whose definitions can be found in a figure on page 520 in Reference [48]), x takes values from Max $\{0, m_F + m_F'\}$  to Min $\{F + m_F, F + m_F'\}$ . The influence of the inversion operation can be included by multiplying the relevant rotation matrices by  $\pm 1$ , depending on the spatial parity: we take +1 for  $\{\Gamma_6^+, \Gamma_7^+, \Gamma_8^+\}$  and -1 for  $\{\Gamma_6^-, \Gamma_7^-, \Gamma_8^-\}$ . The characters  $\chi^{\alpha}(G_a)$  and the bases for different symmetries can be found in the table for  $O_h$  group in Reference [80]. The components of the cubic symmetry states can be decided by checking the relevant projectors which connect that cubic symmetry state with the spherical states in our list. If elements in a projector all equal to zero, it means there is no component of that spherical state in the given the cubic symmetry state. Diagonalizing the projectors and applying the eigenvectors corresponding to the non-zero eigenvalues to the  $|L,J,F,m_F\rangle$  basis, we will obtain the Hamiltonian function F(x) in the cubic

symmetry basis, where x is the radial parts of the states.

After obtaining the Hamiltonian function, we expand the basis in terms of Gaussian functions. The radial parts of the states (such as  $f_i(r)$  in Equation 2.5) are expanded by Equation 2.6, so the elements in each Hamiltonian matrix block can be written as

$$H_{ij} = \int_0^\infty r^{l'} e^{-\alpha_i r^2} F(r^l e^{-\alpha_j r^2}) dr, \qquad (A.4)$$

where l',  $\alpha_i$  and l,  $\alpha_j$  are the orbital angular momentum and Gaussian exponent for the initial state and finial state respectively. This integral can be analytically solved by the 'Integrate' command in Mathematica. We use 21 Gaussian functions, with exponents given by  $\alpha_i = \frac{5 \times 10^5}{2.42632^{i-1}}$ , so each Hamiltonian matrix block is a  $21 \times 21$  matrix. Here we choose the ratio 2.42632 to make the exponents fall in the same range ( $\alpha_1 = 5 \times 10^5$ ,  $\alpha_{21} = 0.01$ ) as in the previous paper [6]. Then we gather the Hamiltonian matrix blocks in the Gaussian basis according to the components of the cubic symmetry states by Mathematica 'Join' command, and get the energies and eigenvectors by diagonalizing the Hamiltonian with the help of 'Eigensystem' command.

#### Appendix B

## Modeling details for the tight-binding model

This part of calculations is done by coding in FORTRAN. First, let us begin with a pair of acceptors.

We separate the Hamiltonian into two parts as shown in Equation 3.2 and 3.3. Using Equations 3.2 and 3.3, we can obtain the transition strength between any two single-acceptor states on any sites.

The single-hole energies can then be found by solving a generalised eigenvalue problem provided we can compute the overlap  $\langle \phi_A | \phi_B \rangle$  and the potential term  $\langle \phi_A | \frac{1}{r_i} | \phi_B \rangle$ . We follow the methods in the previous paper [47] to get the matrix elements between the Gaussian orbitals, then multiply by the relevant Gaussian coefficients of the single-acceptor states and sum them according to Equation 2.6 to get the matrix elements in the Cartesian basis. Reference [47] gives the result for states up to P orbitals, while the results for higher angular momenta can be obtained by taking further derivatives along the different axis. In FORTRAN, these further derivatives can be found by building a recursive function which is a pure programming problem that we will not discuss here.

Then, with the help of spherical harmonics, the Cartesian basis can be transformed to the  $|L,m_L,J,m_J\rangle$  basis, which can in turn be transformed to the  $|L,J,F,m_F\rangle$  basis by using relevant Clebsch-Gordan coefficients. The transform matrix for the first step can be found in most of textbooks about quantum mechan-

ics or Wikipedia online, while the Clebsch-Gordan coefficients can be obtained by using the 'ClebschGordan' command in Mathematica. The projectors connecting the  $|L,J,F,m_F\rangle$  basis and the cubic symmetry basis can be obtained from the formula given in the projection operator section in reference [48]. Diagonalizing the projectors and applying the eigenvectors corresponding to the non-zero eigenvalue to the  $|L,J,F,m_F\rangle$  basis, we will get the Hamiltonian matrix and overlap matrix under the cubic symmetry basis. The steps above can be written as

$$H_{|L,m_L,J,m_J\rangle} = U_{\text{spherical harmonics}}^{\dagger} H_{Cartesian} U_{\text{spherical harmonics}},$$
 (B.1)

$$H_{|L,J,F,m_F\rangle} = U_{\text{Clebsch-Gordan}}^{\dagger} H_{|L,m_L,J,m_J\rangle} U_{\text{Clebsch-Gordan}},$$
 (B.2)

$$H_{\text{cubic}} = U_{\text{cubic}}^{\dagger} H_{|L,J,F,m_F\rangle} U_{\text{cubic}},$$
 (B.3)

where  $U_i$  is the relevant transform matrix. Finally, the eigenvalues and corresponding eigenvectors can be achieved by performing a generalized diagonalization. In FORTRAN, this can be realized by using the 'hegvd' subroutine in the 'lapack95' package.

For a larger system with more than two acceptors, most of the steps are the same. The differences are only which hopping interactions will be allowed in the model and which potential terms will be considered. After deciding these questions, formulae like Equations 3.5 to 3.10 will be obtained and the further steps will be the same as indicated above.

For an infinite system, we need to transform the Hamiltonian matrix to the momentum basis with the help of Fourier transformation

$$H_k = \int_{\text{first BZ}} e^{ikx} H dx. \tag{B.4}$$

We take small discrete steps for momentum k in the calculation so that the integral in Equation B.4 becomes summations

$$H_k = \sum_{x} e^{ikx} H. \tag{B.5}$$

In our calculations, we take the value of the integrand at the left-hand side of each interval for the whole range, and include each interval in the summation only if its left-hand edge is in the first Brillouin zone.

#### Appendix C

# Modelling details for full configuration interaction calculation and Heitler-London approximation

This part of the calculations is done by coding in FORTRAN. First, we need a list for all possible configurations of the holes; the size of this list depends on the number of acceptors. After listing all possible configurations, we need to decide which configuration will be included in the calculation. For a full CI calculation, all configurations are required; for HL cases, those configurations where more than one hole is localized at any one acceptor will be removed.

Next, we calculate the hole-hole integrals. These integrals can be achieved by the same method mentioned in Appendix B as the relevant formulas are offered in the previous paper [47]. We only need to remember applying the transformation matrices in Equations B.1 to B.3 to the basis for both holes separately.

After removing the unwanted configurations to get the list of states considered in the calculation, the Hamiltonian and the corresponding overlap matrix are formed within this basis by using Equations 4.1 and 4.2. A simple example of how to obtain the Hamiltonian for a hydrogen molecule including all possible configurations has been given in Section 2.3.1 of Reference [58]. This is equivalent to a two-acceptor, two-hole system as similar formulae used there apply for holes as well as for electrons. The Hamiltonian for a system with more than two holes can be achieved by

following the same logic.

Now we have the Hamiltonian and the corresponding overlap matrix under the multi-hole basis. The eigenvalues and corresponding eigenvectors can be obtained by performing a generalized diagonalization. In FORTRAN, this can be realized by using 'hegvd' subroutine from the 'lapack95' package. The eigenvalues are then the total energies of each multi-hole state (including the ground state and excited states), and eigenvectors are many-hole states expressed in the chosen multi-hole basis.

#### Appendix D

### Modelling details for unrestricted Hartree-Fock method

This part of the calculations is done by coding in FORTRAN. First, let us consider the case of a finite system.

As discussed in §4.1.2, we need to make an initial guess for the arrangement of holes based on our experience and the one-hole model results. This will be a one-hole density matrix expressed in the one-hole basis. In our calculations, we take two kinds of initial guess: the zero guess and the anti-ferromagnetic guess. For the zero guess, all the elements in the density matrix equal to zero, so the  $\hat{G}$ -matrix representing the hole-hole interactions is also zero. This is equivalent to taking the result from the one-hole model as the initial guess, and it is used in most cases. The anti-ferromagnetic guess is a density matrix with an anti-ferromagnetic configuration; in our calculations, we form this anti-ferromagnetic configuration in the density matrix by placing holes in the  $m_F = \pm \frac{3}{2}$  states. For example, the anti-ferromagnetic guess for a two-acceptor cell in our honeycomb lattice calculations

is

(where the ordering of the states is  $m_F = \{+\frac{3}{2}, +\frac{1}{2}, -\frac{1}{2}, -\frac{3}{2}\}$  for each acceptor). This guess is introduced in cases with large inter-acceptor separations where we expect the symmetry will break in an anti-ferromagnetic way; it is used in those cases simply to ensure the initial state achieves the right symmetry.

Next, we calculate the hole-hole integrals. These integrals can be obtained by the same method mentioned in Appendix B as the relevant formulas are given in the previous paper [47]. We only need to remember applying the transform matrices in Equation B.1 to B.3 on the basis for both holes separately.

Then using Equation 4.4, one can achieve the interacting matrix  $\hat{G}$  which reflects the hole-hole interactions within the one hole basis. The derivation of Equation 4.4 can be found in Chapter 3 of Reference [58]. There the authors considered a two-spin system without spin-orbit coupling and achieved the following formula for each spin:

$$G_{\mu\nu}^{\alpha} = \sum_{\lambda\sigma}^{\text{acceptor}} \left( P_T^{\lambda\sigma} \left( \mu\nu \|\sigma\lambda \right) - P_{\alpha}^{\lambda\sigma} \left( \mu\lambda \|\sigma\nu \right) \right), \tag{D.2}$$

$$G_{\mu\nu}^{\beta} = \sum_{\lambda\sigma}^{\text{acceptor}} \left( P_T^{\lambda\sigma} \left( \mu\nu \|\sigma\lambda \right) - P_{\beta}^{\lambda\sigma} \left( \mu\lambda \|\sigma\nu \right) \right), \tag{D.3}$$

where  $\mu, \nu, \sigma, \lambda$  are labels running over all acceptors only,  $G^i_{\mu\nu}$  is the interacting matrix element for spin  $i, P^{\lambda\sigma}_i$  is the single-particle density matrix element for spin

i, and  $P_T^{\lambda\sigma}$  is the single-particle density matrix element for the sum of the different spins. In our case, there are four different spins and the spin-orbit coupling also needs to be considered. To achieve a general formula, we allow  $\mu, \nu, \sigma, \lambda$  to run over all basis functions on all acceptors, so

$$\sum_{\lambda\sigma} P_T^{\lambda\sigma} (\mu \nu \| \sigma \lambda) = \sum_{\lambda\sigma} P^{\lambda\sigma} (\mu \nu \| \sigma \lambda), \tag{D.4}$$

where  $P^{\lambda\sigma}$  is the density matrix defined in Equation 4.6. Considering the interactions between different spins,  $\sum_{\lambda\sigma}^{\text{acceptor}} P_i^{\lambda\sigma}(\mu\lambda\|\sigma\nu)$  in Equation D.2 and D.3 will be replaced by  $\sum_{\lambda\sigma} P^{\lambda\sigma}(\mu\lambda\|\sigma\nu)$ . Then the general form for the interaction matrix  $\hat{G}$  becomes Equation 4.4.

After obtaining the matrix  $\hat{G}$ , one can easily get the Fock matrix  $\hat{F}$  by using Equation 4.3. The Fock matrix  $\hat{F}$  is still expressed in the non-orthogonal one-hole basis, so the corresponding overlap matrix is the same one used in the one-hole model. The eigenvalues and corresponding eigenvectors can be achieved by performing a generalized diagonalization. In FORTRAN, this can be realized by using 'hegvd' subroutine in the 'lapack95' package. The eigenvalues and eigenvectors then correspond to the single-hole states, so the total energy of the ground state can be obtained by using Equation 4.8 and the total density matrix is the sum of density matrices for each filled single-hole state.

According to self-consistent-field theory, the output total one-hole density matrix and the input guess should be equivalent if the input guess correctly reflects the configuration of the ground state. Hence, we need to set a threshold to check whether this is true or not. If the difference between the input and output density matrices is larger than the threshold, the output density matrix will be used as a new input guess for the next loop; if the difference is smaller than the threshold, we say the system has converged and the relevant generalized eigenvalues and eigenvectors of the Fock matrix will truly reflect the properties of the system which we are calculating. In our calculations, we set a threshold for the average difference of each element in the total density matrix so that the difference will not be influenced by

the size of the matrix. The value for the threshold is  $1 \times 10^{-6}$  for most cases; however, for some arrangements, the convergence is extremely slow as the initial guess is far away from the real distribution of holes. In these cases we take a larger value for the threshold (up to  $5 \times 10^{-5}$ ) after confirming the total density matrix will not be dramatically changed in those cases.

For an infinite system, we can combine the steps mentioned above with Fourier transformation according to Reference [59]. We take small discrete steps for momentum k in the calculation so that the integrals in Fourier transformation become summations. In our calculations, we take the value of the integrand at the left-hand side of each interval for the whole range, and include each interval in the summation only if its left-hand edge is in the first Brillouin zone. First, we make an initial guess for the density matrix in momentum space. Then it is transformed into the real space by

$$P = \sum_{k} e^{-ikx} P_k. \tag{D.5}$$

to calculate the  $\hat{G}$  matrix, after applying a truncation to the Coulomb interactions as described in §4.1.5. Later, we take a part of the  $\hat{G}$  matrix which shares the same surroundings as the unit cell in the infinite system and transform that part back to momentum space by

$$G_k = \sum_{x} e^{ikx} G. \tag{D.6}$$

to get  $\hat{G}_k$ . The Fock matrix in momentum space then can be obtained by using Equation 4.9. The eigenvalues and corresponding eigenvectors can be achieved by performing a generalized diagonalization, as before. The total density matrix is the sum of density matrices for each filled single hole state in momentum space, and the check for the convergence is also done in momentum space. For a 2D system, we need to take two components of the momentum vector along different directions, so  $\pm ikx$  in Equation D.5 and D.6 becomes  $\pm (ik_1x_1 + ik_2x_2)$ .

#### Appendix E

## Modelling details for topological invariants

This part of calculations is done by coding in FORTRAN.

The calculation of the Zak phase is very simple. The integral in Equation 3.11 is discretized to become a summation, taking small steps in momentum k to move through the Brillouin zone. In our calculations, we take the value of the integrand at the left hand side of the interval, and include the interval in the summation only if the left-hand edge of it is within the first Brillouin zone. Then we can code the integrand according to Equation 3.11 or 4.11, using the eigenvectors obtained in the tight-binding calculations or UHF calculations to calculate the Zak phase; this is a pure programming problem which we will not discuss here.

For the computation of the  $Z_2$  invariant based on the time-reversal symmetry, we take the eigenvectors for the filled states achieved in UHF calculations at four distinct time-reversal-invariant points in the Brillouin zone  $(\{(0,0),(0,\pi),(\pi,0),(\pi,\pi)\})$  and check their parities separately. In our calculations, we check the parity by applying the inversion transformation on the eigenvectors. If the outcome equals to the input, the eigenvector has even parity  $(\delta=1)$ ; if the outcome equals to the input times -1, the eigenvector has odd parity  $(\delta=-1)$ . The filled states are pairwise degenerate states for a system with time reversal symmetry (by Kramers' theorem) so they share the same parity. We only consider one of them, as the parity of the time-reversed state pair is required in Equation 1.7.

Using Equation 1.7, the value of v can be obtained.

To obtain the classification of the multi-hole topological phases, we check the the degeneracy and symmetry of the ground states under different arrangements in the full CI calculations to decide whether they are topologically non-trivial or not. The degeneracy can be read directly from the energy eigenvalues. In our case, it is 1 in the short-long limit, and becomes 4 in the long-short limit. According to the table offered in Reference [46], a non-degenerate state can only have  $(\mu = 0, \phi = 0, \kappa =$ 0) and a 4-fold degenerate state can only have  $\mu = 0$ , so the further calculation is not necessary for the short-long limit and we know  $\mu = 0$  for the long-short limit. Then we check the symmetry of the system to decide the values of  $(\phi, \kappa)$ . As the eigenvectors in the full CI calculation are expressed in the multi-hole basis, we need to calculate the reduced (one-hole) density matrices which will represent the state in the one-hole basis. The relevant discussion is given in Section 4.4 of Reference [58] and we will not repeat it here. After obtaining the reduced density matrix, we can apply to it the transformation matrices corresponding to different symmetries to check the symmetry of the system. As shown in §4.2.3, the system contains full symmetries (including inversion symmetry and time-reversal symmetry) in the long-short limit. According to the definitions of the three parameters (Equation 1.8 to 1.10) in §1.5,  $\mu$  and  $\phi$  correspond to inversion symmetry and time-reversal symmetry separately. As the system respects both those symmetries, we only need to check the details of the original eigenvectors. As  $\phi = \pi$  only if time-reversal changes the parity of the fermion number at either end when  $\mu = 0$  and this is not true in our case, we deduce that  $\phi = 0$  for the long-short limit. Considering the ground state has 4-fold degeneracy, the system can therefore only have  $(\mu = 0, \phi =$  $0, \kappa = \pi$ ) according to the table offered in Reference [46].

#### **Bibliography**

- [1] Michael Nielsen and Isaac Chuang. *Quantum Computation and Quantum In- formation*, volume 70. UK: Cambridge University Press, 01 2004.
- [2] B. E. Kane. A silicon-based nuclear spin quantum computer. *Nature*, 393(6681):133–137, May 1998.
- [3] J. M. Luttinger. Quantum theory of cyclotron resonance in semiconductors: General theory. *Phys. Rev.*, 102:1030–1041, May 1956.
- [4] Sokrates T. Pantelides and C. T. Sah. Theory of localized states in semiconductors. i. new results using an old method. *Phys. Rev. B*, 10:621–637, Jul 1974.
- [5] Belita Koiller, Xuedong Hu, and Sankar Das Sarma. Exchange in silicon-based quantum computer architecture. *Physical review letters*, 88:027903, 02 2001.
- [6] A. Baldereschi and Nunzio O. Lipari. Spherical model of shallow acceptor states in semiconductors. *Phys. Rev. B*, 8:2697–2709, Sep 1973.
- [7] A. Baldereschi and Nunzio O. Lipari. Cubic contributions to the spherical model of shallow acceptor states. *Phys. Rev. B*, 9:1525–1539, Feb 1974.
- [8] Nunzio Lipari and A Baldereschi. Interpretation of acceptor spectra in semiconductors. *Solid State Communications*, 25:665–668, 03 1978.

- [9] Adam C. Durst, Kyle E. Castoria, and R N. Bhatt. Heitler-london model for acceptor-acceptor interactions in doped semiconductors. *Physical Review B*, 96:155208, 06 2017.
- [10] Adam C. Durst, Genesis Yang-Mejia, and R. N. Bhatt. Quadrupolar interactions between acceptor pairs in *p*-doped semiconductors. *Phys. Rev. B*, 101:035202, Jan 2020.
- [11] P Clauws, J Broeckx, E Rotsaert, and Joost Vennik. Oscillator strengths of shallow impurity spectra in germanium and silicon. *Physical review. B, Condensed matter*, 38:12377–12382, 01 1989.
- [12] Nguyen Vinh, Britta Redlich, AFG van der Meer, C Pidgeon, P T. Greenland, Stephen Lynch, G Aeppli, and Ben Murdin. Time-resolved dynamics of shallow acceptor transitions in silicon. *Physical Review X*, 3:011019, 03 2013.
- [13] Peihua Dai, Youzhu Zhang, and M P. Sarachik. Electrical conductivity of metallic si:b near the metal-insulator transition. *Physical review. B, Condensed matter*, 45:3984–3994, 03 1992.
- [14] N. F. Mott. The Basis of the Electron Theory of Metals, with Special Reference to the Transition Metals. *Proceedings of the Physical Society A*, 62(7):416–422, July 1949.
- [15] J. Hubbard. Electron correlations in narrow energy bands. iii. an improved solution. *Proceedings of The Royal Society A: Mathematical, Physical and Engineering Sciences*, 281:401–419, 09 1964.
- [16] M. Sarachik and P. Dai. Scaling of the conductivity of insulating si:b: A temperature-independent hopping prefactor. *EPL* (*Europhysics Letters*), 59:100, 01 2007.
- [17] Jarryd J. Pla, Kuan Y. Tan, Juan P. Dehollain, Wee H. Lim, John J. L. Morton, Floris A. Zwanenburg, David N. Jamieson, Andrew S. Dzurak, and Andrea

- Morello. High-fidelity readout and control of a nuclear spin qubit in silicon. *Nature*, 496(7445):334–338, April 2013.
- [18] Thomas Watson, Bent Weber, Jill Miwa, Suddhasatta Mahapatra, Roel Heijnen, and Michelle Simmons. Transport in asymmetrically coupled donor-based silicon triple quantum dots. *Nano letters*, 14, 03 2014.
- [19] Yu Wang, Chin-Yi Chen, Gerhard Klimeck, Michelle Simmons, and Rajib Rahman. All-electrical control of donor-bound electron spin qubits in silicon. 03 2017.
- [20] M. Broome, Samuel Gorman, Matthew House, Samuel Hile, Joris Keizer, Daniel Keith, C. Hill, Thomas Watson, William Baker, L. Hollenberg, and Michelle Simmons. Two-electron spin correlations in precision placed donors in silicon. *Nature Communications*, 9, 03 2018.
- [21] Lukas Fricke, Samuel Hile, Ludwik Kranz, Yousun Chung, Yu He, Prasanna Pakkiam, Matthew House, Joris Keizer, and Michelle Simmons. Coherent control of a donor-molecule electron spin qubit in silicon. *Nature Communications*, 12, 06 2021.
- [22] Y. He, S. K. Gorman, D. Keith, L. Kranz, J. G. Keizer, and M. Y. Simmons. A two-qubit gate between phosphorus donor electrons in silicon. *Nature*, 571(7765):371–375, July 2019.
- [23] Marcos Atala, Monika Aidelsburger, Julio Barreiro, Dmitry Abanin, Takuya Kitagawa, Eugene Demler, and Immanuel Bloch. Direct measurement of the zak phase in topological bloch bands. *Nature Physics*, 9, 11 2013.
- [24] Eric Meier, Fangzhao An, and Bryce Gadway. Observation of the topological soliton state in the su-schrieffer-heeger model. *Nature Communications*, 7, 07 2016.

- [25] P. St-Jean, V. Goblot, Elisabeth Galopin, Aristide Lemaître, T. Ozawa, Luc Legratiet, Isabelle Sagnes, J. Bloch, and A. Amo. Lasing in topological edge states of a one-dimensional lattice. *Nature Photonics*, 11, 10 2017.
- [26] Rajesh Chaunsali, Eunho Kim, Aman Thakkar, Panayotis Kevrekidis, and Jinkyu Yang. Demonstrating an in situ topological band transition in cylindrical granular chains. *Physical Review Letters*, 119, 02 2017.
- [27] Sylvain Léséleuc, Vincent Lienhard, Pascal Scholl, Daniel Barredo, Sebastian Weber, Nicolai Lang, Hans Büchler, Thierry Lahaye, and Antoine Browaeys. Observation of a symmetry-protected topological phase of interacting bosons with rydberg atoms. *Science*, 365:eaav9105, 08 2019.
- [28] W. Cai, J. Han, Feng Mei, Y. Xu, Ma Yuwei, X. Li, H. Wang, Y.P Song, Zheng-Yuan Xue, Zhang-qi Yin, Suotang Jia, and Luyan Sun. Observation of topological magnon insulator states in a superconducting circuit. *Physical Review Letters*, 123, 08 2019.
- [29] M. Kiczynski, S. K. Gorman, H. Geng, M. B. Donnelly, Y. Chung, Y. He, J. G. Keizer, and M. Y. Simmons. Engineering topological states in atom-based semiconductor quantum dots. *Nature*, 606(7915):694–699, June 2022.
- [30] Konstantin Litvinenko, Ellis Bowyer, P.T. Greenland, N Stavrias, Juerong Li, R Gwilliam, B.J. Villis, G Matmon, Matthew Pang, Britta Redlich, A.F.G. van der Meer, C Pidgeon, G Aeppli, and Ben Murdin. Coherent creation and destruction of orbital wavepackets in si:p with electrical and optical read-out. *Nature communications*, 6:6549, 03 2015.
- [31] Joost van der Heijden, Takashi Kobayashi, Matthew G. House, Joe Salfi, Sylvain Barraud, Romain Laviéville, Michelle Y. Simmons, and Sven Rogge. Readout and control of the spin-orbit states of two coupled acceptor atoms in a silicon transistor. *Science Advances*, 4(12):eaat9199, 2018.
- [32] Andrea Corna, Léo Bourdet, Romain Maurand, Alessandro Crippa, Dharmraj Kotekar-Patil, Heorhii Bohuslavskyi, Romain Lavieville, Louis Hutin, Sylvain

- Barraud, X. Jehl, Maud Vinet, Silvano Franceschi, Yann-Michel Niquet, and Marc Sanquer. Electrically driven electron spin resonance mediated by spin-valley-orbit coupling in a silicon quantum dot. *npj quantum information*, 4:6, 02 2018.
- [33] Alessandro Crippa, Romain Maurand, Léo Bourdet, Dharmraj Kotekar-Patil, Anthony Amisse, Xavier Jehl, Marc Sanquer, Romain Laviéville, Heorhii Bohuslavskyi, Louis Hutin, Sylvain Barraud, Maud Vinet, Yann-Michel Niquet, and Silvano De Franceschi. Electrical spin driving by *g*-matrix modulation in spin-orbit qubits. *Phys. Rev. Lett.*, 120:137702, Mar 2018.
- [34] A. Crippa, R. Ezzouch, A. Aprá, A. Amisse, Romain Lavieville, L. Hutin, Benoit Bertrand, M. Vinet, Matias Urdampilleta, T. Meunier, Marc Sanquer, X. Jehl, Romain Maurand, and S. Franceschi. Gate-reflectometry dispersive readout and coherent control of a spin qubit in silicon. *Nature Communica*tions, 10:2776, 07 2019.
- [35] Joe Salfi, J Mol, Rajib Rahman, Gerhard Klimeck, Michelle Simmons, L C. L. Hollenberg, and Sven Rogge. Quantum simulation of the hubbard model with dopant atoms in silicon. *Nature Communications*, 7:11342, 04 2016.
- [36] Tomáš Škereň, Sigrun Köster, Bastien Douhard, Claudia Fleischmann, and Andreas Fuhrer. Bipolar device fabrication using a scanning tunnelling microscope. *Nature Electronics*, 3:1–7, 09 2020.
- [37] Georg Gramse, Alexander Kölker, Tomáš Škereň, Taylor Stock, Gabriel Aeppli, Ferry Kienberger, Andreas Fuhrer, and Neil Curson. Nanoscale imaging of mobile carriers and trapped charges in delta doped silicon p–n junctions. *Nature Electronics*, 3:1–8, 09 2020.
- [38] Matthew Radue, Sungha Baek, Azadeh Farzaneh, K. Dwyer, Quinn Campbell, Andrew Baczewski, Ezra Bussmann, George Wang, Yifei Mo, Shashank Misra, and R. Butera. Alcl 3 -dosed si(100)-2 × 1: Adsorbates, chlorinated

- al chains, and incorporated al. *The Journal of Physical Chemistry C*, 125, 05 2021.
- [39] Kevin Dwyer, Sungha Baek, Azadeh Farzaneh, Michael Dreyer, James Williams, and Robert Butera. B-doped -layers and nanowires from area-selective deposition of bcl 3 on si(100). *ACS Applied Materials & Interfaces*, 13, 08 2021.
- [40] Steven Schofield, Neil Curson, Michelle Simmons, F J Ruess, Toby Hallam, Lars Oberbeck, and Rebecca Clark. Atomically precise placement of single dopants in si. *Physical review letters*, 91:136104, 10 2003.
- [41] Taylor J. Z. Stock, Oliver Warschkow, Procopios C. Constantinou, Juerong Li, Sarah Fearn, Eleanor Crane, Emily V. S. Hofmann, Alexander Kölker, David R. McKenzie, Steven R. Schofield, and Neil J. Curson. Atomic-scale patterning of arsenic in silicon by scanning tunneling microscopy. ACS Nano, 14(3):3316–3327, March 2020.
- [42] Pierre Delplace, Denis Ullmo, and Gilles Montambaux. The zak phase and the existence of edge states in graphene. *Physical Review B*, 84:195452, 09 2011.
- [43] J. Zak. Berry's phase for energy bands in solids. *Phys. Rev. Lett.*, 62:2747–2750, Jun 1989.
- [44] Emilio Artacho and David D. O'Regan. Quantum mechanics in an evolving hilbert space. *Phys. Rev. B*, 95:115155, Mar 2017.
- [45] Liang Fu and C. L. Kane. Topological insulators with inversion symmetry. *Phys. Rev. B*, 76:045302, Jul 2007.
- [46] Ari M. Turner, Frank Pollmann, and Erez Berg. Topological phases of one-dimensional fermions: An entanglement point of view. *Phys. Rev. B*, 83:075102, Feb 2011.

- [47] E Clementi and D.R Davis. Electronic structure of large molecular systems. *Journal of Computational Physics*, 1:223–244, 11 1966.
- [48] J. P. Elliott and P. G. Dawber. *Symmetry in Physics*. London: Macmillan, January 1979.
- [49] Jianhua Zhu, Wei Wu, and Andrew J. Fisher. Msc project thesis. *unpublished*, 2018.
- [50] Nicola Marzari and David Vanderbilt. Maximally localized generalized wannier functions for composite energy bands. *Physical Review B*, 56:12847–12865, 07 1997.
- [51] Erik Nielsen and R. Bhatt. Nanoscale ferromagnetism in nonmagnetic doped semiconductors. *Phys. Rev. B*, 76, 05 2007.
- [52] Nguyen Le, Andrew Fisher, and Eran Ginossar. Extended hubbard model for mesoscopic transport in donor arrays in silicon. *Physical Review B*, 96, 07 2017.
- [53] Nguyen H. Le, Andrew J. Fisher, Neil J. Curson, and Eran Ginossar. Topological phases of a dimerized fermi-hubbard model for semiconductor nanolattices. *npj Quantum Information*, 6(1):24, February 2020.
- [54] Masatoshi Imada, A. Fujimori, and Yoshinori Tokura. Metal-insulator transition. *rmp*, 70:1039–, 10 1998.
- [55] Jorge Hirsch and S. Tang. Antiferromagnetism in the two-dimensional hubbard model. *Physical review letters*, 62:591–594, 02 1989.
- [56] Thomas Maier, M Jarrell, Th Pruschke, and J. Keller. d -wave superconductivity in the hubbard model. *Physical review letters*, 85:1524–7, 09 2000.
- [57] Daniel Arovas, Erez Berg, Steven Kivelson, and Srinivas Raghu. The hubbard model. *Annual Review of Condensed Matter Physics*, 13, 03 2022.

- [58] A. Szabó and N.S. Ostlund. *Modern Quantum Chemistry: Introduction to Advanced Electronic Structure Theory*. Macmillan, 1982.
- [59] Roberto Dovesi, R. Orlando, C. Roetti, C. Pisani, and V.R. Saunders. The periodic hartree-fock method and its implementation in the crystal code. *Physica Status Solidi B-basic Solid State Physics PHYS STATUS SOLIDI B-BASIC SO*, 217:63 88, 01 2000.
- [60] Lukasz Fidkowski and Alexei Kitaev. Effects of interactions on the topological classification of free fermion systems. *Phys. Rev. B*, 81:134509, Apr 2010.
- [61] Fabian Grusdt, Michael Höning, and Michael Fleischhauer. Topological edge states in the one-dimensional superlattice bose-hubbard model. *Phys. Rev. Lett.*, 110:260405, Jun 2013.
- [62] Andreas Rüegg, Jun Wen, and Gregory A. Fiete. Topological insulators on the decorated honeycomb lattice. *Phys. Rev. B*, 81:205115, May 2010.
- [63] Hai-Jun Zhang, Stanislav Chadov, Lukas Müchler, Binghai Yan, Xiao-Liang Qi, Jürgen Kübler, Shou-Cheng Zhang, and Claudia Felser. Topological insulators in ternary compounds with a honeycomb lattice. *Phys. Rev. Lett.*, 106:156402, Apr 2011.
- [64] Motohiko Ezawa. Monolayer topological insulators: Silicene, germanene, and stanene. *Journal of the Physical Society of Japan*, 84(12):121003, 2015.
- [65] Sankalan Bhattacharyya, Jianhua Zhu, and Andrew J. Fisher. Summer project report. *unpublished*, 2021.
- [66] Stephan Rachel and Karyn Le Hur. Topological insulators and mott physics from the hubbard interaction. *Phys. Rev. B*, 82:075106, Aug 2010.
- [67] C. Jozwiak, Y L. Chen, A V. Fedorov, J G. Analytis, C R. Rotundu, A K. Schmid, J D. Denlinger, Y.-D. Chuang, D.-H. Lee, I R. Fisher, R J. Birgeneau, Z.-X. Shen, Z. Hussain, and A. Lanzara. Widespread spin polarization effects

- in photoemission from topological insulators. *Phys. Rev. B*, 84:165113, Oct 2011.
- [68] M. Xia, J. Jiang, Z. R. Ye, Y. H. Wang, Y. Zhang, S. D. Chen, X. H. Niu, D. F. Xu, F. Chen, X. H. Chen, B. P. Xie, T. Zhang, and D. L. Feng. Angle-resolved photoemission spectroscopy study on the surface states of the correlated topological insulator ybb6. *Scientific Reports*, 4(1):5999, August 2014.
- [69] Baiqing Lv, Tian Qian, and Hong Ding. Angle-resolved photoemission spectroscopy and its application to topological materials. *Nature Reviews Physics*, 1(10):609–626, October 2019.
- [70] C Kane and E Mele. Quantum spin hall effect in graphene. *Physical review letters*, 95:226801, 12 2005.
- [71] Fariborz Parhizgar, Alireza Qaiumzadeh, and Reza Asgari. Quantum capacitance of double-layer graphene. *Physical review. B, Condensed matter*, 96:075447, 08 2017.
- [72] David Indolese, Paritosh Karnatak, Artem Kononov, Raphaëlle Delagrange, Roy Haller, Lujun Wang, Péter Makk, Kenji Watanabe, Takashi Taniguchi, and Christian Schoenenberger. Compact squid realized in a double-layer graphene heterostructure. *Nano Letters*, 20, 09 2020.
- [73] Frank Schindler, Ashley Cook, Maia Vergniory, Zhijun Wang, Stuart Parkin, B. Bernevig, and Titus Neupert. Higher-order topological insulators. *Science Advances*, 4, 08 2017.
- [74] Jianhua Zhu, Wei Wu, and Andrew J. Fisher. Linear combination of atomic orbitals model for deterministically placed acceptor arrays in silicon. *Phys. Rev. B*, 101:085303, Feb 2020.
- [75] Jianhua Zhu, Wei Wu, and Andrew Fisher. Multihole models for deterministically placed acceptor arrays in silicon. *Physical Review B*, 104, 09 2021.

- [76] A Yakunin, A Silov, P.M. Koenraad, J Wolter, W Roy, Jo De Boeck, Jian-Ming Tang, and Michael Flatté. Spatial structure of an individual mn acceptor in gaas. *Physical review letters*, 92:216806, 06 2004.
- [77] Ken-Ichiro Imura, Ai Yamakage, Shijun Mao, Akira Hotta, and Yoshio Kuramoto. Zigzag edge modes in a z 2 topological insulator: Reentrance and completely flat spectrum. *Physical Review B*, 82, 04 2010.
- [78] Feifei Xiang, Sven Maisel, Sumit Beniwal, Vladimir Akhmetov, Cordula Ruppenstein, Mirunalini Devarajulu, Andreas Dörr, Olena Papaianina, Andreas Görling, Amsharov Konstantin, and Sabine Maier. Planar -extended cycloparaphenylenes featuring an all-armchair edge topology. *Nature Chemistry*, pages 1–6, 06 2022.
- [79] Florentino López-Urías and Josue Ortiz-Medina. Unconventional metallicity in graphene nanoribbons with armchair edges. *Advanced Theory and Simulations*, 5:2100392, 01 2022.
- [80] George Koster. Properties of the thirty-two point groups. M.I.T. Press, 1963.